PERFORMANCE ASSESSMENT OF A TI6AL4V(ELI) LIGHT AIRCRAFT NOSE WHEEL FORK PRODUCED THROUGH LASER POWDER BED FUSION

HLAKAE PATRICK MIYA

Dissertation submitted in fulfilment of the requirements for the degree

MASTER OF ENGINEERING
in
MECHANICAL ENGINEERING

in the

Department of Mechanical and Mechatronics Engineering

Faculty of Engineering, Built Environment and Information Technology

at

Central University of Technology, Free State

Supervisor: Prof. W. B. du Preez, PhD, Pr Sci Nat

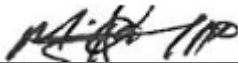Co-supervisor: L. F. Monaheng, M Eng (Mech)

BLOEMFONTEIN

April 2023

DECLARATION OF INDEPENDENT WORK

DECLARATION WITH REGARD TO

INDEPENDENT WORK

I, <u>Hlakae Patrick Miya</u>, identity number _____ and student number _____, hereby declare that this research project submitted to Central University of Technology, Free State, for the degree MASTER OF ENGINEERING in MECHANICAL ENGINEERING is my own original work, complies with the Code of Academic Integrity, other relevant policies, procedures, rules and regulations of Central University of Technology, Free State and has not been submitted before to any institution by myself of any other person in fulfilment (or partial fulfilment) of the requirements for the attainment of any qualification.

_____ _____14 April 2023_____

SIGNATURE OF STUDENT **DATE**

ACKNOWLEDGEMENTS

SUMMARY OF THE WORK

A scaled-down nose wheel fork for a light aircraft was redesigned by applying topology optimization for manufacturing in Ti6Al4V(ELI) through laser powder bed fusion (LPBF). This scaled-down nose wheel fork was built together with the test specimens for tensile and fatigue testing in this study.

The test specimens were quality checked, tested, and analyzed through standard procedures to obtain the porosity levels, tensile and fatigue properties, and fracture characteristics. The effect of the inherent surface roughness on the high-cycle fatigue properties of LPBF Ti6Al4V(ELI) test specimens was investigated. These test specimens were built to the standard geometry without subsequent machining in three orthogonal directions. They were tested under constant load in a tension–tension fatigue testing machine in accordance with the ASTM E 466 standard. The data was collected and complied with the ASTM F3001 – 14 standard for additive manufacturing (AM) Ti6Al4V(ELI) with laser powder bed fusion. The fatigue performance of the Ti6Al4V(ELI) specimens built to the standard geometry without subsequent machining was compared to that of machined test specimens. It was found that the inherent surface roughness of the specimens built to the standard geometry reduced their fatigue life by about half that of the machined specimens.

A customized jig was designed and manufactured to simulate the operational conditions applicable to the scaled-down nose wheel fork. This jig allowed three critical load cases to be tested. The experimental results of the fatigue test specimens and the performance testing of the scaled-down nose wheel fork under static loading were used to evaluate the feasibility of LPBF for production of structural aircraft components, particularly the nose wheel fork. Based on the outcome of the study, it was concluded that it would be justifiable to build a full-scale prototype of the nose wheel fork for testing under operational conditions.

Keywords: Scaled-down nose wheel fork, Laser Powder Bed Fusion, Ti6Al4V(ELI) tensile properties, High cycle fatigue, Surface roughness, Performance testing.

PUBLICATION RESULTING FROM THIS RESEARCH

Peer-Reviewed Journal Article

TABLE OF CONTENTS

ABBREVIATIONS

AHRLAC – Advanced High-performance Reconnaissance Light Aircraft

AM – Additive Manufacturing

BCC – Body-Centred Cubic Structure

BIS – Beam Interference Solidification

BPM – Ballistic Particle Manufacturing

CAD – Computer-Aided Design

CRPM – Centre for Rapid Prototyping and Manufacturing

CSIR – Council for Scientific and Industrial Research

CUT – Central University of Technology, Free State

DfAM – Design for Additive Manufacturing

DMD – Direct Metal Deposition

DMLS – Direct Metal Laser Sintering

EBM – Electron Beam Melting

ELI – Extra Low Interstitials

FEM – Finite Element Modelling

HCF – High Cycle Fatigue

HCP – Hexagonal Close Packed

HIP – Hot Isostatic Pressing

HIS – Holographic Interference Solidification

IJP – Inkjet Printing

LENS – Laser Engineered Net Shaping

LCF – Low Cycle Fatigue

LOM – Laminated Object Manufacturing

LPBF – Laser Powder Bed Fusion

MJM – Multi Jet Modelling

NASA – National Aeronautics and Space Administration

NECSA – The South African Nuclear Energy Corporation

PBF – Powder Bed Fusion

SEBM – Selective Electron Beam Melting

SLA – Stereolithography

SFP – Solid Foil Polymerization

SGC - Solid Ground Curing

SLC – Selective Laser Cladding

SLM – Selective Laser Melting

SLS – Selective Laser Sintering

UFS – University of the Free State

UP – University of Pretoria

VAR – Vacuum Arc Re-melting

3DP – Three-Dimensional Printing

LIST OF FIGURES

LIST OF TABLES

CHAPTER 1: INTRODUCTION

1.1 Background

An agreement was reached between ADC Aeroswift (Pty) Ltd and Central University of Technology, Free State, to redesign the Advanced High-performance Reconnaissance Light Aircraft (AHRLAC) nose wheel fork for manufacture through laser powder bed fusion (LPBF) in Ti6Al4V(ELI). To achieve this, it was necessary to design the component for production using LPBF and apply topology optimization to minimize its weight. Although the competence of the Centre for Rapid Prototyping and Manufacturing (CRPM) in LPBF of Ti6Al4V(ELI) to produce certified medical implants had been proven, the feasibility of producing structural aerospace components in this alloy had not been researched. Therefore, it was necessary to produce data that could contribute towards qualifying the LPBF production process and the component for this application.

AHRLAC is a two-person cockpit pusher propeller plane designed by the South African company Aerosud and manufactured in partnership between Aerosud and the Paramount Group [1]. The AHRLAC company considers AM a technology suitable for their manufacturing strategy because with the use of the high-speed LPBF machine, Aeroswift, it would be possible to build larger parts for this aircraft, thus opening new horizons for AM technology in the aerospace industry. The Aeroswift machine has a build volume of 2000 x 600 x 600 mm [2].

The landing gear nose wheel fork of the AHRLAC is manufactured through conventional machining processes from Aluminium 7050 Alloy [1]. Given the large build volume of the Aeroswift machine, it would be possible to manufacture the nose wheel fork of the AHRLAC in this machine from the Ti6Al4V(ELI) alloy with its excellent properties of high strength-to-weight ratio (specific strength), good fatigue life and corrosion resistance [3].

The current study on the performance assessment of the nose wheel fork produced through LPBF from the Ti6Al4V(ELI) alloy was aligned with the

doctoral project of Mr L. F. Monaheng. It had to contribute towards qualifying the redesigned nose wheel fork by generating mechanical test data necessary for the eventual qualification of LPBF to produce this mission-critical structural component of the aircraft. Full functional performance testing of the redesigned nose wheel fork under operating load conditions was needed before it could be installed on the aircraft.

The LPBF technology has various advantages over conventional manufacturing methods. These include reduction of production costs because tooling is not necessary for this technology, high design freedom of complex-shaped parts, which could include topology optimization, and rapid prototyping [2][3]. Although a complex-shaped structural component of an aircraft can be produced using LPBF with reduced raw material waste, strict standards in the aircraft industry limit the application of Ti6Al4V components produced using LPBF technology [1][4]. This implies that performance assessment data that meet the aerospace standards remain the key factor for the acceptance of LPBF as a manufacturing technology in the aviation industry. One of the major challenges of this technology is the reduced fatigue life caused by the as-built surface roughness inherent to the LPBF process [5].

An inherent characteristic of the LPBF process is high localized heating and subsequent rapid cooling [6]. This leads to thermal gradients during the building process, which consequently induces thermal residual stresses within the part [7]. These unwanted residual stresses affect the mechanical properties and cause premature part failure. For example, tensile residual stresses add to stresses resulting from external loads and may cause distortion, cracks, and premature component failure [8]. High-cycle fatigue performance is very sensitive to residual stress because it can cause crack initiation at lower-than-expected applied stresses and limit the fatigue life of a component [8]. To avoid the negative effects of residual stress, stress-relieving heat treatment is applied on an LPBF part after the built process while it is still attached to the build platform. Thereafter, the part is subjected to a high-temperature annealing heat treatment to alter the microstructure of the material, consequently producing the desired mechanical properties for high-cycle fatigue behaviour, as required for structural aircraft components like the landing gear fork [1][7].

The landing gear of an aircraft is a critical structural system since it ensures safe landing, taxiing, and take-off. Therefore, it must be designed to absorb the high kinetic energy of impact, thereby reducing the impact loads transmitted to the aircraft [9]. Extensive performance testing was required to qualify the landing gear nose wheel fork, which was redesigned and manufactured in such a way that the weight was minimized while the required performance could be retained.

The feasibility of manufacturing structural aircraft components through LPBF must be validated by determining manufacturing precision and testing mechanical properties. A successful outcome of this study could provide a basis for a more extensive application of LPBF technology for the production of structural aerospace components [8][10].

1.2   Problem statement

As mentioned in section 1.1, the commercial AHRLAC is fitted with a nose wheel fork machined from 7050 aluminium. Although the redesigned topologically optimized nose wheel fork had been reduced in weight by using less metal, it resulted in a complex-shaped structural part that could not be produced using conventional manufacturing technology. However, producing the component through the LPBF technology was quite feasible. Despite this, the nose wheel fork of a light aircraft produced through LPBF in Ti6Al4V(ELI) had not been qualified before. Authorities such as the European Aviation Safety Agency (EASA) and the Federal Aviation Administration (FAA) require the manufacturability, suitability, and durability of a material used in an aircraft to be determined based on experimental tests to internationally accepted standards. Performance testing of the current nose wheel fork under operational loading conditions had never been done. Therefore, detailed performance testing information of the redesigned and LPBF-produced Ti6Al4V(ELI) nose wheel fork was required to validate the compliance of the process and the alloy with the requirements of the aircraft industry.

1.3   Aim of study

The aim of this study was to generate experimental data on the operational performance of a light aircraft nose wheel landing gear fork which was produced through LPBF of Ti6Al4V(ELI) that would contribute to the validation of the design of this component.

1.4   Objectives

The objectives of the study were:

a) To manufacture a scaled-down prototype of the nose wheel fork, together with test specimens for chemical, physical and mechanical testing, by using the EOSINT M280 machine.

b) To perform tensile and fatigue tests using as-built, followed by heat treatment, mechanical test specimens in the as-built geometry.

c) To determine the chemical composition, density, and microstructure of the test specimens.

d) To perform fractographic analysis on the mechanically tested specimens.

e) To design the test procedure and manufacture a test jig for performance testing of the scaled-down Ti6Al4V(ELI) nose wheel fork produced through LPBF.

f) To determine the mechanical characteristics of the scaled-down nose wheel fork under experimental static load conditions.

1.5   Delimitations

This study did not cover the performance assessment of the full-scale nose wheel fork due to the following reasons:

• It was not feasible to manufacture the full-scale component due to the limited bed size of the DMLS EOSINT M280 machine compared to the large size of the full-scale component.

- This study contributed to the comprehensive doctoral study of Mr L. F. Monaheng. Therefore, only the static performance assessment of the scaled-down nose wheel fork was conducted in this study.

1.6   Scope of work

In this research, experimental data was collected for the tensile and fatigue properties of standard test specimens that were characterized before mechanical testing. The test specimens were built through direct metal laser sintering (DMLS) in Ti6Al4V(ELI) to the standard geometry without subsequent machining to test the effect of surface roughness on their fatigue properties. Tension-tension fatigue tests were done on the DMLS Ti6Al4V(ELI) test specimens up to 5 million cycles. The fatigue behaviour and fracture properties of the test specimens were analyzed. The collected data provided confidence in the integrity of the scaled-down AHRLAC nose wheel fork prototype built together with the test specimens. Consequently, performance testing of the scaled-down nose wheel fork could proceed. A customized test jig for testing the performance of the landing gear fork was designed and manufactured. The performance of the scaled-down nose wheel fork under experimental static load conditions was tested.

1.7   Dissertation layout

Chapter 1 of the dissertation comprises an introduction and the need for the study. In this chapter, the background, problem statement, research aim, objectives and scope of the study are discussed. In Chapter 2, the literature study that was conducted to review the existing extent of qualification of AM in the aerospace industry for structural components and the insight gained in the field are presented. Chapter 3 entails the research methodology applied to obtain the required data from the Ti6Al4V(ELI) standard test specimens and the scaled-down nose wheel fork. The results are presented and discussed in Chapter 4. In Chapter 5, conclusions are drawn from the results, and future work is recommended.

CHAPTER 2: LITERATURE REVIEW

2.1 Introduction

This chapter provides the understanding gained by the student into the existing knowledge in the field as context for the research conducted in this project. It provides findings from the research on the behaviour and operation of landing gear forks for light aircraft, as well as the history and background of titanium and its alloys. An introduction to AM with further discussion of DMLS is followed by a discussion of the characteristics of the DMLS Ti6Al4V(ELI) alloy and the resulting mechanical properties. A discussion on fatigue includes fatigue failure of as-built DMLS Ti6Al4V parts. The next section deals with residual stress and its generation during the DMLS process. Finally, design for additive manufacturing (DfAM), considering the part geometry and the surface roughness of DMLS parts, is discussed.

2.2 Aircraft landing gear

2.2.1 Structure and operation of landing gear

Safety is of paramount importance on aircraft. Therefore, landing gear structures must safely support the weight of an aircraft during take-off, landing, and taxing. They are designed to absorb the kinetic energy of the impact during the landing and take-off of an aircraft. Depending on the size of an aircraft, these loads can be very high, which determines the size, type of landing gear required for an aircraft and retractability to avoid the aerodynamic drag during flight [9][11]. This implies that the landing gear must meet the requirements for the safety of aircraft, such as good strength, stability, good control and damping, as well as stiffness. The design limits and requirements, such as low weight and cost, high performance, as well as optimized development time and life of the landing gear, remain a challenge in the aerospace industry [12].

AHRLAC is equipped with a tricycle type of landing gear structure. This structure has the main gear system attached to the rear of the fuselage and

below the wings of an aircraft, whereas the front wheel is located at the nose section of the fuselage. See Figure 2.1 for an illustration.

Figure 2.1: Tricycle type of landing gear **[12]**

This type of configuration puts the centre of gravity of an aircraft in the centre of the two landing gear structures, which allows the aircraft to have a more forceful application of brakes during landing without nosing into the ground. It also helps to prevent ground looping since the centre of gravity is forward of the main landing gear [13].

The landing gear comprises four parts: the axle, shock absorber, torque arm and fork. During landing on a tricycle type of landing gear, the main gear touches down on two points, and a few seconds later, the tyre of the nose wheel follows. The transmission of ground reaction loads acting on the nose wheel starts from the tyre to the axle. This impact force on the axle is transmitted to the fork through two components that compress and bend the fork [14]. Since the primary purpose of the landing gear is to absorb the impact energy of the aircraft when it lands and taxies, it is critical to ensure that all the components of the landing gear are fit for purpose.

2.2.2 Failure analysis of landing gear nose wheel forks

It is important that the landing gear systems are carefully studied for different types of failures, defects and problems occurring on them. This helps to avoid accidents caused due to the failure of the landing gear, which can lead to

human death in some cases [15]. The main failure of a landing gear structure is usually due to fatigue, which occurs when the material is dynamically stressed beyond its limit. Failure analysis of landing gear structures is usually done by visual inspections of the failed component, followed by in-depth techniques, such as fractography. This is done to understand the crack growth behaviour which could lead to a final failure [16].

Franco et al. [17] studied the fatigue fracture of a nose landing gear manufactured in microalloyed vanadium steel for the military transport aircraft, EMB 121 – Xingu, which collapsed during take-off. In their study, they discovered that the landing gear is usually subjected to severe environmental conditions, such as temperature, climate, and operational situations, including runway conditions. These conditions could lead to failure of the landing gear. Also, in this study, apart from fatigue being a primary cause of failure, corrosion pits were identified as the secondary cause of crack initiation, which led to failure. This implies that corrosion also needs to be considered in the failure of landing gear systems.

Infante et al. [18] did a study on the aluminum alloy (series 5000), landing gear fork of a light aircraft that failed during landing. The assessments were done to determine the possible causes of failure observed during service. In their study, visual analysis and optical microscopy with a low magnification of the fracture surface were performed to characterize the type of fracture and identify areas of interest using scanning electronic microscopy (SEM). Following the outcome of the fractography, they also performed finite element analysis (FEA) and numerical simulation of the landing gear component to determine the stresses the component was subjected to. This contributed to a deeper understanding of the cause of failure of the landing gear. In another study of an aircraft accident, the stress intensity factors for crack initiation on fork holes were calculated. This contributed to a better understanding of fatigue crack propagation behaviour using finite element modelling (FEM) [14].

2.3   Titanium

2.3.1 History and background

Titanium was first discovered in England in 1790 by Reverend William Gregor [19]. This element was found to be a unique metal in black magnetic sand with a chemical composition that corresponded with ilmenite ($FeTiO_3$). This discovery raised interest worldwide, and it was followed by Martin Heinrich Klaproth in Hungary, who identified from his investigations the dioxide of the same metal in rutile ore (impure TiO_2) [19].

Klaproth decided to call the element titanium, named after mythological gods, the Titans, who were believed to possess enormous power. Klaproth attempted to isolate this metal, but his attempts failed. In 1910, the American chemist Matthew Arnold Hunter succeeded in developing a process to extract titanium from the mineral, followed by William Justin Kroll, who produced a ductile titanium metal by reacting titanium tetrachloride with magnesium metal in a closed system with an inert gas (argon) atmosphere, to avoid the traces of oxygen or nitrogen found when the process was carried out in air [19] [20].

2.3.2 The Kroll process

Today the Kroll process is the most commonly employed smelting process of titanium [21]. It begins with the chlorination process, where chlorine gas is reacted with rutile within an atmosphere saturated with carbon. Equation 2.1 describes this process:

$$TiO_2 + 2C + 2Cl_2 \rightarrow TiCl_4 + 2CO \dots\dots\dots\dots\dots (2.1)$$

The titanium tetrachloride formed is then reduced with magnesium to produce a product known as titanium sponge, together with magnesium chloride as a by-product, as shown in equation 2.2.

$$TiCl_4 + 2Mg \rightarrow 2Ti + 2MgCl_2 \dots\dots\dots\dots\dots (2.2)$$

This by-product is taken through electrolysis of the molten salt to recover magnesium and chlorine separately to be used again in the Kroll process.

2.3.3 Atomic structure and crystal structure

Titanium is element 22 in the periodic table with the symbol Ti. It has a low density of 4.5 g/cm^3 and an atomic weight of 47.9. Titanium is corrosion resistant because it is a reactive metal which forms a natural oxide surface layer spontaneously whenever it is exposed to oxygen. This oxide layer is usually compact, adherent to the substrate and chemically stable in a variety of environments, thus resulting in the excellent corrosion resistance of titanium [22]. Titanium also has a good yield and tensile strength, which, combined with its low density, result in a high strength-to-weight ratio or specific strength [20].

Titanium has two types of crystal structure in its pure form, the alpha (*α*) and beta (*β*) phases. The *α* phase is a hexagonal close-packed (HCP) structure, and the *β* phase is a body-centred cubic (BCC) structure [22][23]. These crystal structures are shown in Figures 2.2 and 2.3.
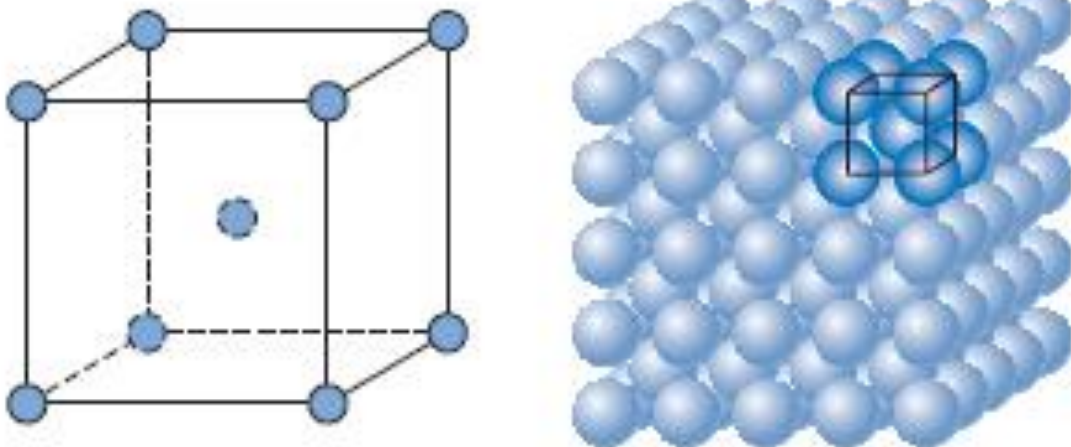
Figure 2.2: The body-centred cubic crystal structure. Left: a reduced-sphere unit cell, and right: an aggregate of many atoms [23]
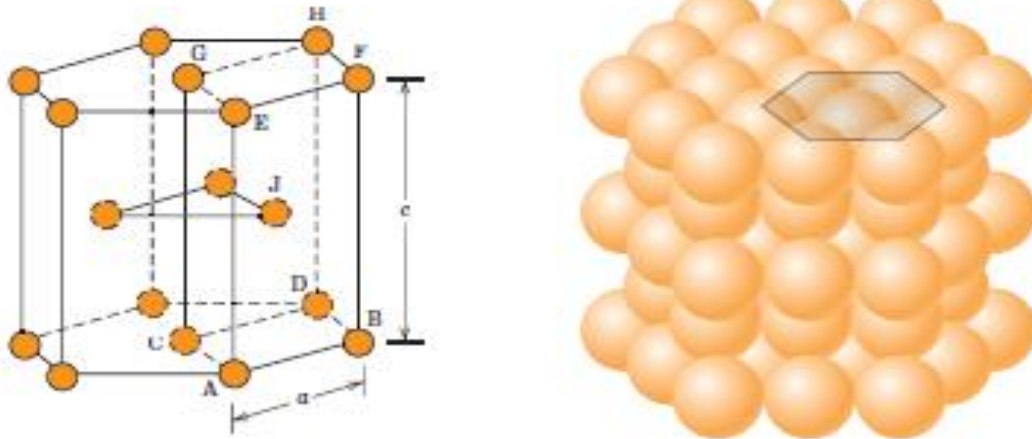
Figure 2.3: The hexagonal close-packed crystal structure, Left: a reduced-sphere unit cell, and right: an aggregate of many atoms [23]

The HCP structure in pure titanium develops at low temperatures, while the BCC crystal structure of titanium develops at higher temperatures when titanium transforms from the *α* to the *β* phase. The complete transformation from one crystal structure to the other is known as an allotropic transformation, and the transformation temperature is called the beta transus (*β* transus) temperature. The *β* transus temperature for pure titanium is 882 ± 2 °C. The *α* and *β* crystal structures are the most basic structures of titanium, and they form the basis of alloying titanium [24].

2.3.4 Titanium alloys

Titanium alloying elements are classified as neutral, *α*-stabilizers and *β*-stabilizers. These classifications are based on the influence that the elements have in stabilizing either the *α* phase or the *β* phase. The *α*-stabilizers raise the *β* transus temperature, while the *β*-stabilizers lower it [24]. In Table 2.1, the alpha and beta stabilizers are presented.

Table 2.1: Classification of selected alloying elements used in titanium alloys (After [24])

Alloy classification	α-stabilizers	β-stabilizers		Neutral
		β-eutectoid	β-isomorphous	
Substitutional	Al	Mo, V, Fe	Cr, Mn, Ni	Sn, Zr
Interstitial	O, N, C		H	

Titanium alloys are classified as follows:

- *α and near α* alloys - alloys with alloying elements that stabilize the *α*-phase.

- *β and near β* alloys – alloys with alloying elements that stabilize the *β*-phase

- *α+β* alloys – alloys with a mixture of elements that stabilize both the *α* and *β* phases.

In many alloys, the *β* phase is retained at room temperature, thus producing an alloy that contains both the *α* and *β* phases or even only the *β* phase [25]. The *α*-stabilizing elements extend the *α* phase field to a higher temperature, while the *β*-stabilizing elements shift the *β* phase field to a lower temperature. Figure 2.4 illustrates the effects of alloying with different elements on the phase equilibrium diagram of titanium.
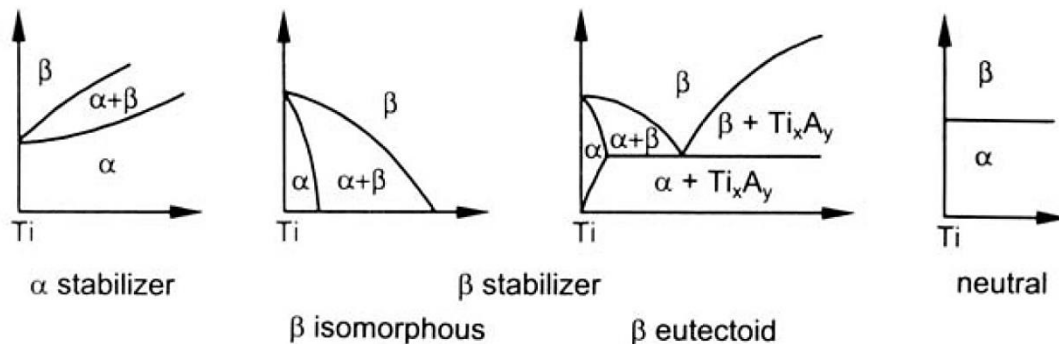
***Figure 2.4: Effect of alloying with different elements on the equilibrium phase diagram of titanium* [26]**

Apart from the abovementioned alloys, titanium alloys are furthermore subdivided into near *α* and near *β* alloys [23]. The three-dimensional phase diagram in Figure 2.5 illustrates the classification of the titanium-aluminium-vanadium alloys. If small percentages of *β*-stabilizing elements are added, they are referred to as near *α* alloys. The *α+β* alloys are the most widely used alloy group. If the proportion of *β*-stabilizing elements is further increased to a level where *β* no longer transforms to a martensite upon quenching, the alloys are

still in the two-phase field, and the class of metastable *β* alloys is reached [23]. Metastable *β* alloys form part of the four categories of *β* phase Ti alloys based on the approximation of *β* phase stability and molybdenum equivalency. Near *β* alloys are considered metastable *β* alloys because their composition places them near the *α+β* phase field and *β* phase field boundaries [27][28].
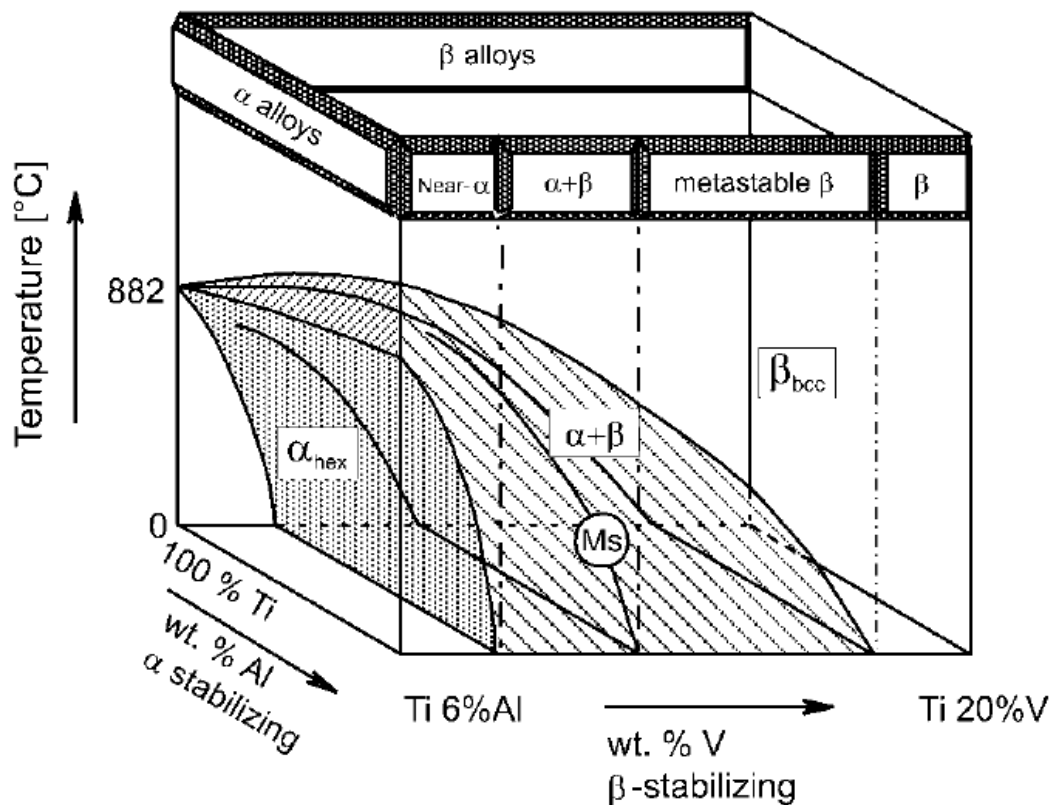
Figure 2.5: Three-dimensional phase diagram used to classify titanium alloys **[28]**

The content of *α* and *β* in an alloy after processing and heat treatment influences the microstructure, which in turn affects the mechanical properties of titanium alloys [29]. The *α* alloys have good weldability, satisfactory strength, creep resistance and high fracture toughness, which make them suitable for cryogenic applications. The *α+β* alloys, on the other hand, generally exhibit good manufacturability, increased ductility, and strength at high and moderately elevated temperatures. The 100% *β* alloys have good ductility, toughness, and excellent formability. Figure 2.6 summarizes the alloying effect for selected alloys according to their classifications.

α alloys	Unalloyed titanium Ti-5Al-2.5Sn	-Higher density -Increasing heat treatment response
Near-α	Ti-8Al-1Mo-1V Ti-6Al-2Sn-4Zr-2Mo	-Higher short time strength -Increasing strain rate sensitivity -Improved fabricability
α+β alloys	Ti-6Al-4V Ti-6Al-2Sn-6V	
Near-β	Ti-6Al-2Sn-4Zr-6Mo Ti-3Al-10V-2Fe	-Higher creep strength -Improved weldability
β alloys	Ti-13V-11Cr-3Al Ti-8Mo-8V-2Fe-3Al	

Figure 2.6: Summary of the alloying effect on the selected properties of the Ti alloys [25]

2.4 Additive manufacturing

According to the ASTM F2792 – 12a standard [30], AM is referred to as "a process of joining materials to make objects from 3D model data, usually layer upon layer, as opposed to subtractive manufacturing methodologies." The solid parts are directly fabricated from the computer-aided design (CAD) data. This offers design and manufacturing advantages, such as design freedom for complex geometries, short lead time due to no need for tooling and near-zero material wastage [4][31].
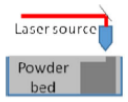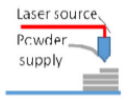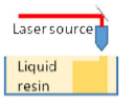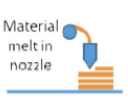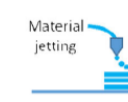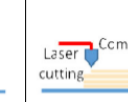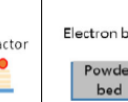
This technology is categorized based on its manufacturing processes. Over the past decades, different variations of AM technology have been developed. These include; Stereolithography (SLA), Holographic Interference Solidification (HIS), Selective Laser Sintering (SLS), and Selective Laser Melting (SLM) [31]. However, to simplify all these classification processes, ASTM F2792 was created as a guideline for classifying AM technologies. Below is the list of these categories according to the standard:

a) *Binder Jetting* – an additive manufacturing process in which a liquid bonding agent is selectively deposited to join powder materials.

b) *Directed Energy Deposition* – an additive manufacturing process in which focused thermal energy is used to fuse materials by melting as they are being deposited.

c) *Material Extrusion* – an additive manufacturing process in which material is selectively dispensed through a nozzle or orifice.

d) *Material Jetting* – an additive manufacturing process in which droplets of build material are selectively deposited.

e) *Powder Bed Fusion* – an additive manufacturing process in which thermal energy selectively fuses regions of a powder bed.

f) *Sheet Lamination* – an additive manufacturing process in which sheets of material are bonded to form an object.

g) *Vat Photopolymerization* – an additive manufacturing process in which liquid photopolymer in a vat is selectively cured by light-activated polymerization.

These listed processes are the only seven AM categories approved by ASTM International and ISO [30]. However, different companies have their own commercial AM brands and use their own terminology related to the seven categories. Table 2.2 illustrates how the commercial AM brands relate to the ASTM categories.

Table 2.2: Illustration of how AM processes are categorized by commercial brands [31]

Additive Manufacturing (AM) Processes						
Laser Based AM Processes			Extrusion Thermal	Material Jetting	Material Adhesion	Electron Beam
Laser Melting		*Laser Polymerization*				
SLS	DMD	SLA	FDM	3DP	LOM	EBM
SLM	LENS	SGC	Robocasting	IJP	SFP	
DMLS	SLC	LTP		MJM		
	LPD	BIS		BPM		
		HIS		Thermojet		

Bulk Material Type: Powder (green), Liquid (blue), Solid (red)

Referring to Table 2.2, it should be noted that processes such as Direct Metal Deposition (DMD) are classified according to the type of energy source and the form of material that they use. This shows that industry also develops its own

terminologies as technology improves. In Table 2.3, the classification of these commercial terminologies according to the seven classifications in the ASTM F2792 standard is presented.

Table 2.3: AM classifications of commercial brands from Table 2.2

Commercial brand name	Abbreviation	ASTM F2792 Classification
Selective Laser Sintering	SLS	Powder Bed Fusion
Selective Laser Melting	SLM	Powder Bed Fusion
Direct Metal Laser Sintering	DMLS	Powder Bed Fusion
Direct Metal Deposition	DMD	Directed Energy Deposition
Laser Engineered Net Shaping	LENS	Directed Energy Deposition
Selective Laser Cladding	SLC	Directed Energy Deposition
Laser Powder Deposition	LPD	Directed Energy Deposition
Stereolithography	SLA	Vat Photopolymerization
Solid Ground Curing	SGC	Vat Photopolymerization
Liquid Thermal Polymerization	LTP	Vat Photopolymerization
Beam Interference Solidification	BIS	Vat Photopolymerization
Holographic Interference Solidification	HIS	Vat Photopolymerization
Fused Deposition Melting	FDM	Material Extrusion
Three-Dimensional Printing	3DP	Material Jetting
Inkjet Printing	IJP	Material Jetting
MultiJet Modelling	MJM	Material Jetting
Ballistic Particle Manufacturing	BPM	Material Jetting
Laminated Object Manufacturing	LOM	Sheet Lamination
Solid Foil Polymerization	SFP	Sheet Lamination
Electron Beam Melting	EBM	Powder Bed Fusion

2.5 Direct metal laser sintering

Direct metal laser sintering (DMLS) is LPBF terminology used by the machine supplier EOS GmbH - Electro Optical Systems. This technology uses a laser to selectively fuse metal powder layer-by-layer to eventually build a three-dimensional (3D) part [32]. The process begins with CAD of the desired part to be manufactured, followed by the conversion of the CAD model into a programming file called a Stereolithography (STL) file. The STL file is read by the DMLS machine to manufacture a 3D part based on the design [30]. The DMLS process is illustrated in Figure 2.7.
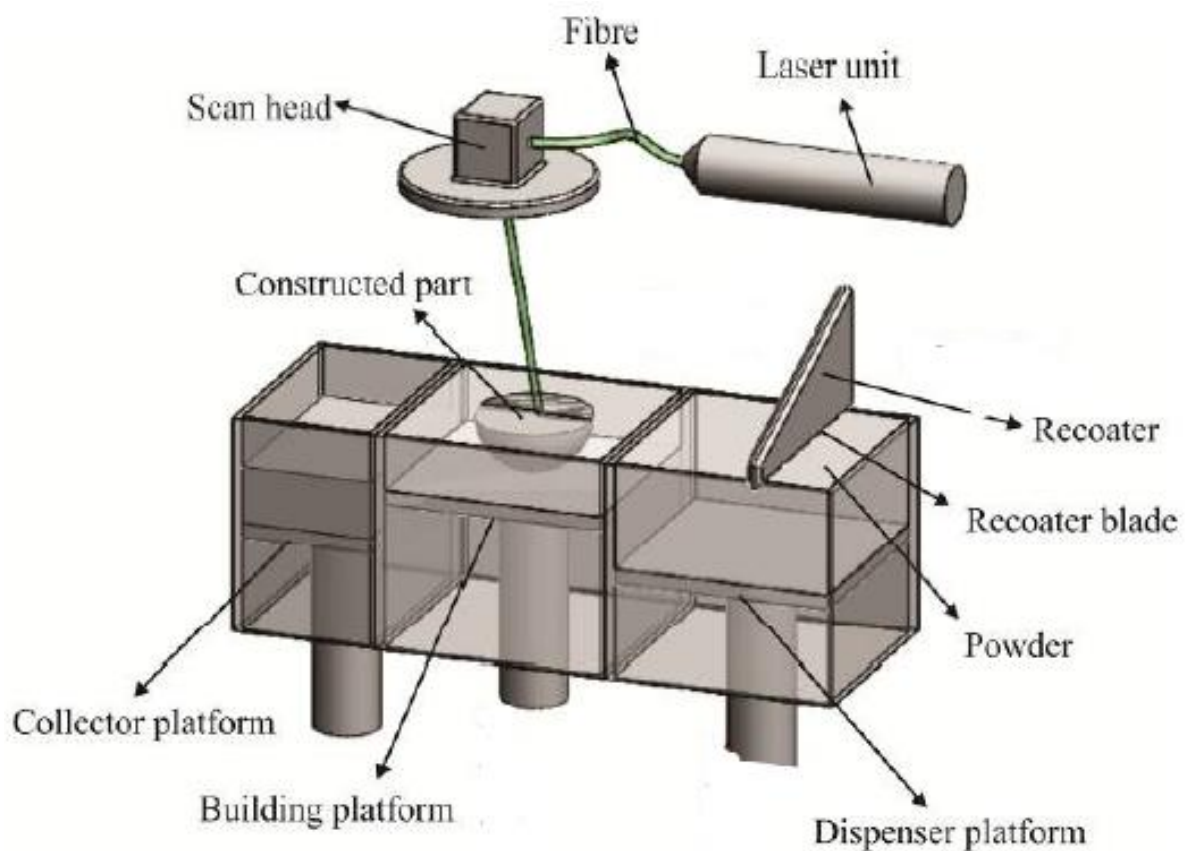
Figure 2.7: Schematic diagram of a DMLS system [33]

A thin layer of powder, typically 30 μm thick, is deposited onto the building platform by the recoater blade. To achieve this, the recoater blade moves from the dispenser platform spreading the powder over the building platform. The powder deposited onto the building platform is then selectively fused by the laser according to the layer data encoded in the STL file. Thereafter, the building platform moves down at a distance equal to the fused layer thickness,

and the recoater blade moves back to collect powder to deposit another layer of powder over the previous layer. This layer of powder is also selectively fused, as well as fused onto the previous layer, and the process is repeated until the final 3D part is produced. The excess powder not fused during the process is moved to the collector container. Successful part manufacturing through DLMS is influenced by parameters such as laser power, beam offset and diameter, layer thickness, scanning speed, and part orientation during manufacturing. The different parameters that influence the DMLS process are given in Figure 2.8.
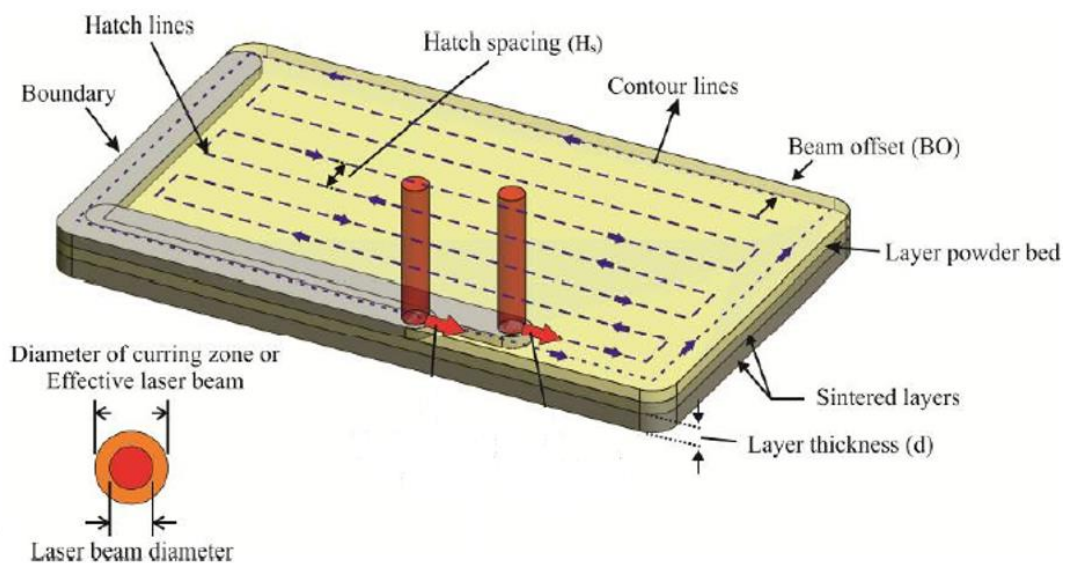
Figure 2.8: Illustration of the parameters relevant to the DMLS process **[33]**

The DMLS process uses scanning techniques such as a raster scan pattern to fuse the powder layers. Parameters such as the hatch spacing, hatch distance, laser beam diameter, and offset play a vital role when creating a DMLS part. The diameter of the fused zone is usually larger than the laser diameter. These differences in diameters necessitate compensation for the dimensional error. Therefore, the laser beam is shifted by half the curing width from the contour line. This is to ensure that the part produced corresponds with the dimensions of the original CAD design. This correction is referred to as the beam offset, which affects part manufacturing. If the beam offset value is too high or less than the corrected value, the powder particles would still be fused, leading to part inaccuracy [33].

The layer thickness is also an essential process parameter that needs careful control during the DMLS process. If the layer thickness is too large, there will not be enough adhesion between the layers of the part. This is because the laser energy may be insufficient and thus result in incomplete fusion of the part, which can lead to layer detachment [33]. If the laser power is too high for a specific layer thickness, it may result in a porous structure. Therefore, it is important that the laser power must be optimized so that a fused layer with completely fused powder particles can be produced.

Proper planning of the orientation of a part to be built through DMLS is essential for obtaining a successfully built part. This planning is needed because the recoater blade passes over the fused part while spreading the following powder layer from the dispenser platform to the building platform. As the recoater blade passes over the part, it may collide with the exposed layer with high force and deform the part shape at that layer, thus creating a part that deviates from the original CAD model. The blade may tend to bounce off a parallel wall, as shown in Figure 2.9 (a), and the section itself may not resist the force of the moving blade. A good practice is to orientate the part at an angle, as indicated in Figure 2.9 (b), so that the recoater blade only makes contact with a smaller area of the part and not the full face [34].
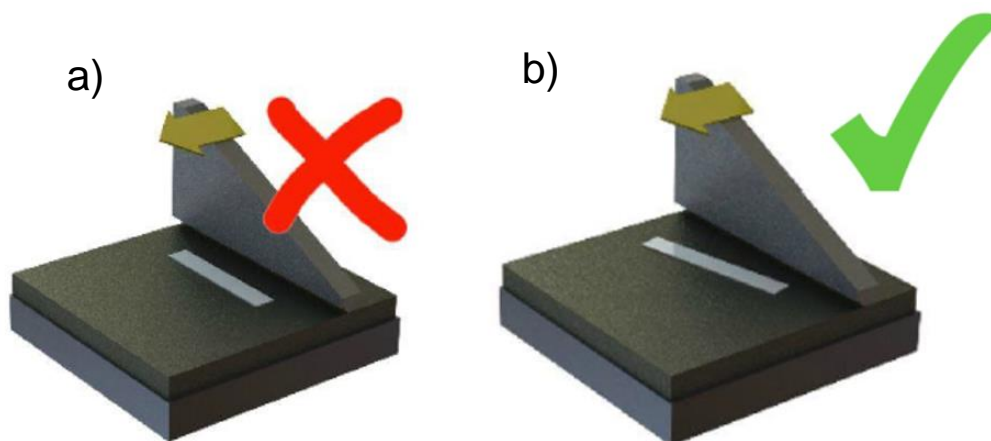
***Figure 2.9: Illustration of the part orientation in the DMLS process a) Bad part orientation b) Good part orientation* [34]**

2.6 The DMLS Ti6Al4V(ELI) alloy

The Ti6Al4V(ELI) alloy, also known as Titanium Grade 23 [35], is an *α+β* alloy. The abbreviation ELI stands for 'Extra Low Interstitial', meaning reduced concentration of the interstitial elements shown in Table 2.1 in the alloy to improve ductility and fracture toughness with some reduction in strength [36]. The microstructure of this alloy has a distorted HCP structure, designated as *α',* referred to as an acicular martensite microstructure [37]. An acicular martensite microstructure is a needle-like microstructure formed when the alloy is rapidly cooled from its melting point. During the DMLS process, rapid solidification of the molten layers occurs due to the high-temperature gradient inherent in the process. Figure 2.10 illustrates the formation of the martensitic microstructure in Ti6Al4V.
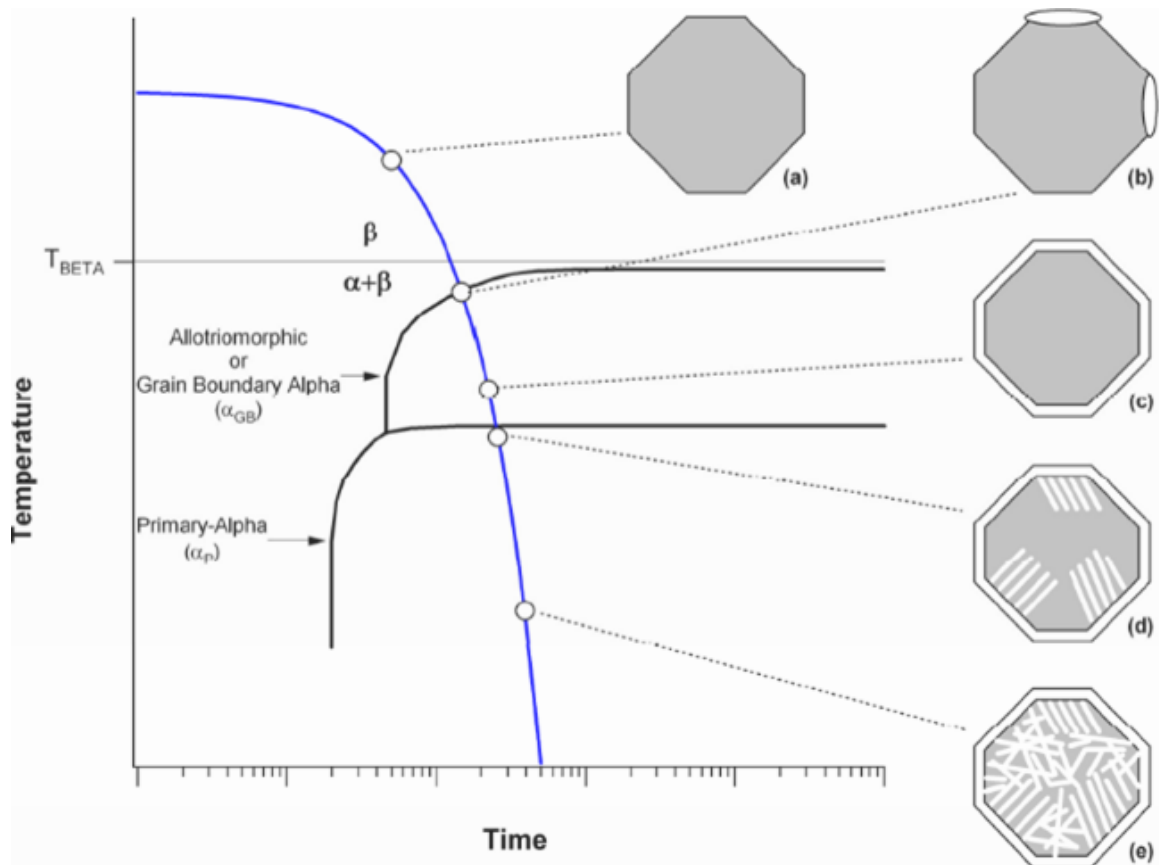
Figure 2.10: Martensitic transformation of Ti6Al4V [6]

As illustrated in Figure 2.10, Ti6Al4V solidifies when moderate cooling occurs from above the *α+β* transus temperature, as illustrated by image (a). When cooling proceeds below the beta transus temperature, a globular *α*-phase forms

when *α* grains start to nucleate along the *β* grain boundaries, as shown in image (b). The *α* phase forms along the specific planes of the *β* phase (image (c)), and it nucleates and grows inside the prior *β* grains to form *α*-laths (image (d) in Figure 2.10). During rapid cooling, the *α* nucleation and growth along and within the *β* grain boundaries increase [38], thus increasing the formation of *α* laths throughout the *β* grains, leading to an intertwined type of microstructure which is referred to as a basket-weave microstructure, as illustrated in image (e) in Figure 2.10. A diffusionless martensitic transformation occurs during rapid cooling to form the *α′* microstructure. The resultant microstructure is shown in Figure 2.11.

Figure 2.11: Basket-weave microstructure **[39]**

The *α′* basket-weave microstructure of Ti6Al4V parts produced through the DMLS process results in high tensile strength, low ductility, and internal thermal residual stresses in produced parts and thus requires heat treatment for tailoring of the microstructure for specific required properties [24][31][33]. In Figure 2.12, the equilibrium phase diagram of Ti6Al4V is presented, which shows that the microstructure of this alloy at room temperature consists of the *α* phase (HCP) with some retained *β* phase (BCC).
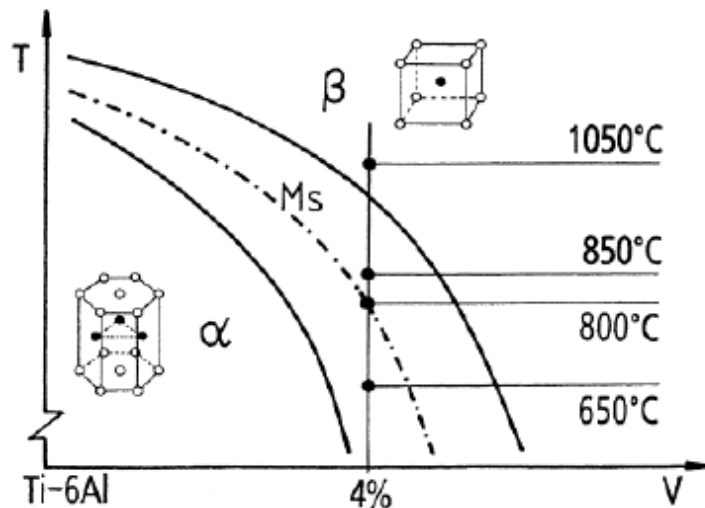
Figure 2.12: Phase diagram of Ti6Al4V **[40]**

Titanium in the alloy undergoes an *α* to *β* transformation, while aluminium at 6% and vanadium at 4% stabilize the *α* and *β* phases, respectively. The *α* stabilization leads to a reduction of density, resulting in the alloy being lighter in weight, while *β* stabilization lowers the *α+β to β* transformation temperature (*β transus)*, which facilitates the hot working of the alloy. Therefore, Ti6Al4V can exist in different morphologies, such as lamellar, equiaxed and bimodal microstructures [41]. Figure 2.13 shows the different microstructures of Ti6Al4V.
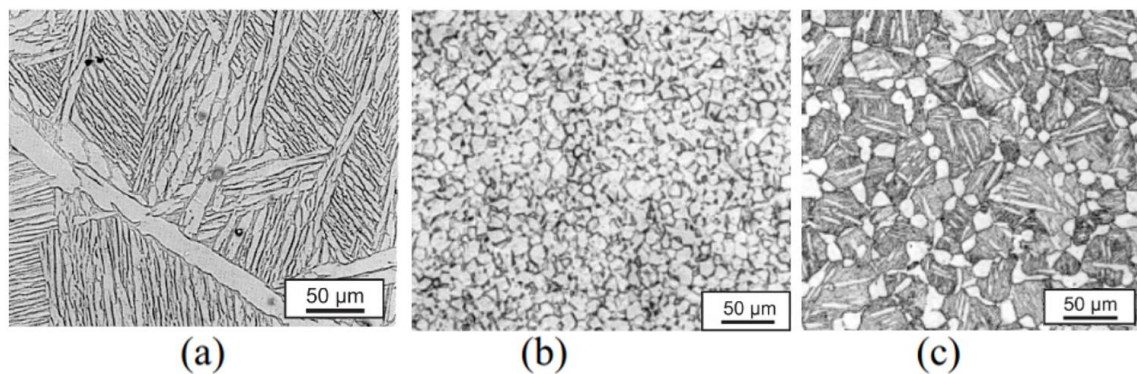
Figure 2.13: Ti6Al4V microstructures: a) lamellar structure, b) equiaxed structure and c) bimodal structure **[29]**

Each of the microstructures in Figure 2.13 is associated with different mechanical properties. The lamellar microstructure is generated upon cooling from above the *β*-phase field. When the temperature is below the *β* transus temperature, *α* nucleates at grain boundaries and then grows as lamellae into

the prior *β* grains. Slow cooling rates from the *β*-phase field result in lamellar microstructures, with the lamellae becoming coarser with a decrease in the cooling rate. As mentioned in the beginning of this section, rapid cooling or quenching creates a martensitic fine needle-like microstructure characterized by low ductility and moderate crack growth resistance [27][33] [42].

Equiaxed microstructures are the result of recrystallisation [29]. The alloy is heat-treated and furnace soaked within the *α+β* phase field, allowing the *α* grains to globularize [36]. This microstructure has a good balance of strength and ductility as well as fatigue strength [42].

Bimodal microstructures combine the characteristics of lamellar and equiaxed microstructures. To achieve the bimodal microstructures, the recrystallization and annealing would usually be performed just below the *β* transus temperature to allow the growth of *β* grains. This type of microstructure has high ductility, strength and impact toughness [29][33][43].

From this discussion, it follows that the microstructure of this alloy depends on the kind of heat treatment done on the material. The parameters, such as temperature, soaking time, and cooling time, are the controlled variables used in heat treatment processes, and they impact the resulting microstructures [44]. When the heat treatment temperature is increased, the *β* fraction of Ti6Al4V also increases, thus decreasing the *α* fraction. Vrancken et al. [44] studied this behaviour and found that the temperature impacts the microstructure of Ti6Al4V, thus affecting the mechanical properties. Their findings are shown in Figure 2.14.
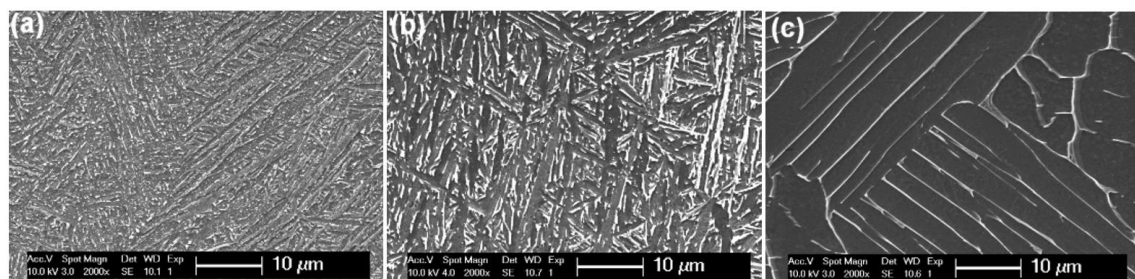
Figure 2.14: Microstructures of Ti6Al4V after heat treatment at different temperatures a) 780 °C b) 843 °C c) 1015 °C [44]

When comparing Figure 2.14 (a) and 2.14 (b), it is observed that the *α* platelets are fine in Figure 2.14 (a) and coarser in Figure 2.14 (b). This is because the heat treatment temperature in Figure 2.14(b) was higher than the heat treatment temperature in Figure 2.14 (a), although they were both below the *β* transus temperature. Furthermore, Figure 2.14 (c) indicates that a heat treatment above the *β* transus temperature results in a lamellar *α+β* microstructure.

Yadroitsev et al. [45] demonstrated that the yield strength of the DMLS Ti6Al4V alloy after heat treatment is usually lower compared to the as-built state. This is due to the coarsening of the lamellar microstructure during high-temperature heat treatment.

Malefane [36] also observed that applying heat treatment on DMLS Ti6Al4V parts below the *β* transus temperature does not yield significant change in the resulting microstructures but only alleviates the inherent residual stress resulting from the DMLS process. However, applying high-temperature annealing for two hours at 950 °C on the stress-relieved DMLS Ti6Al4V(ELI) specimens followed by furnace cooling transformed the *α′* grain structure to an *α+β* grain structure with increased ductility of about 20%, which exceeds the specified ductility in the ASTM F1472 – 08 standard [46].

Ductility coupled with high strength is an important material property during high-cycle fatigue (HCF) applications [47]. Fatigue cracks may nucleate more easily in martensitic Ti6Al4V due to its distorted basketweave microstructure, but the fatigue crack must grow through the path of the "basket form" of the microstructure, which is a tortuous path, making it difficult to grow and thus resulting in low fatigue crack growth [39]. However, this type of microstructure has low ductility but high strength, hence the use of heat treatment to obtain a balance of strength and ductility of the alloy.

2.7   Fatigue

2.7.1 Definition of fatigue

Fatigue is defined as the process of progressive localized permanent structural change occurring in a material subjected to fluctuating stresses and strains. These fluctuating stresses and strains may result in cracks or complete fracture after a sufficient number of stress-strain fluctuations [48]. For the current study, examples of fluctuating stresses can be caused by the take-off, landing, and taxiing loads on an aircraft nose wheel fork. Fatigue is more gradual in ductile materials where loads are low enough for the system to remain elastic except in the plastic zone in front of the crack tip, but when the crack reaches its critical length, the structure will be subjected to fast fracture [49]. Fatigue failure occurs in three stages, namely crack initiation, crack propagation and final fracture [50][51]. These can be portrayed in different zones, as shown in Figure 2.15.
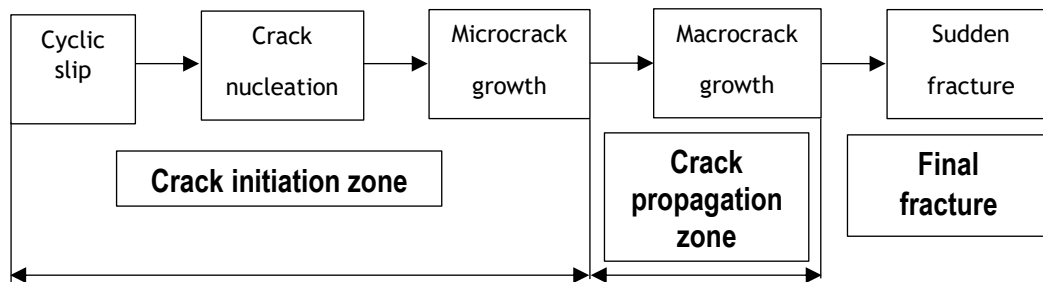
Figure 2.15: Three different stages of fatigue life (After [36]*)*

An area of high-stress concentration, such as notches, surface irregularities, and pores, will promote the crack initiation in a material. Cracks may also occur without any stress raisers but due to dislocations in slip planes resulting from cyclic stress or cracking along slip planes due to repetitive reversals of the active slip systems at a free smooth polished surface of a material [49]. Crack initiation is commonly known as stage 1 of fatigue failure, and it is greatly influenced by microstructural defects such as grain boundaries, inclusions, etc. As the crack length increases, the stress intensity increases and the crack direction becomes perpendicular to the applied stress and enters the crack propagation zone [48]. Crack propagation is divided into two types, namely

stable and fast crack propagation, see Figure 2.16. Stable crack propagation is known as stage 2 of fatigue failure and has a very weak resilience to microstructural defects [49]. This stage of fatigue crack growth produces fatigue features such as striations, which are not visible to the naked eye and require technologies such as SEM to distinguish them. Fatigue striations are located on the faces of tear ridges and are perpendicular to the direction of propagation of cracks and bow out from the site of initiation of cracks.
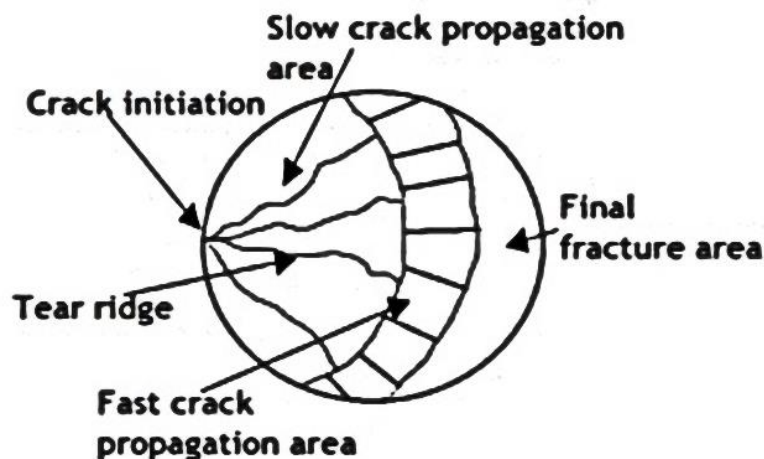
Figure 2.16: Schematic representation of a fracture surface representing three different stages of fatigue failure [36]

The second stage of crack propagation is fast crack propagation, commonly known as stage 3 of fatigue crack failure. This stage occurs when the crack length is closer to the critical area where the remaining material can no longer handle the stress intensity, which leads to a final fracture [48]. The final fractured area can either be ductile or brittle in nature. Ductile fractured areas display cup and cone fracture features because the material absorbs more energy before fracture, while brittle fractured areas are normally flat because the cracks quickly propagate across the section, along or through the grain boundary of the material, causing a catastrophic failure [48][52].

2.7.2 Fatigue failure of the as-built DMLS Ti6Al4V parts

The major challenge in DMLS as-built parts is poor fatigue behaviour related to their rough surfaces [5]. Powder distribution onto the building substrate

(recoating) and the build orientation impacts the staircase effect (visible layer marks on the part caused by an offset between the layers when forming a curvature, creating a rough surface). The surface roughness depends on the slope of a layered surface of a DMLS part [52]. This is illustrated in Figure 2.17.
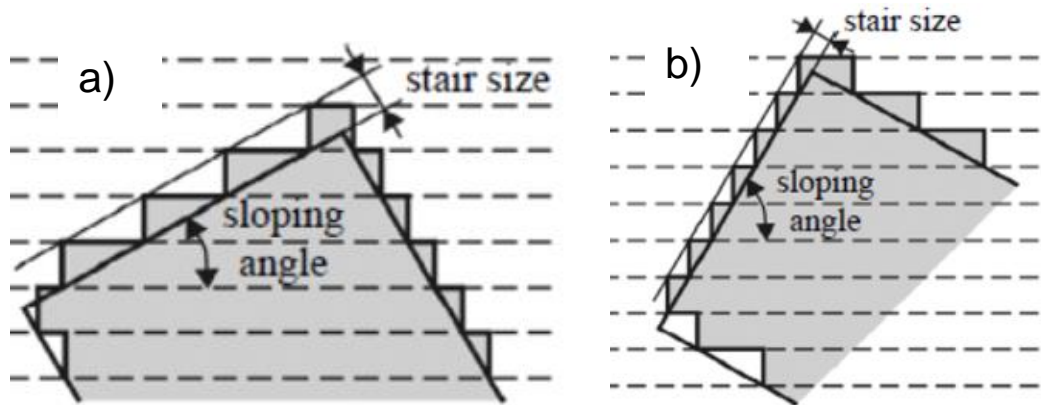
Figure 2.17: Staircase effect a) less inclined slope with more surface roughness b) more inclined slope with less surface roughness [52]

Surface topography features consisting of small radii of curvature act as local notches and create local stress concentration sites, which may lead to crack initiation at the as-built surface [53]. Therefore, these features negatively impact the fatigue life of Ti6Al4V parts produced through LPBF [7][8]. Similarly, the lack of fusion of powder particles on the as-built surface also directly affects the surface roughness of the end product [54]. The surface roughness caused by these features depends on the LPBF machine parameters, such as the thickness of the built layer, the allowable powder size distribution, and the laser energy [55].

Creating a smooth LPBF part surface implies additional cost because specialized machining or polishing must be implemented, and it might even be impossible to do with complex-shaped components. Such post-LPBF processes should be avoided to retain the economic advantage of using LPBF to produce complex-shaped aircraft structural components [7].

Kahlin et al. [56] reported on the fatigue behaviour of SLM Ti6Al4V. Comparing the fatigue strength of as-built (AB) and machined specimens, they found that surface roughness contributed most significantly to the fatigue properties and reduced the fatigue limit by approximately 45%, as shown in Figure 2.18.
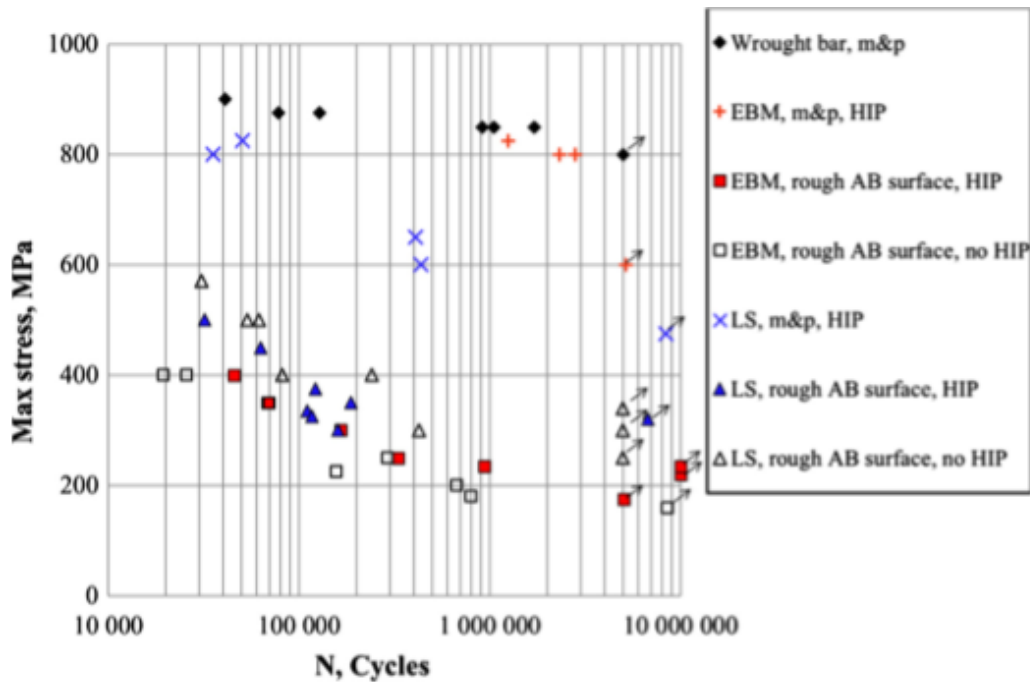
Figure 2.18: Fatigue life of EBM and SLM (LS) specimens with machined and polished (m&p) surfaces vs rough as-built (AB) surfaces **[56]**

The endurance limits of the as-built specimens shown in Figure 2.18 range between 200 and 400 MPa. Wycisk et al. [57] also reported an endurance limit of 210 MPa for DMLS Ti6Al4V specimens with inherent surface roughness and 500 MPa for polished specimens. This emphasizes the importance of the surface condition for fatigue-sensitive parts intended for use in their as-built condition. It is also relevant for parts with complex internal features where surface finishing may not be possible.

2.8   Residual stress

Residual stress is the internal stress that is locked into a body after it reaches equilibrium [58]. The common cause of residual stress is manufacturing processes such as casting, welding and the DMLS process due to the high localized heating involved in the process [10]. Unlike external stresses, residual stresses are less predictable and can be either tensile or compressive. The effect of residual stress can either be beneficial or disadvantageous. For example, tensile residual stresses are usually caused by processes such as aggressive grinding, which creates uneven surfaces that may promote crack initiation. In this case, the residual stress is disadvantageous because it

decreases the fatigue strength and consequently contributes to the failure of the part [59].

Residual stresses are categorized into three types depending on their nature: Type 1, 2, and 3 [10]. Type 1 residual stresses are macro-stresses that occur over distances that involve many grains within a material. Type 2 are micro-stresses caused by the differences in the microstructure of the material and occur over distances comparable to the grain size of the material. Type 3 are sub-micro stresses that occur inside a grain due to the imperfections within the grains [7]. Knowing the origin of residual stress helps the designer or manufacturer to prevent or accommodate its effect. For instance, finite element modelling (FEM) packages such as ABAQUS are used to simulate the resulting residual stresses prior to actual LPBF building processes and play a significant role in preventing failure during the processing of components [60].

As discussed in section 2.5, the DMLS process uses high-power laser energy input to build parts. This highly concentrated energy input always leads to residual stress and sometimes crack formation during processing and after separation from the supports [7]. The formation of residual stress in the DMLS process is due to the high-temperature gradient between the layers where compressive stresses are induced in the melt zone, and tensile stresses are induced in the cooler underlying layers during heating [36]. This phenomenon is illustrated in Figure 2.19.
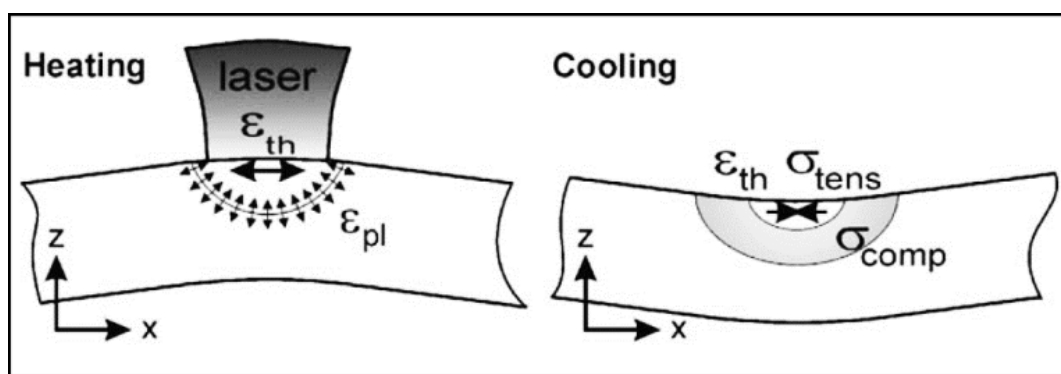
Figure 2.19: Schematic of the state of stress of a layer during heating and cooling [10]

When the top molten layer is fused into the previously solidified layer, it will be restricted in thermal expansion by the previous layer, and this will cause compressive stress in it. During the cooling process, see Figure 2.19, the lower layer restricts the upper layer from thermal contraction resulting in residual stress in both layers. The lower layer will experience compressive stress, and the upper layer will be under tensile stress [27][36].

It is clear that the residual stress in LPBF parts is induced by thermal gradients inherent in the process. This indicates that heat treatment can also be used to reduce the residual stress in the parts. The thermal stresses induced in LPBF parts cause warpage when the parts are removed from the substrate directly after the LPBF process. This is because the part would still be under the residual stresses induced during the heating and cooling. If a stress-relieving heat treatment is applied before the part is removed from the substrate, the residual stress can be reduced, and warpage can be limited [36][61]**.**

2.9   Design for additive manufacturing

Design for AM (DfAM) is essential for proper LPBF part manufacturing. Customized design approaches and optimization are required to ensure that the part design includes the design freedom provided by AM technologies and satisfies the AM manufacturing constraints.

In the DMLS process, factors such as the build platform, building orientation, part strength during the build process, use of support structures, and the post-processes need to be considered. Failure to consider these factors could result in a deformed part or a part with various defects. For example, the build orientation affects the surface finish on the end product due to the staircase effect. On the other hand, support structures prevent the part from deforming and warping during the build process since they allow dissipation of heat away from the newly formed geometry and provide temporary support, thus maintaining the geometry of the part [34]. However, the attachment points of these structures negatively affect the surface finish. As a result, the choice of type and positioning of support structures is very important.

Furthermore, the design requirement for the component and its application must be considered in the DMLS design strategy. For an aerospace part such as the AHRLAC nose wheel fork, understanding the operating conditions is essential. In addition, the mass of the nose wheel fork is an important consideration. The industry uses specific methods to provide the designer with a systematic design optimization methodology. Brandt et al. [62] developed a generic AM design optimization methodology incorporating topology optimization. Topology optimization is a simulation-driven design tool concentrating on the material distribution and structural connectivity in the design domain space [1][62]. A lightweight part can be produced while maintaining its strength, and the material needed to produce the end product can be significantly reduced.

Vayre et al. [63] recommend four steps in the design methodology. These include the initial shape generation and geometrical parameter definition, followed by shape optimization through tuning the AM process parameters and the validation of a part design. Lettori et al. [64] proposed an approach to assess the compatibility and suitability of a part for AM production through a set of reference questions and a compliance index, which was validated with case studies found in a literature review they conducted. Other researchers, such as Zhang et al. [65], also proposed a framework to assess the design from the perspective of the AM planning process by checking and verifying the suitability of the part design for AM production. Clearly, a framework can help designers benefit from the advantages of AM processing while enabling them to avoid the potential difficulties resulting from the limitations of AM technology.

2.10 Summary

Through the literature study, insight was gained into the importance of the integrity of the nose wheel fork for airplane safety, and the causes of failure were identified. Understanding the titanium alloy and the DMLS technology to be used for the scaled-down nose wheel fork was essential for the project planning and execution of the study. The literature on the characteristics of the DMLS Ti6Al4V(ELI) alloy and the resulting mechanical properties was

reviewed, and understanding was gained on how post-process heat treatment can be used to optimise the mechanical properties of DMLS Ti6Al4V(ELI)-produced parts to improve their fatigue properties. Understanding DfAM also raised awareness of the importance of part geometry, which affects the surface roughness of DMLS-produced parts.

CHAPTER 3: METHODOLOGY

3.1 Approach

Qualifying components for the aerospace industry require extensive testing, especially if they are structural parts in the airframe of an aircraft. As mentioned in section 1.5, this study was done on a scaled-down prototype nose wheel fork produced through DMLS of Ti6Al4V(ELI), and the performance testing of the component was limited to static testing. The research methodology was divided into three phases. Phase 1 dealt with building the prototype together with the standard test specimens. Phase 2 entailed the characterization and mechanical testing of the standard test specimens, and Phase 3 consisted of the design and manufacturing of the test jig, followed by static performance testing of the scaled-down nose wheel fork. A schematic illustration of the research methodology is shown in Figure 3.1.

Phase 1: DMLS building and heat treatment of test specimens and scaled-down prototype.

Specification and design of test specimen geometry, build orientation and number of specimens

↓

Obtain prototype CAD model and determine AM build orientation

↓

DMLS building of the scaled-down prototype and test specimens

↓

Post-process heat treatment of DMLS built parts

1. Stress relieving (attached to platform)

2. High temperature annealing
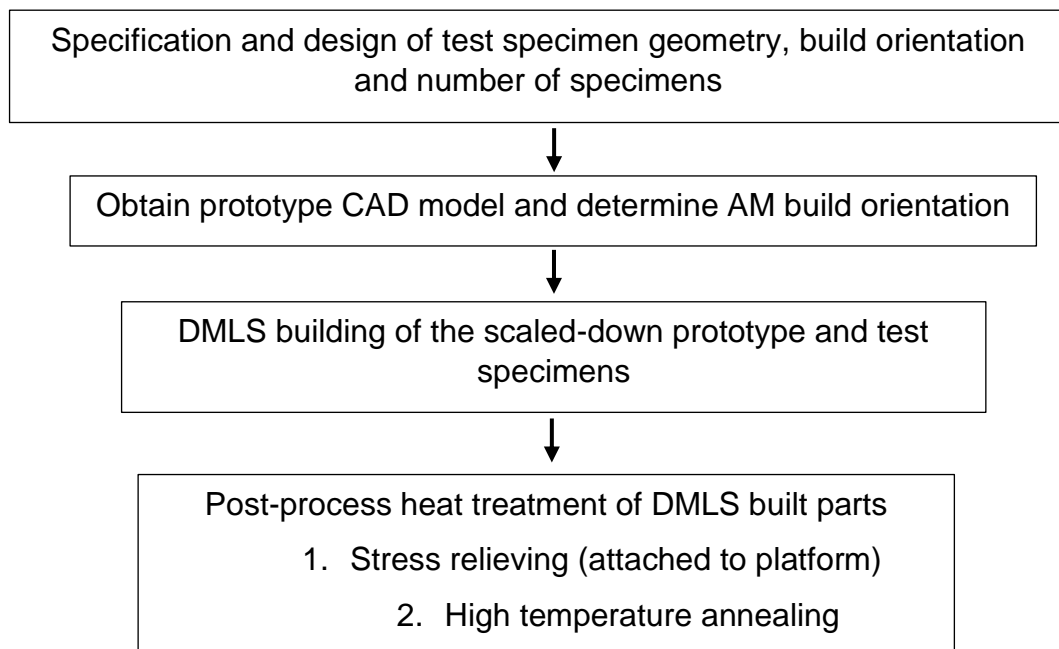
Phase 2: Characterization, mechanical testing and fractography of test specimens.

Characterization of test specimens

↓

Machining of the grip-ends on test specimens

↓

Tensile and fatigue testing of the specimens

↓

Fractographic analysis of the fractured fatigue specimens using scanning electron microscopy

Metallographic analysis of the fractured fatigue specimens using optical microscopy

Phase 3: Static performance testing of the scaled-down prototype

Machining of the axle holes in the scaled-down prototype

↓

Design and manufacturing of the test jig

↓

Performance testing of the scaled-down prototype in the test jig

↓

Assessment of results and conclusion

Figure 3.1: Schematic overview of the methodology followed for this research project

3.2 Building and heat treatment of test specimens and scaled-down prototype

3.2.1 DMLS building of test specimens and scaled-down prototype

The optimized CAD model of the scaled-down prototype nose wheel fork was obtained from Mr L. F. Monaheng, see Figure 3.2.
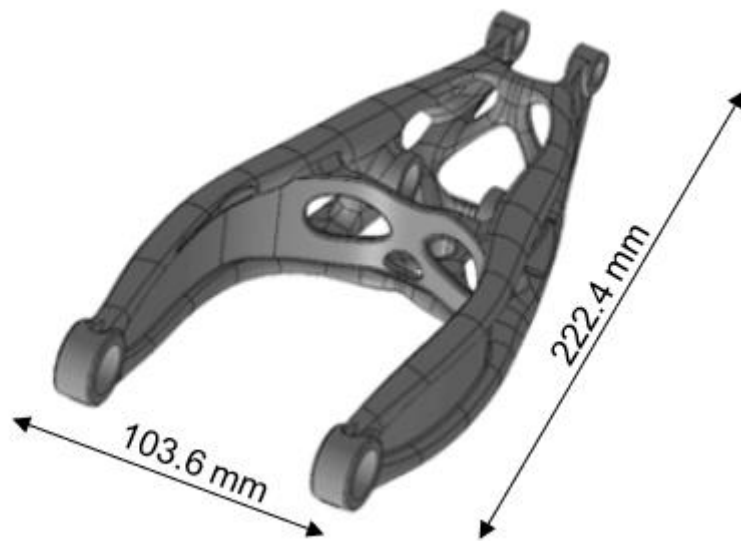
Figure 3.2: CAD design of the scaled-down prototype nose wheel fork [1]

The scaled-down nose wheel fork was designed through topology optimization and built together with 21 HCF Ti6Al4V(ELI) test specimens at the Centre for Rapid Prototyping and Manufacturing (CRPM) at Central University of Technology, Free State (CUT) using an EOSINT M280 DMLS machine. The test specimens were designed according to the ASTM E466 standard for fatigue testing of metallic materials [66]. The design drawing is given in Appendix 1. The EOSINT M280 machine was set to the standard parameters of the supplier. See Table 3.1 for the process parameters.

Table 3.1: Process parameters for the DMLS process

Parameter	Laser Power (W)	Beam Diameter (µm)	Scanning Speed (mm/s)	Layer thickness (µm)	Hatch spacing (µm)	Powder bed temperature (℃)
Value	170	75	1 400	30	100	40

Spherical Ti6Al4V(ELI) powder, supplied by TLS Technik GmbH & Co. Spezialpulver KG, Bitterfeld-Wolfen, Germany, with an average powder particle size of less than 45 µm was used to build the component and test specimens. The powder used in this study was from the batch used in the study of Monaheng et al.[67], and its composition, as determined by an independent laboratory through inductively coupled plasma - optical emission spectroscopy (ICP-OES), is given in Table 3.2.

Table 3.2: Chemical composition of TLS Technik Ti6Al4V(ELI) powder

Materials	Titanium (Ti)	Aluminium (Al)	Vanadium (V)	Iron (Fe), max	Oxygen (O), max	Nitrogen (N), max
TLS powder [67]	90.30%	5.56%	4.02%	0.23%	0.12%	0.04%
ASTM F3001 – 14 [68]	Balance	5.5–6.5%	3.5–4.5%	0.25%	0.13	0.05

Two building platforms were used to achieve a total of 21 specimens due to the limited building area of the EOSINT M280 DMLS machine. Of the 21 HCF test specimens, seven were built in the X-orientation (long axis along the X-direction), another seven in the Y-orientation (long axis along the Y-direction) and the third set of seven in the Z-orientation (long axis along the Z-direction), as illustrated in Figure 3.3.
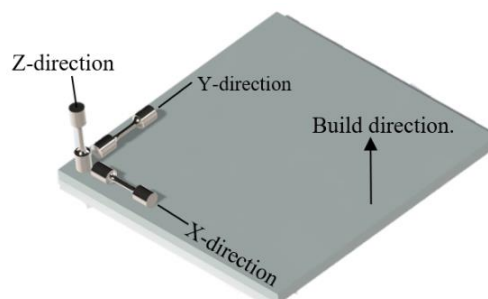
Figure 3.3: Illustration of DMLS Ti6Al4V(ELI) test specimen orientations on the building platform

To confirm the build quality, nine cylindrical tensile test specimens were built on platform 1 with the nose wheel fork in the same orientations as the HCF specimens (three in each orientation). Platform 2 was for 21 HCF test specimens. Similar to the HCF test specimens, the tensile test specimens were also built in the final geometry given in Appendix 1. The test specimens were tested in their as-built geometry, which implied that no post-process machining on the gauge lengths of the specimens was done after DMLS building and post-process heat treatment. Machining was only done on the grip ends of the specimens for clamping them in the fatigue testing machine. This allowed the investigation of the effects of as-built surface roughness on the fatigue properties of the DMLS Ti6Al4V(ELI) specimens. Therefore, the Z-specimens were built upright, with a vertical support cylinder around the gauge length to support the upper grip parts and maintain the geometry of the Z-specimens, as shown in Figure 3.4 (a). These support structures could be removed with pliers, not affecting the surface of the gauge length. The X- and Y-specimens had support structures directly supporting the gauge length, as shown in Figures 3.4 (b) and (c). While these structures could be easily removed, they left attachment marks that created rough surfaces on the gauge lengths of the specimens. In addition, there were also two built-in types of support structures (pin support) outside the gauge length of the X- and Y-specimens. This type of support was used to maintain the geometry of the gauge length by preventing warping of the test specimens.
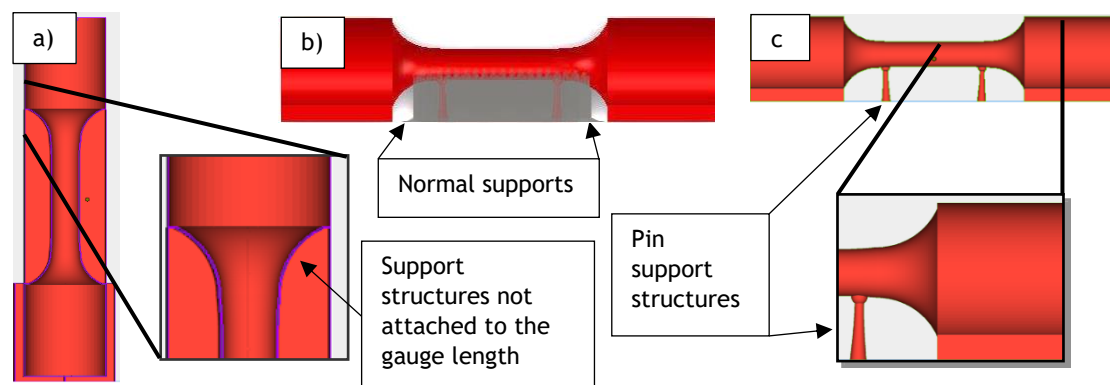
Figure 3.4:Test specimens with support structures. a) Z-specimen b) X/Y-specimens showing normal supports on gauge length c) Pin supports on X/Y-specimens

3.2.2 Post-process heat treatment of DMLS-built parts

After the DMLS process, a two-stage heat treatment was performed on the built parts. Firstly, to relieve the residual stress, the parts (still attached to the build substrate) were heated to a temperature of 650 °C at a rate of 3.6 °C/min in a T-M Vacuum Products Inc., Super Series Vacuum Furnace, SS12/24-13MDX. They were kept at 650 °C for three hours and furnace-cooled to room temperature. Thereafter, the parts were cut from the build substrate by wire electrical discharge machining, and the support structures were removed manually with long-nose pliers in the Product Development Technology Station (PDTS). Subsequently, the standard test specimens and the prototype were submitted to a high-temperature annealing heat treatment, which was done as follows: The parts were heated at a rate of 5.2 °C/min to a temperature of 950 °C in the vacuum furnace and held isothermally at that temperature for two hours before furnace cooling to room temperature. Figure 3.5 shows the parts inside the vacuum furnace.
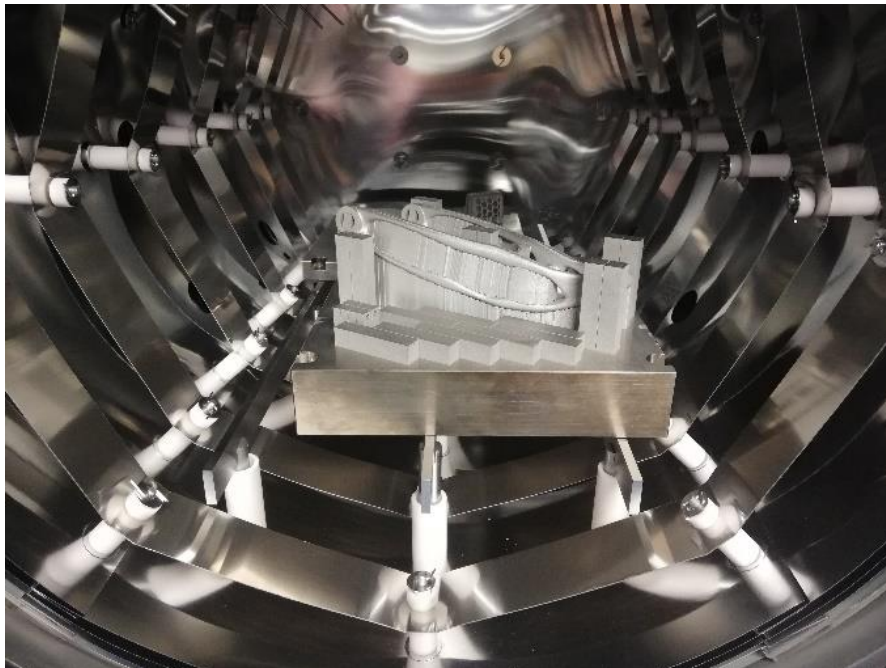
Figure 3.5: Ti6Al4V parts inside the T-M Vacuum Products Inc. Super Series Vacuum Furnace, SS12/24-13MDX, prior to the stress-relieving heat treatment

3.3 Characterization and mechanical testing of the test specimens

The chemical composition of the Ti6Al4V(ELI) powder used to build the test specimens, as well as the density of the built parts, was important to characterize before the specimens could be tested to obtain the mechanical properties of DMLS Ti6Al4V(ELI).

3.3.1 Surface roughness characterization of the test specimens

It was expected that the test specimens would have a quantifiable difference in surface roughness due to the different support structures used for the three orthogonal build orientations. However, due to the shape of the as-built specimen, it was not feasible to use the surface roughness tester on the gauge length of the test specimens after the DMLS build. This tester ideally requires a flat surface to provide accurate surface roughness values. Therefore, a JEOL JSM-7800F scanning electron microscope (SEM) was used to obtain images from which semi-quantitative assessments of the surface roughness of the gauge length could be made. By comparing images at the same magnification, the differences in the surface finish of different specimens could be determined.

3.3.2 Micro-CT scanning of the test specimens

Representative test specimens, one from each build platform for each of the build orientations (X, Y and Z), were selected and sent to the South African Nuclear Energy Corporation (NECSA) for X-ray micro-computed tomography (micro-CT) scanning to determine the porosity levels. The micro-CT analysis was performed using a Micro-focus X-ray Machine type NIKON XTH 225 ST. It was set to a current of 200 µA, acceleration potential of 185 kV and exposure time of four seconds per projection at 2 000 projections per sample. A scanning resolution of 8.2 µm was used, and scans were only done on the gauge length areas of the test specimens, which were sections within the 13 mm length and 4.37 mm diameter area shown in Appendix 1. All the scans were performed to evaluate the level and distribution of porosity. These micro-CT analyses were

used as a quality control measure to confirm that the DMLS Ti6Al4V(ELI) test specimens and scaled-down nose wheel fork component were of the same good quality as other parts CRPM produces with the EOSINT M280 DMLS machine.

3.3.3 Mechanical testing of the test specimens

The test specimens were subjected to tension and axial force-controlled fatigue testing in the Mechanical Testing Laboratory of the CSIR. A total of nine specimens (three specimens per build orientation) were subjected to tensile testing using an Instron 1432 servo-hydraulic testing machine. The tensile tests were performed according to the ASTM E8 standard for testing metallic materials. The remainder of the 21 test specimens (nine specimens per build orientation) were then subjected to high-cycle axial force-controlled fatigue testing, which was performed according to the following criteria:

Table 3.3: Test criteria for the axial force-controlled fatigue testing

Testing standard	ASTM E 466 – 15 and ISO 1099
Testing Equipment	50kN Instron 1432, axial, servo hydraulic
R-ratio	0.1
Control mode	Stress control mode
Frequency	10 Hz
Temperature	20 ± 2 °C
Run-out	5 x 10^6 cycles

The HCF test regime was informed by the study of Malefane et al. [51] on their machined and polished HCF test specimens, which could reach a run-out of five million cycles at the maximum stress of 450 MPa. In the current study, the first specimen (Z4) was tested at maximum stress of 450 MPa, and it failed after 50 142 cycles. The maximum stress level was then reduced by 7.1% from 450 MPa to 418 MPa for testing the next specimen (Z5), which failed after 61 584 cycles. A significant reduction of 20% from the initial maximum stress of 450 MPa was then applied on the third specimen (Z6), and improvement in the number of cycles to 122 595 cycles was achieved. The maximum stress was continuously lowered based on the resulting number of cycles to failure until the stress level was 50% of the initial maximum stress of 450 MPa, where the run-

out was achieved on the Z9 specimen. Table 3.4 shows the stress levels for the Z-orientation specimens.

Table 3.4: Maximum stresses for fatigue testing of Z-orientation DMLS Ti6Al4V(ELI) test specimens

Specimen designation	Maximum stress (MPa)
Z8	225
Z9	250
Z7	270
Z10	300
Z6	360
Z5	418
Z4	450

Based on the behaviour of the Z-orientation test specimens, the stress range for the X- and Y-orientation specimens was derived. Therefore, the testing of the next set of specimens (X-orientation) was started at a maximum stress of 360 MPa. The range of maximum stress levels for the X-orientation specimens is shown in Table 3.5, and those for the Y-orientation specimens in Table 3.6.

Table 3.5: Maximum stresses for fatigue testing of X-orientation DMLS Ti6Al4V(ELI) test specimens

Specimen designation	Maximum stress (MPa)
X8	190
X10	200
X7	210
X6	230
X9	270
X5	300
X4	360

Table 3.6: Maximum stresses for fatigue testing of Y-orientation DMLS Ti6Al4V(ELI) test specimens

Specimen designation	Maximum stress (MPa)
Y7	190
Y10	200
Y6	230
Y8	250
Y9	270
Y5	300
Y4	360

3.3.4 Fractography of the test specimens

The fracture surfaces of selected HCF DMLS Ti6Al4V(ELI) test specimens were analyzed in a JEOL JSM-7800F SEM at the University of the Free State (UFS). The analysis was done using the secondary electron imaging (SEI) mode of the SEM with accelerating voltages of 10–20 kV at working distances of up to 50 mm.

3.3.5 Metallographic analysis of the test specimens

Metallographic analysis was performed using a ZEISS Axio A1 optical microscope. Test specimens were prepared by cutting cross sections using an Accutex AU-500 iA electron discharge wire-cutting machine after HCF-testing the test specimens. The cross sections were cut from one part of each fractured specimen next to the fractured area, as indicated in Figure 3.6.

Figure 3.6: Illustration of the cross sections cut on HCF test specimens using an AU-500 iA Accutex wire-cutting machine

The cross sections were then mounted in a non-conductive Multifast resin in a Citopress-1 machine. A Struers Tegramin-25 machine was used to grind and polish the specimen surfaces. The grinding was firstly done with a silicon carbide grinding paper of 320 grit, followed by polishing on an MD-largo disc using Diapro diamond suspension of 9 μm particle size. The final finish was done by polishing the specimens with an MD-Mol cloth using Diapro diamond suspension of 3 μm particle size. The specimens were mirror polished using an MD-Chem disc with OP-S suspension as a lubricant. Finally, after polishing, the test specimens were etched in an ESCO fume hood using Kroll's reagent to reveal the microstructures of the test specimens.

3.4 Performance testing of the prototype scaled-down nose wheel fork

Performance testing of the scaled-down nose wheel fork was done in the Mechanical Engineering Heavy Machine Laboratory at the University of Pretoria (UP). The laboratory has unique facilities for dynamic structural testing under simulated operational conditions for various applications. The performance testing plan was developed in collaboration with the UP team (see Appendix 2 for the test instruction plan). A test jig that allowed simulation of the operational conditions of the nose wheel fork during testing was designed and manufactured in the PDTS at CUT.

3.4.1 CAD design and manufacturing of a test jig

The test jig was designed to fit the applicable testing equipment in the Mechanical Engineering Heavy Machine Laboratory at UP. Figure 3.7 shows a CAD model of the test jig and the physical image.
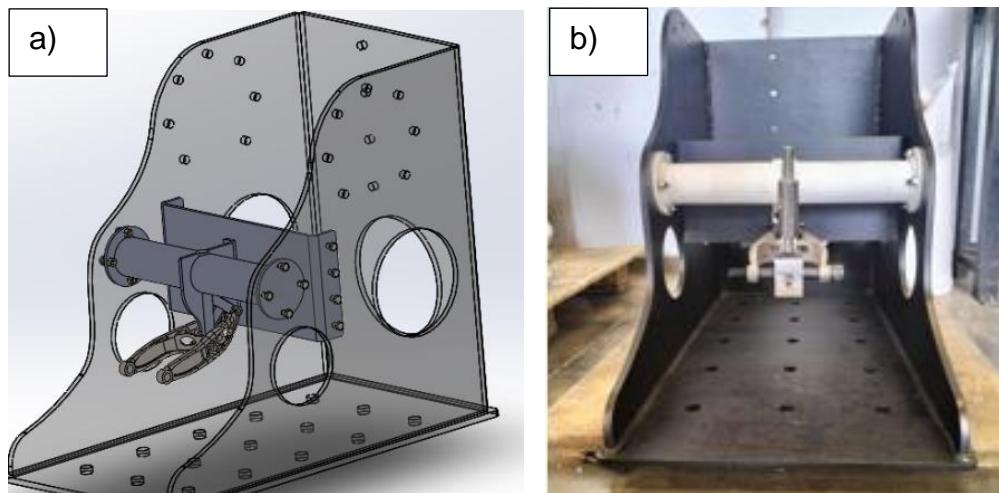
Figure 3.7: Landing gear fork performance test jig: a) CAD model b) image of the manufactured jig

3.4.2 Performance testing of the scaled-down prototype nose wheel fork

This study was limited to the static performance testing of the scaled-down nose wheel fork, which forms part of Mr L. F. Monaheng's doctoral study. In the

current study, the maximum operational static loads acting in the X-, Y-, and Z-directions were applied on the DMLS Ti6Al4V(ELI) nose wheel fork. The loads were applied in the positive and negative direction for each load case, with the X-load case first followed by the Z- and Y-load cases. These tests were done to assess the potential of the scaled-down nose wheel fork to meet the requirements for such a structural aircraft component.

To capture strain values experienced by the scaled-down nose wheel fork while loads were applied, strain gauges were bonded on the specific areas of the nose wheel fork, which were expected to have high strain. A total of four strain gauges were used. Two were rosette gauges, and the other two were single-grid gauges. Therefore, there were eight strain gauge readings in total. The rosette strain gauges had 120 ± 0.3% ohm resistance, and the single-grid strain gauge had 350 ± 0.3% ohm resistance. The locations of all strain gauges are shown in Figure 3.8. The higher magnifications show the exact positions of these gauges.
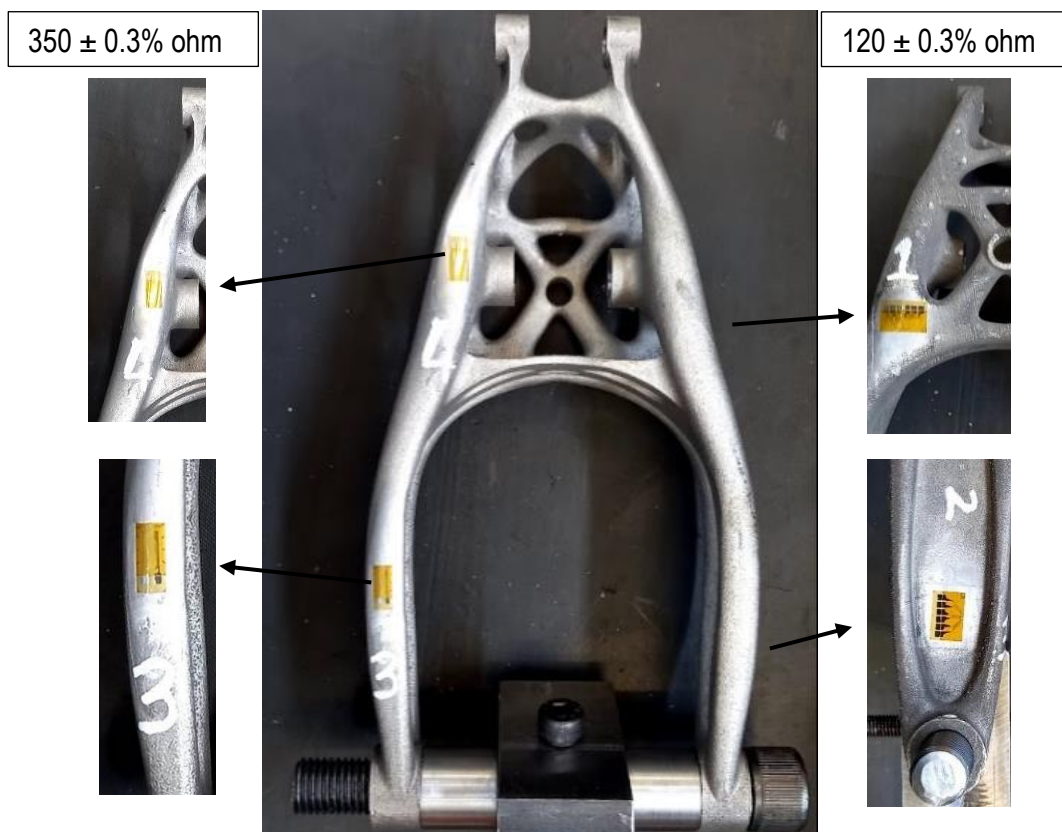
Figure 3.8: Strain gauges positioned on the scaled-down nose wheel fork. Gauges 1 and 2 were placed on the side of the nose wheel fork

All strain gauges were connected to quarter bridge circuits (SCM-SG120 and SCM-SG350). Each quarter bridge circuit was then connected to a specific channel on a Universal Amplifier (MX840 8-channel amplifier). The amplifier was connected to a Quantum X data recorder system (CX 22W). The technical specifications of the Universal Amplifier (MX840 8-channel amplifier) and Quantum X data recorder (CX 22W) are presented in Appendix 3 and 4, respectively. Figure 3.9 shows the schematic of the experimental setup.
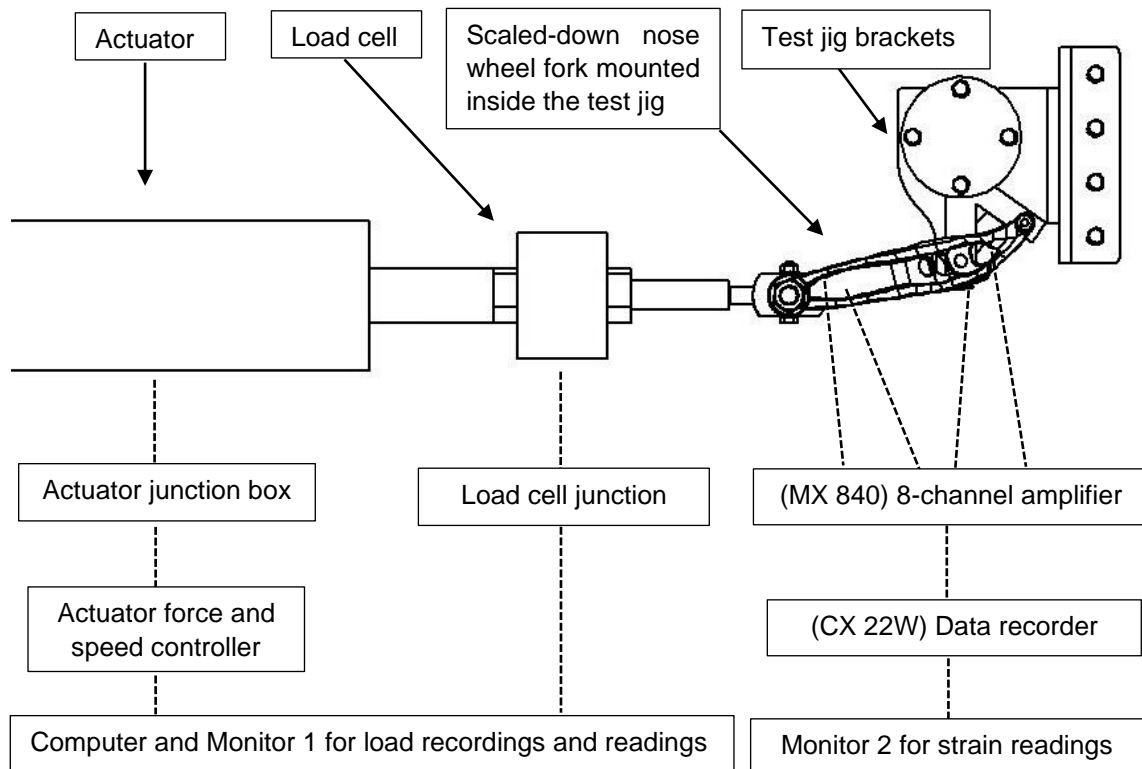
Figure 3.9: Schematic representation of the experimental layout and data recording. (Dashed lines represent electrical connections.)

The test jig was mounted on the isolated test floor of the laboratory, which had a T-slot base where studs were used to keep the jig in a fixed position when loads were applied. See Figure 3.10 for this setup for the X-direction of loading. The actuator holder bracket was also mounted on the isolated bed using the studs.

Actuator Load cell Scaled-down nose wheel fork in the test jig
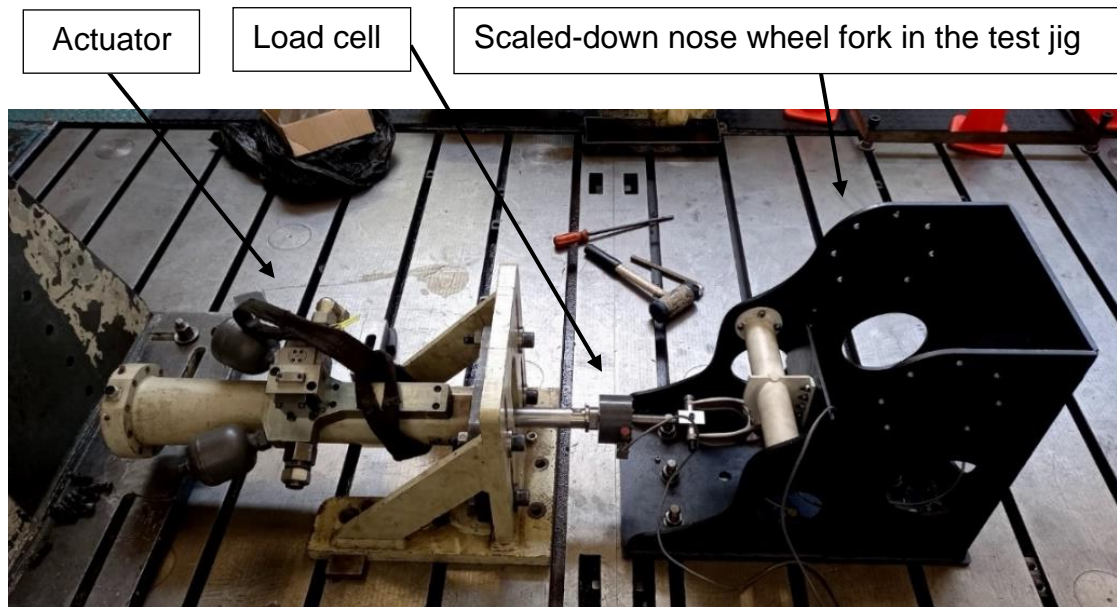
Figure 3.10: X-load case experimental testing setup for the performance test of the scaled-down nose wheel fork on the isolated floor in the laboratory at UP

The performance tests on the scaled-down nose wheel fork were done at loads 40% of the magnitude of the maximum loads on the full-scale nose wheel fork. The latter was provided by the manufacturer of the ARHLAC, Aerosud. This resulted in static loads of Fx = 5 584 N, Fy = 3 358 N, and Fz = 8 285 N applied on the scaled-down nose wheel fork. Figures 3.11 and 3.12 illustrate the experimental test setup in the Y- and Z-loading direction, respectively.
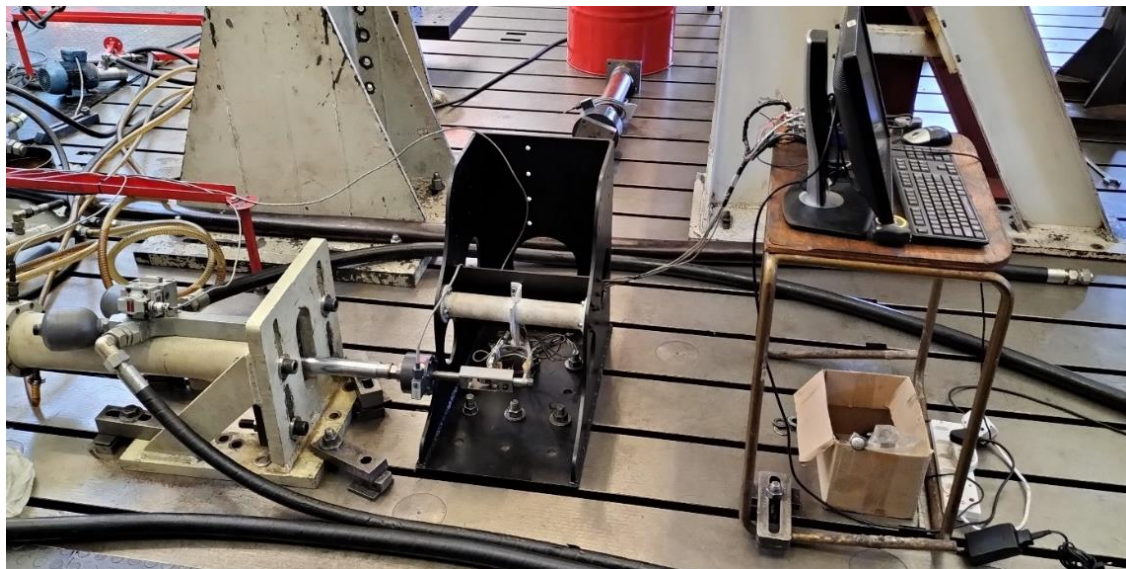
Figure 3.11: Y-load case experimental testing setup for the performance test of the scaled-down nose wheel fork on the isolated floor in the laboratory at UP
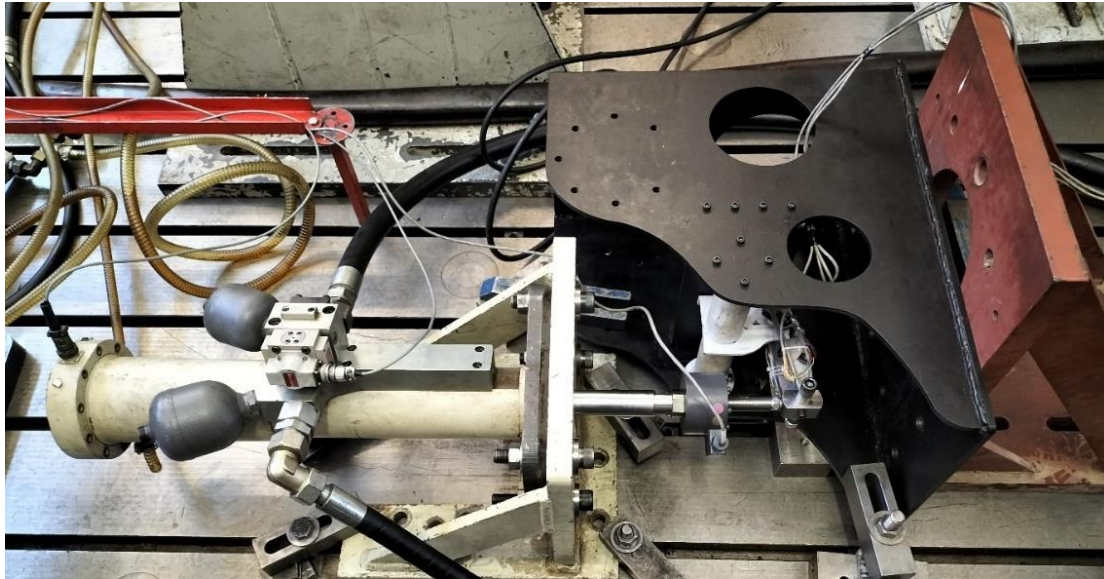
Figure 3.12: Z-load case experimental testing setup for the performance test of the scaled-down nose wheel fork on the isolated floor in the laboratory at UP

The applied load on the fork was gradually increased for each load case until the required load level was reached. The load was stopped at the required level for a few seconds, and the strain readings were collected at the different positions on the fork where the strain gauges were mounted for strain measurements. This data was used to assess the static test performance of the scaled-down nose wheel fork produced in Ti6Al4V(ELI) through DMLS.

3.4.3 Data preparation for analysis on performance testing of the prototype scaled-down nose wheel fork.

The data collected from the performance tests of the Ti6Al4V(ELI) scaled-down nose wheel fork produced through DMLS was analyzed in two phases. Firstly, all data points from the actuator controller were collected, and sinusoidal load curves were plotted to simulate the compressive and tensile static loads applied on the fork as a function of time. Secondly, the corresponding strain curves were plotted from data collected from the strain gauges. The load and strain curves were compared per load to evaluate the correct functionality of the measuring equipment. As the strain values increased with the increased applied loads, it became clear that the measurement was done correctly. The detailed procedure for the data preparation for analysis is provided here for the X direction of loading.

3.4.3.1 Preparation of data for X-direction of loading – actuator controller

The actuator controller only recognises the voltage reading as the input load the system will apply to the fork. Therefore, all the available loads from Aerosud were converted from kilonewtons to voltages based on equation 3.1.

1 Volt = 2 kN... (3.1)

The maximum load in the X-direction of testing was 6 kN. This maximum load was divided into 20% intervals, and a series of static loads were applied using equation 3.1, as shown in Table 3.7.

Table 3.7: Applied loads in the X-direction for static testing of the DMLS Ti6Al4V(ELI) prototype nose wheel fork

Load divisions	Controller reading (V)	Force (kN)
1	0.6	1.2
2	1.2	2.4
3	1.8	3.6
4	2.4	4.8
5	3	6

The static test for Load division 1 of 1.2 kN was performed by applying a compressive force starting from the zero position of the controller and gradually increasing the load to a maximum of 1,2 kN and then stopping at this load for about 20 seconds. Subsequently, the controller knob was turned back to the zero position and then increased to 1,2 kN in the negative direction, stopping at –1,2 kN for the tensile force. Finally, the knob was turned back to zero. This completed one sinusoidal cycle for Load division 1. The actuator controller data was collected using MATLAB. The raw data is presented in Appendix 5. The force vs time curve for Load division 1 was also generated to obtain the complete sinusoidal cycle for this load division, as shown in Figure 3.13.
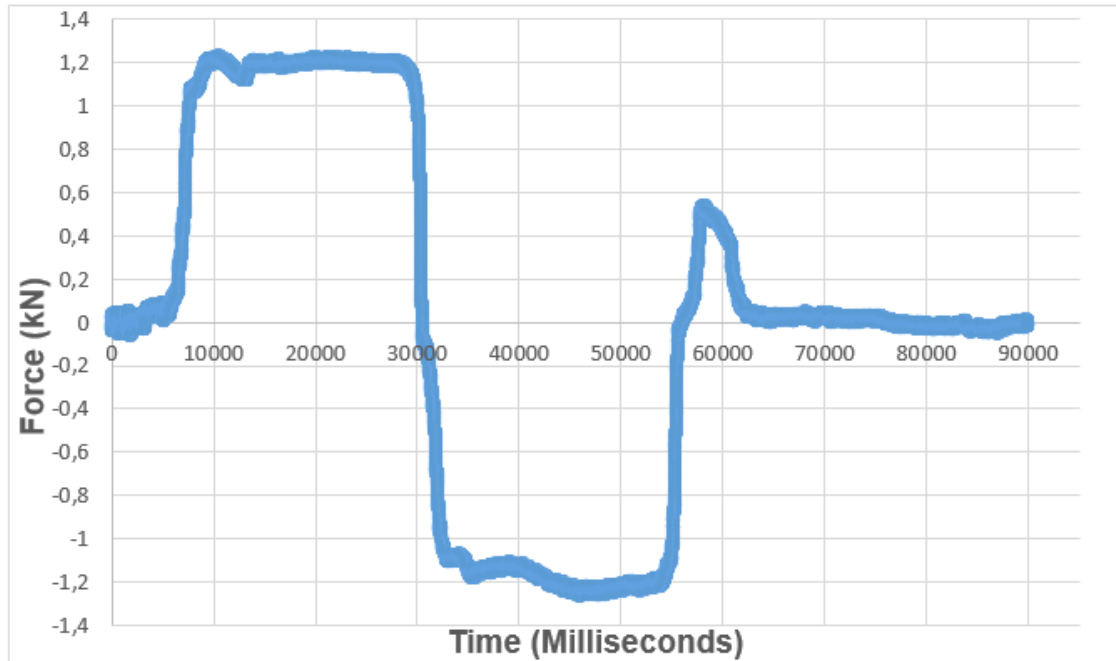
Figure 3.13: Force vs time curve for Load division 1 of the X-direction testing

The load data points from 15 000 to 25 000 milliseconds in Figure 3.13 were collected, and the mean value of these data points was calculated to provide the actual static load applied. This load was found to be 1,206 kN. This verification had to be done because the actuator controller did not use a digital system where accurate values could be set, only a knob that had to be set manually. This procedure was repeated for all five load divisions, and the results are tabulated in Table 3.8.

Table 3.8: Planned versus actual load values of the X-direction static tests for the DMLS Ti6Al4V(ELI) prototype nose wheel fork

Load divisions	Planned load (kN)	Actual load (kN)
1	1,200	1,206
2	2,400	2,424
3	3,600	3,582
4	4,800	4,892
5	6,000	6,120

The procedure followed in the applied load results for Load division 1 (static force of 1.2 kN) was repeated for the strain results of Load division 1 for the X-load case to record and analyse all the strain results throughout the experiment.

3.4.3.2 Preparation of data for X-direction of loading – strain gauges

The data acquisition system allowed all eight strain gauges to collect data simultaneously for each load case. Similar to the actuator controller, Load division 1 is used here as an example to demonstrate the procedure followed to prepare data for analyzing the strain gauge values measured on the DMLS Ti6Al4V(ELI) nose wheel fork.

The Quantum X MX840 strain data collection system was activated at the same time as the controller knob to allow simultaneous data capturing. The raw data from all the strain gauges were also collected and plotted, and the mean value was calculated at the peak point corresponding to the load versus time curve in Figure 3.13. These results are provided in Chapter 4.

The eight strain gauges had a unique nomenclature for each strain gauge. This nomenclature was used to identify the position (channel) where the strain gauge was connected on Quantum X, the strain gauge number, as well as the position of the strain gauge on the nose wheel fork, as shown in Figure 3.8. The first strain gauge is used as an example to explain this nomenclature further:

CH 1_SG_1A_P1: *CH 1* = Channel number 1 in Quantum X, *SG_1A* = Strain Gauge number 1A, and P1 = Position 1 in Figure 3.8.

Table 3.9 gives the details of all eight strain gauges and their positions.

Table 3.9: Quantum X channels and their connected strain gauges

Position for connection on Quantum X	Abbreviation	Strain gauge name
Channel 1	CH 1	CH 1_SG_1A_P1
Channel 2	CH 2	CH 2_SG_1B_P1
Channel 3	CH 3	CH 3_SG_1C_P1
Channel 4	CH 4	CH 4_SG_2A_P2
Channel 5	CH 5	CH 5_SG_2B_P2
Channel 6	CH 6	CH 6_SG_2C_P2
Channel 7	CH 7	CH 7_SG_3_P3
Channel 8	CH 8	CH 8_SG_4_P4

3.5 Summary

The methodology used in this chapter included non-destructive analytical techniques, such as CT scanning and SEM, on the test specimens for validation of the DMLS process using Ti6Al4V(ELI) powder, as well as the characterization of the surface roughness of the as-built Ti6Al4V(ELI) specimens. Tensile and fatigue testing was employed to determine the mechanical properties of the as-built DMLS Ti6Al4V(ELI) parts, followed by the fractography and metallographic analysis of the fractured fatigue test specimens. The DMLS Ti6Al4V(ELI) scaled-down prototype nose wheel fork was tested under static performance conditions using specialized equipment that could simulate the operational conditions of the nose wheel fork. This static data contributed to the comprehensive doctoral study aimed at contributing to the eventual qualification of the LPBF Ti6Al4V(ELI) nose wheel fork.

CHAPTER 4: RESULTS AND DISCUSSION

4.1 Introduction

This chapter includes the results of the CT scanning, the tensile and fatigue tests of the test specimens, as well as the fractography and microstructural analysis of the fractured DMLS Ti6Al4V(ELI) specimens. Finally, the static performance of the DMLS Ti6Al4V(ELI) scaled-down nose wheel fork is presented and discussed.

4.2 Micro-CT scanning

The density results of the DMLS Ti6Al4V(ELI) specimens submitted to two-stage heat treatment are presented in this section. In Table 4.1, the percentage porosity as determined through micro-CT analysis of the specimens built along the X-, Y- and Z-direction are tabulated.

Table 4.1: Micro-CT porosity results of DMLS Ti6Al4V(ELI) test specimens

Specimen Designation	Porosity (%)
X1	0.0029
Y1	0.0033
Z1	0.0011

The level of porosity shown in Table 4.1 was found to be below 0.01%. This was an extremely low level of porosity and confirmed the consistency of the EOSINT M280 machine employed to build the test specimens compared to porosity levels found in other studies [69][70]. High porosity levels could negatively impact the fatigue performance of the DMLS-built parts because they act as stress raisers, which could initiate cracks [69]. However, from the literature, it was also clear that the fatigue behaviour of DMLS-built parts cannot only be related to the level of porosity but also the location, size and geometry of pores [69]. It has been reported that a very specific type of layered defect can be formed in DMLS parts due to incomplete melting in specific layers. These defects may be present in a part with as little as 0.005% porosity and

can still be problematic if localized in a thin-walled section [71]. These pore locations are critical for fatigue performance because they determine the stress concentration factor during loading [72][73]. However, no large pores or clusters of pores were localized in sections of any of the test specimens in this study. This confirmed the quality of the DMLS build process.

4.3 Tensile test results

The tensile test results for the DMLS Ti6Al4V(ELI) specimens built in the X-, Y- and Z-orientations are given in Table 4.2.

Table 4.2: Tensile test results for the X-, Y-, and Z-orientation DMLS Ti6Al4V(ELI) test specimens

Specimen Designation	Tensile Stress at Yield (Offset 0.2%) (MPa)	Ultimate Tensile Stress (MPa)	Modulus of Elasticity (GPa)	Percentage Elongation (%)
ASTM F 3001 – 14				
-	795	860	-	10
This study				
X1	860.42	948.13	116.3	16.50
X2	852.44	939.65	113.9	15.50
X3	853.73	941.53	115.0	15.05
Mean	**855.73**	**943.10**	**115.1**	**15.68**
Standard deviation	**4.285**	**4.450**	**1.162**	**0.472**
Y1	863.94	947.64	118.1	13.25
Y2	860.75	943.50	120.8	14.70
Y3	856.71	941.14	114.6	15.05
Mean	**856.71**	**941.14**	**114.69**	**14.33**
Standard deviation	**3.625**	**3.289**	**3.089**	**0.954**
Z1	774.78	888.52	110.0	15.75
Z2	780.48	894.81	109.5	15.60
Z3	781.33	891.61	108.5	16.15
Mean	**778.86**	**891.65**	**109.3**	**15.83**
Standard deviation	**3.562**	**3.146**	**0.796**	**0.284**

The specimens in the X- and Y-orientations exhibited similar tensile properties with the mean tensile stress at yield, showing no significant difference, ranging from 855.73 ± 4.285 MPa on the X-specimens to 856.71 ± 3.625 MPa on the Y-specimens. The ultimate tensile stress and the modulus of elasticity for both X- and Y- specimens also had similar values. However, there was a significant difference in tensile properties when comparing the aforementioned mean values of the X- and Y-orientation specimens with that of the Z-orientation specimens. The mean tensile stress at yield for the Z-specimens was found to be 778.86 ± 3.562 MPa, with the ultimate tensile stress and modulus of elasticity being 891.65 ± 3.146 MPa and 109.3 ± 0.796 GPa, respectively. This is common for LPBF-built parts due to the layer-by-layer building, showing a level of anisotropy with respect to the three orthogonal building directions [3][74]. However, when comparing the ultimate tensile stress, yield stress and elongation values for the X-, Y-, and Z-orientation specimens, it is clear that the tensile properties of the X- and Y-orientation specimens in Table 4.2 meet the minimum requirements for the specified tensile properties in ASTM F3001 – 14 for AM Ti6Al4V(ELI) produced with PBF [68].

The ultimate tensile stress and elongation values of the Z-orientation specimens also exceeded the minimum requirements set in the ASTM F3001 – 14 standard, while only the yield stress was 2.03% lower, compared to the set minimum value of 795 MPa in the ASTM F3001 – 14 standard. This observation confirmed the anisotropic nature of parts built in different orientations in the DMLS machine. This has been attributed to the DMLS microstructure of the alloy that displayed the direction of growth of epitaxial β grains to be parallel to the build direction [74]. However, it was expected that the high-temperature annealing heat treatment applied to these specimens should have resulted in a more homogenous microstructure with corresponding alleviation of the anisotropy of the mechanical properties.

4.4 Fatigue test results

The HCF test results of the DMLS Ti6Al4V(ELI) specimens are given in Table 4.3 for the Z-specimens, Table 4.4 for the X-specimens and Table 4.5 for the Y-specimens.

Table 4.3: Fatigue test results for Z-orientation DMLS Ti6Al4V(ELI) test specimens

Specimen designation	Maximum stress (MPa)	Number of cycles to fatigue failure (N_f)
Z8	225	5 000 000
Z9	250	730 494
Z7	270	370 439
Z10	300	483 996
Z6	360	122 595
Z5	418	61 584
Z4	450	50 142

Table 4.4: Fatigue test results for X-orientation DMLS Ti6Al4V(ELI) test specimens

Specimen designation	Maximum stress (MPa)	Number of cycles to fatigue failure (N_f)
X8	190	5 000 000
X10	200	1 153 581
X7	210	893 273
X6	230	513 876
X9	270	346 930
X5	300	218 190
X4	360	147 027

Table 4.5: Fatigue test results for Y-orientation DMLS Ti6Al4V(ELI) test specimens

Specimen designation	Maximum stress (MPa)	Number of cycles to fatigue failure (N_f)
Y7	190	5 000 000
Y10	200	1 002 143
Y6	230	598 800
Y8	250	538 903
Y9	270	434 787
Y5	300	304 007
Y4	360	132 859

The Z7-specimen failed at 270 MPa with 370 439 cycles to failure, while Z10 failed at 300 MPa with 483 996 cycles to failure. Both the Z7 and Z10 specimens failed outside the gauge length and can thus be considered outliers.

Figure 4.1. presents the data in Tables 4.3 to 4.5 as semi-log S-N diagrams of the specimens built in the three orthogonal directions.
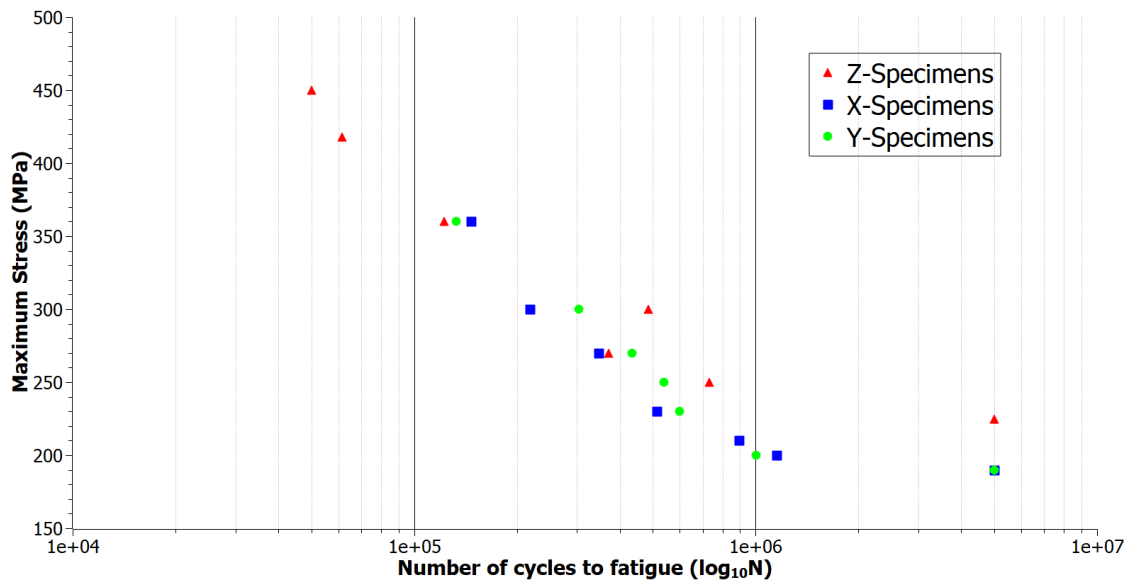
Figure 4.1: Semi–log S-N diagrams for the Ti6Al4V(ELI) test specimens

From Figure 4.1, it is clear that the fatigue performance of the X- and Y-orientation specimens did not differ significantly. However, the fatigue strength of the X- and Y-orientation specimens was 16% less than that of the Z-orientation specimens. The endurance limit of five million cycles was achieved at 225 MPa for the Z-orientation specimens and 190 MPa for both the X- and Y-orientation specimens. This difference can be ascribed to the surface irregularities on the X- and Y-orientation specimens where the support structures needed for these build orientations were removed, especially the pin support structures, as shown in Figure 4.2.
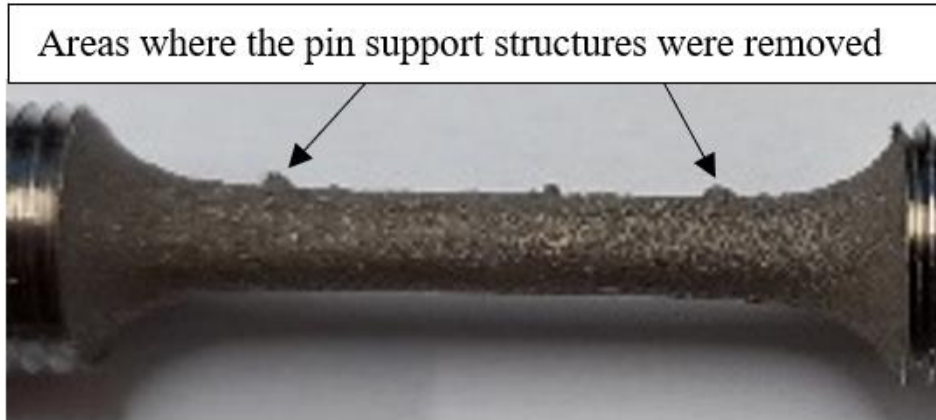
Figure 4.2: The gauge length of a typical LPBF Ti6Al4V(ELI) test specimen built in the X-orientation showing the surface irregularities due to support structures.

The surface irregularities shown in Figure 4.2 acted as areas of stress concentration, which could lead to crack initiation, resulting in a lower fatigue endurance limit for the X- and Y- orientation specimens as compared to the Z-orientation specimens. In the study of Malefane et al. [51], DMLS Ti6Al4V(ELI) test specimens were also built in three orientations (X, Y and Z). All the specimens were heat-treated under the same heat treatment conditions as in the current study but were machined to fully comply with the geometry specified in ASTM E8. In their study, Malefane et al. [51] found that the endurance limit of five million cycles could be reached at maximum stress of 450 MPa for all three building orientations. However, in the current study, the specimens X8 and Y7 could reach an endurance limit of five million cycles at maximum stress of only 190 MPa, while the Z8 specimen reached the limit at a maximum stress of 225 MPa. This implies that the surface irregularities had a strong negative effect on the fatigue properties of the DMLS Ti6Al4V(ELI) specimens that were not machined. Figure 4.3 illustrates the difference in the surface finish of the X- and Z-orientation specimens that endured the maximum stress until five million cycles without failing.
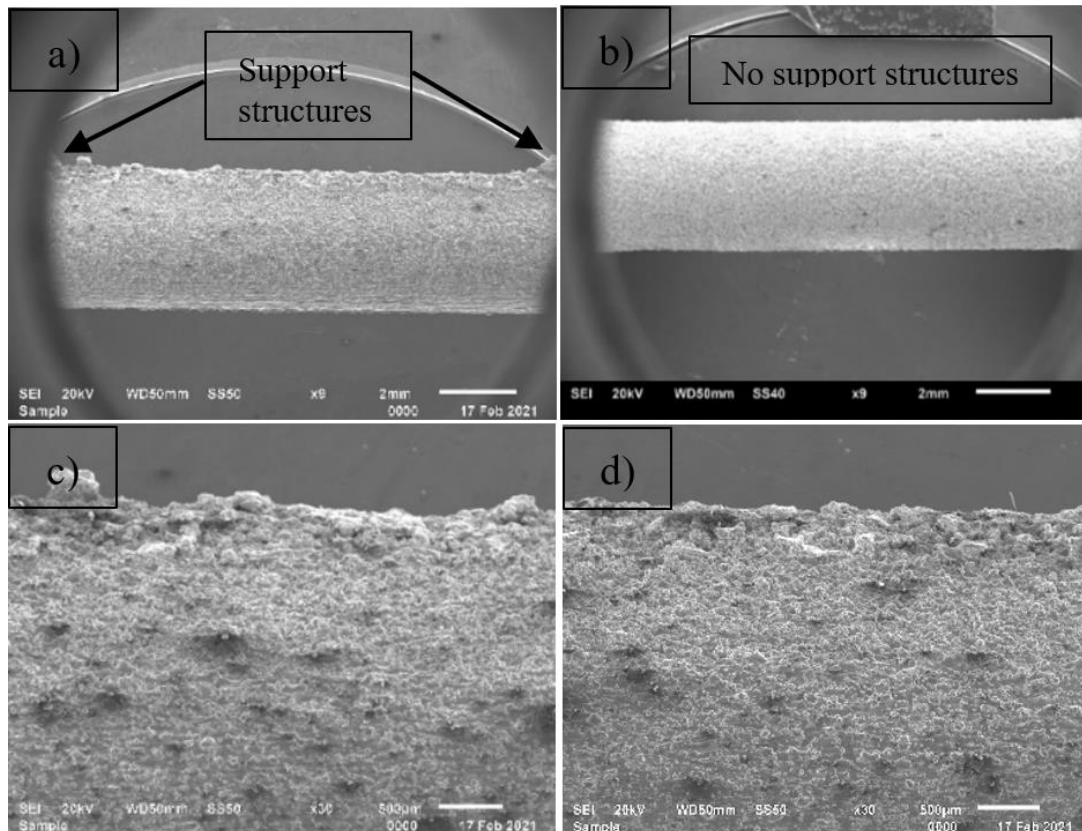
Figure 4.3: SEM SEI of the surface topography of Ti6Al4V(ELI) specimen gauge length areas: a) specimen X8, b) specimen Z8, c) higher magnification of specimen X8, d) higher magnification of specimen Z8

Figures 4.3 (a) and 4.3 (b) show that the specimen built in the X-orientation (which was similar to specimens built in the Y-orientation) appeared to have rougher surfaces on the gauge length area when compared to the specimen built in the Z-orientation. This was expected because the Z-orientation specimens had no support structures on the gauge length, as described in section 3.2.1. This confirmed that the adhesion points of the support structures locally increased the surface roughness of the DMLS parts and resulted in the X- and Y-orientation specimens reaching the endurance limit at lower stress (190 MPa) than the Z-specimens (at 225 MPa).

4.5 Fractography of DMLS Ti6Al4V(ELI) fatigue test specimens

The fracture surfaces of the fractured fatigue test specimens revealed the three stages of fatigue fracture (crack initiation, propagation and final fracture) as

observed in other studies [51][57][75]. Figure 4.4 shows the fracture surface of the Z4 specimen that failed at 50 142 cycles at the maximum stress of 450 MPa.
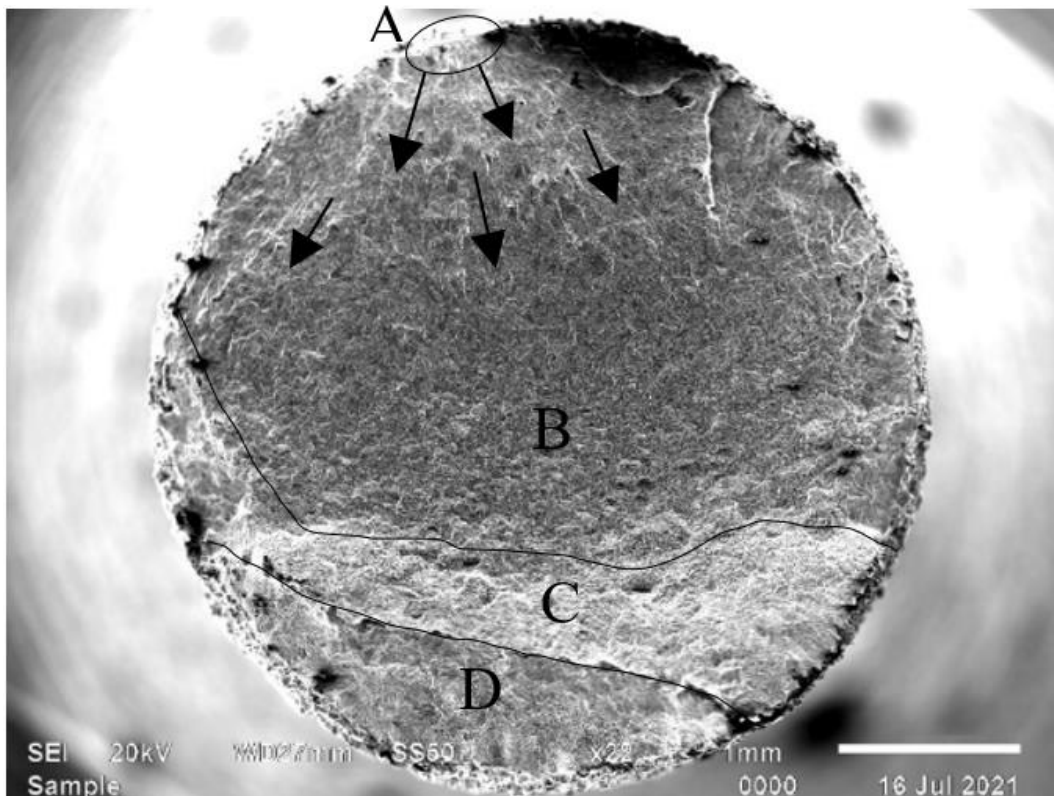
Figure 4.4: SEM SEI of fracture surface of the Z4 specimen: A: crack initiation area B: stable crack propagation area C: fast crack propagation area D: final fracture area

The crack initiated in encircled area A in Figure 4.4 and propagated slowly across the section of the specimen as indicated by the arrows in area B. The crack further propagated to the faster crack propagation region (Area C), and the final fracture occurred in area D. A magnified image of the crack initiation area in Figure 4.4 is presented in Figure 4.5, where the two initiation points due to an inclusion and a surface ridge on the outer surface of the specimen, are indicated. Partially melted powder particles on the surface of the specimen are also visible. These surface defects promote crack initiation [70]. Chastand et al. [70] identified surface and sub-surface defects as the most critical types of defects influencing the fatigue properties of SLM Ti6Al4V. This was also confirmed by Dallago et al. [76].
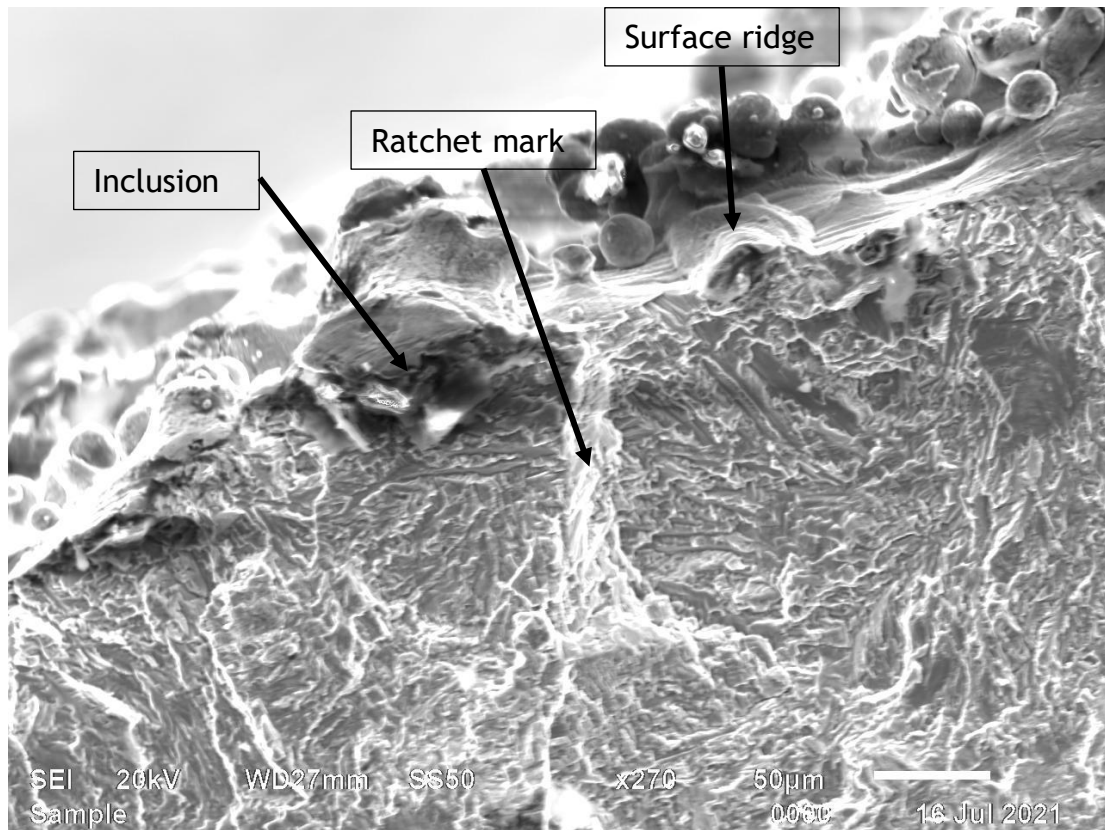
Figure 4.5: SEM SEI at higher magnification of area A in Figure 4.4, where crack initiation occurred

Figure 4.6, a higher magnification of area B in Figure 4.4, shows the characteristics of slow crack propagation with small areas of tear ridges. The tear ridges are clearly visible on the areas closer to the initiation point at area A in Figure 4.4, then start fading towards the middle of area B in Figure 4.4. There were also micro-cracks on area B in Figure 4.4, indicated by arrows in Figure 4.6.
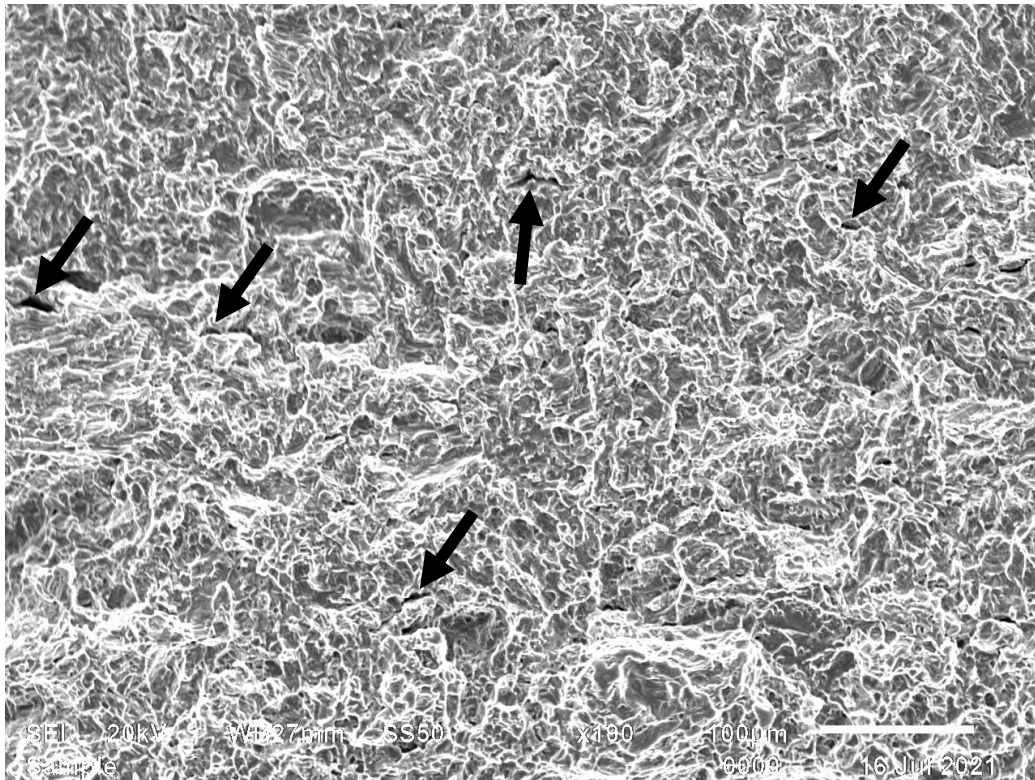
Figure 4.6: SEM SEI at higher magnification of area B in Figure 4.4, where slow crack propagation occurred with micro-cracks indicated by the arrows

In Figure 4.7, the pores formed in the faster crack propagation zone are shown. The higher magnification of the final fracture area in Figure 4.8 shows a dimple fracture, indicating that the material was ductile [77].
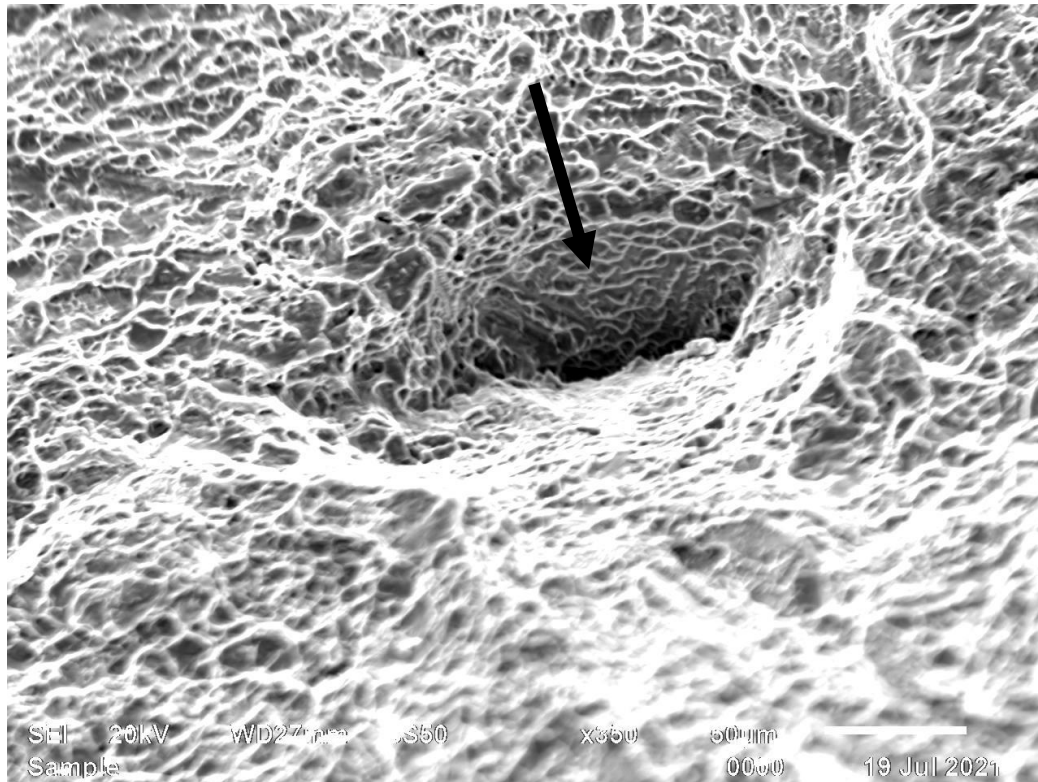
Figure 4.7: SEM SEI at higher magnification of area C in Figure 4.4, where faster crack propagation occurred with a pore indicated by the arrow
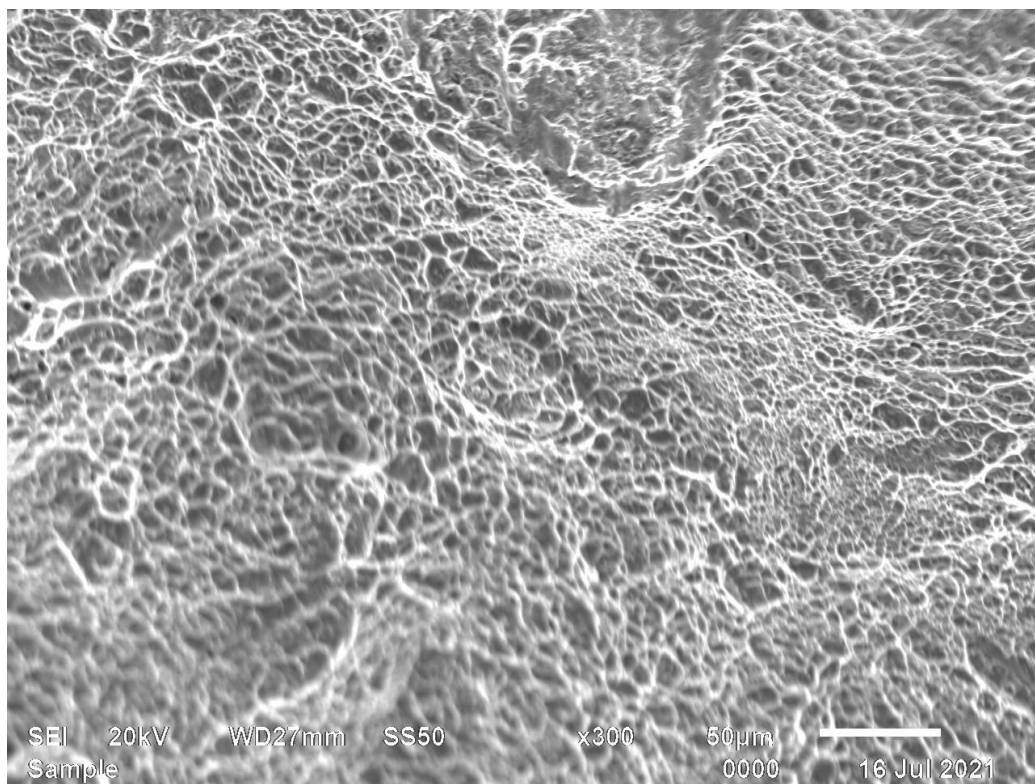
Figure 4.8: SEM SEI at higher magnification of area D in Figure 4 showing the final fracture surface

The fracture surfaces of HCF DMLS TI6Al4V test specimens built in the X- and Y-directions were also analyzed. These test specimens showed similar fracture surface features. Figure 4.9 shows the fracture surface of the Y10 specimen, which failed after 1 002 143 cycles at the maximum stress of 200 MPa.
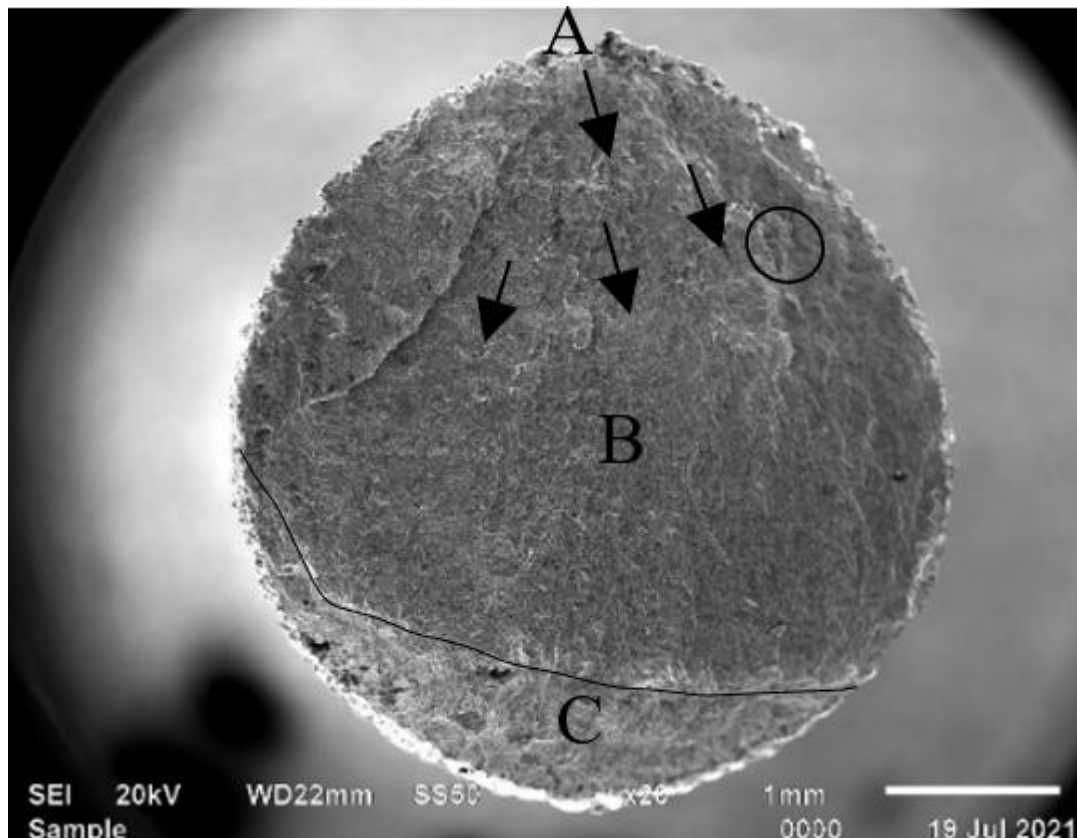
Figure 4.9: SEM SEI of the fracture surface of the Y10 specimen: A: crack initiation area B: crack propagation area , with the encircled area showing the flat surfaes C: final fracture area

The Y10 specimen fracture surface in Figure 4.9 also revealed the three stages of fatigue fracture, namely, crack initiation at A, propagation at B and final fracture at C. The crack initiation was identified at the surface where the support structure was removed, shown as area A in Figure 4.9 (The higher magnification of this area is shown in Figure 4.10).
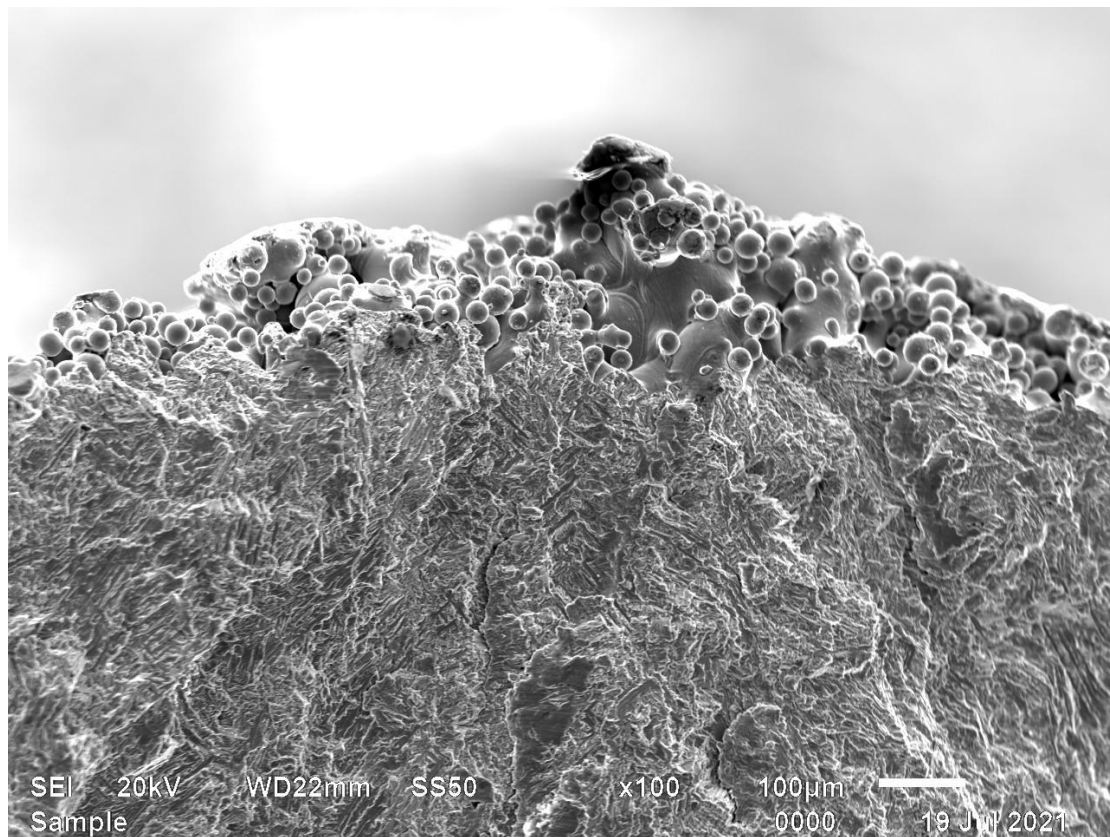
Figure 4.10: SEM SEI at higher magnification of area A in Figure 4.9 where the crack initiation, with powder particles indicating lack of fusion

From Figure 4.10, it was confirmed that the support structures created areas of stress concentration. Unmelted powder particles are also visible in the sub-surface region of this specimen. The crack propagated almost symmetrically down towards the centre of the specimen, as indicated by the arrows in area B in Figure 4.9. A higher magnification of this area is presented in Figure 4.11.
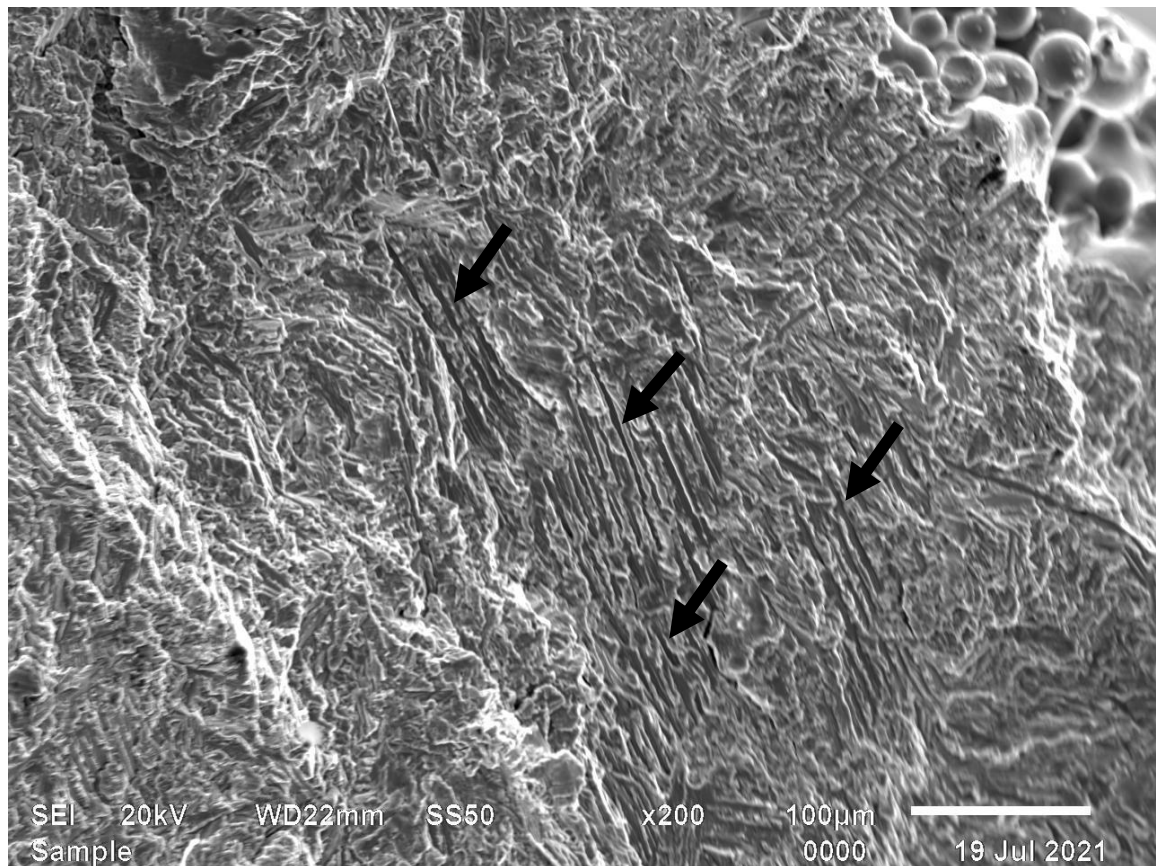
Figure 4.11: SEM SEI at higher magnification of area B in Figure 4.9 showing fatigue striations, indicated by the arrows, in the crack propagation area

Fatigue striations were observed in the crack propagation area, as indicated by the arrows in Figure 4.11. Similar fatigue striations were also found in the study of Gong et al. [78] on their heat-treated TI6Al4V(ELI) parts. Flat surfaces were observed on the encircled area in Figure 4.9, of which a higher magnification is presented in Figure 4.12. These localised flat surfaces could have resulted from intergranular fracture instead of transgranular fracture.
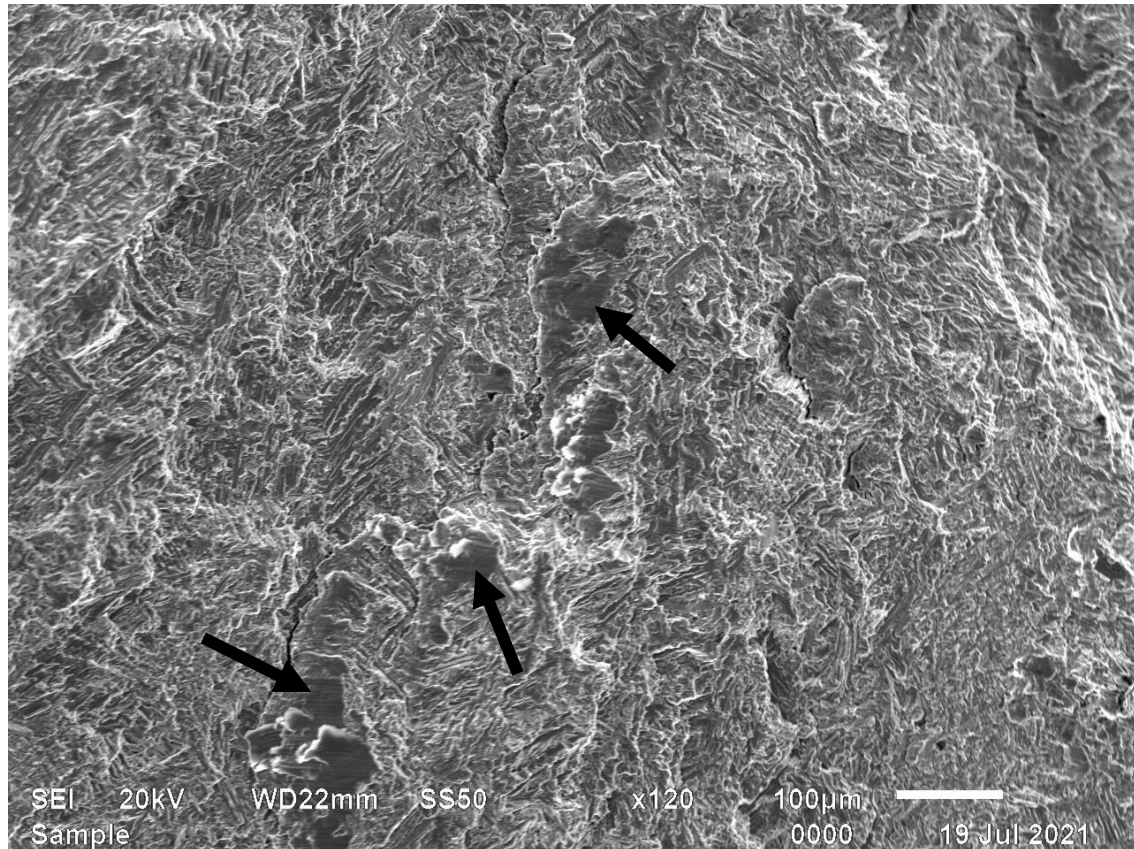
Figure 4.12: SEM SEI at higher magnification of the encircled area in Figure 4.9 showing localized flat surface areas

Hartunian et al. [79] also observed these flat areas in their study on the effect of build orientation on the microstructure and mechanical properties of SLM Ti6Al4V alloy and associated them with a mix of brittle and ductile fracture features.

The final fracture of the Y10 specimen is shown in Figure 4.13, with dimples similar to that of Z4 in Figure 4.8, confirming a ductile fracture type.
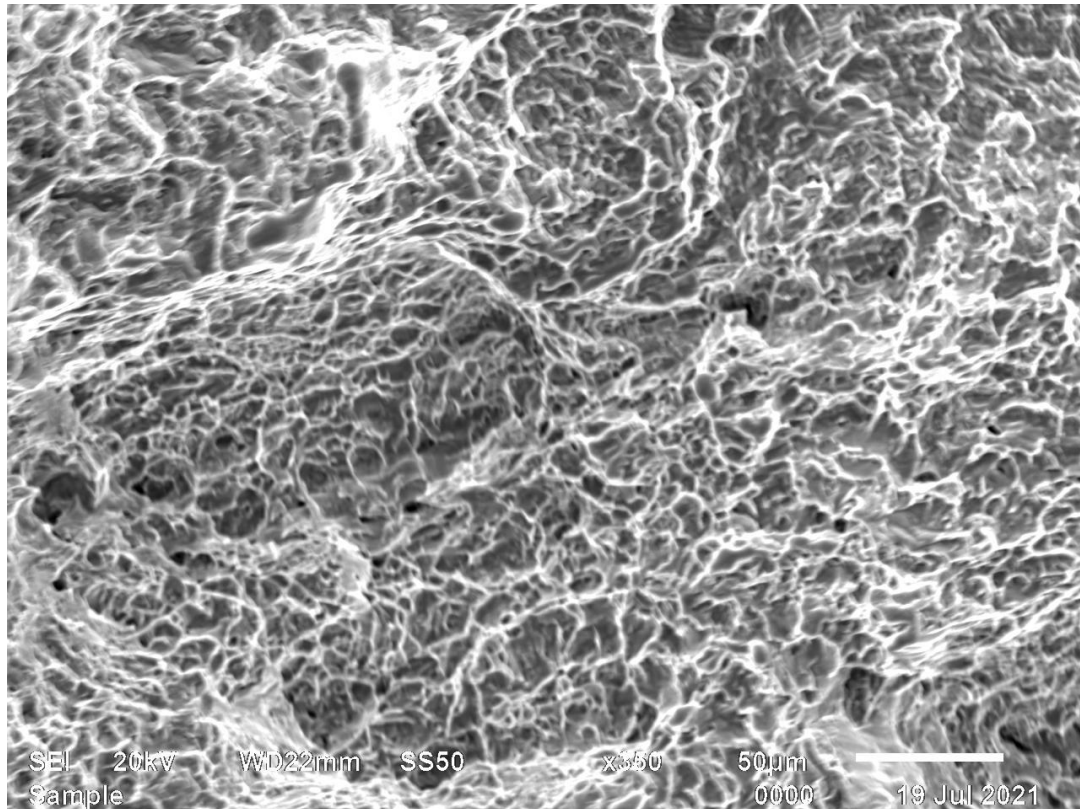
Figure 4.13: SEM SEI at higher magnification of area C in Figure 4.9 showing the final fracture surface

The crack initiation points of the Z4 specimen in Figure 4.4 and the Y10 specimen in Figure 4.9 differed. In the Z4 specimen, crack initiation was due to inclusions in the sub-surface region that resulted in shorter fatigue life of the specimen. In the Y10 specimen, the crack initiation was due to a surface irregularity where the significant partially melted powder particles could be observed in the area where the support structures were removed. Chandran [80] found that inclusions can result in a much shorter fatigue life located close to the sample surface in comparison to inclusions in the bulk of a part. Internal defects have been previously reported as the cause of failure in high-cycle fatigue [3][16][76]. Yan et al. [3] suggested that the HCF properties of their HIPed samples indicated that minimized porosity could significantly improve the fatigue strength of the material. However, in the current study, internal porosity was minimal; therefore, the poorer HCF performance of the as-built test specimens is attributed to the inherent surface roughness. This was also observed in the study of Wycisk et al. [57], where lower cycles to fatigue were achieved due to the inherent surface roughness for material in the as-built condition.

4.6 Microstructure analysis of DMLS Ti6Al4V(ELI) test specimens

Optical micrographs of cross sections of the Ti6Al4V(ELI) test specimens built as described in section 3.2 are shown in Figures 4.14 to 4.16. These test specimens were submitted to stress relieving and high-temperature annealing to relieve the residual stress and decompose the acicular α' martensitic microstructure into the $\alpha+\beta$ microstructure, respectively. Figures 4.14, 4.15 and 4.16 show the micrographs of the X-, Y- and Z-orientation specimens, respectively. These micrographs show the cross sections of the specimens in the following planes: Y-Z plane for the X-orientation specimen, X-Z plane for the Y-orientation specimen and X-Y plane for the Z-orientation specimen. The beta phase appears dark, and the alpha phase appears light in all three micrographs.
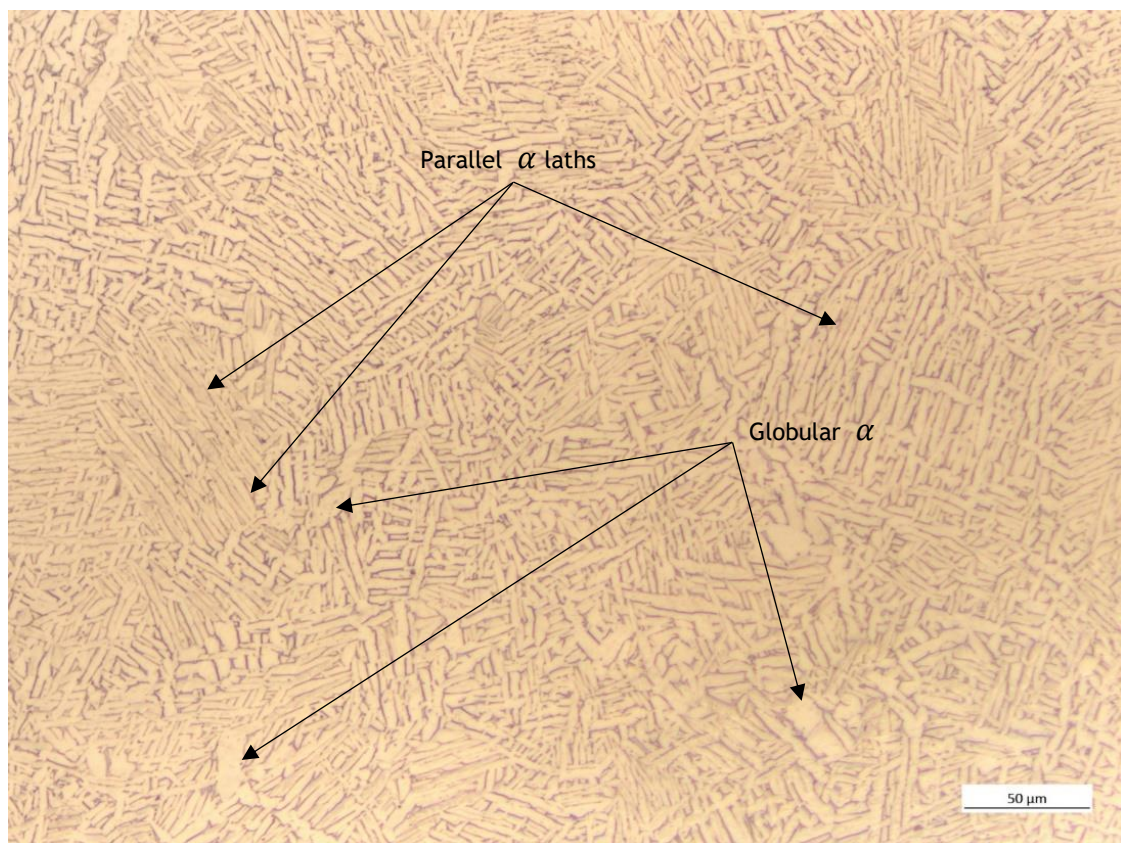
Figure 4.14: Optical micrograph of the cross section of a DMLS Ti6Al4V(ELI) specimen built along the X-orientation, stress relieved for three hours, followed by HTA at 950 °C for two hours and furnace cooled
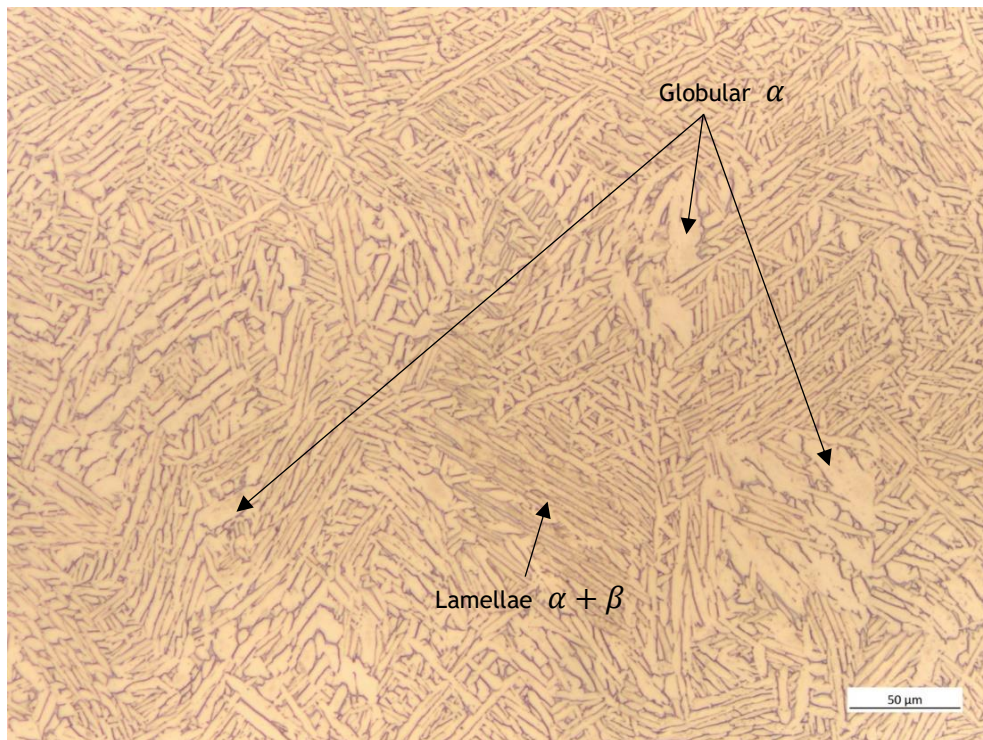
Figure 4.15: Optical micrograph of the cross section of a DMLS Ti6Al4V(ELI) specimen built along the Y-orientation, stress relieved for three hours, followed by HTA at 950 °C for two hours and furnace cooled
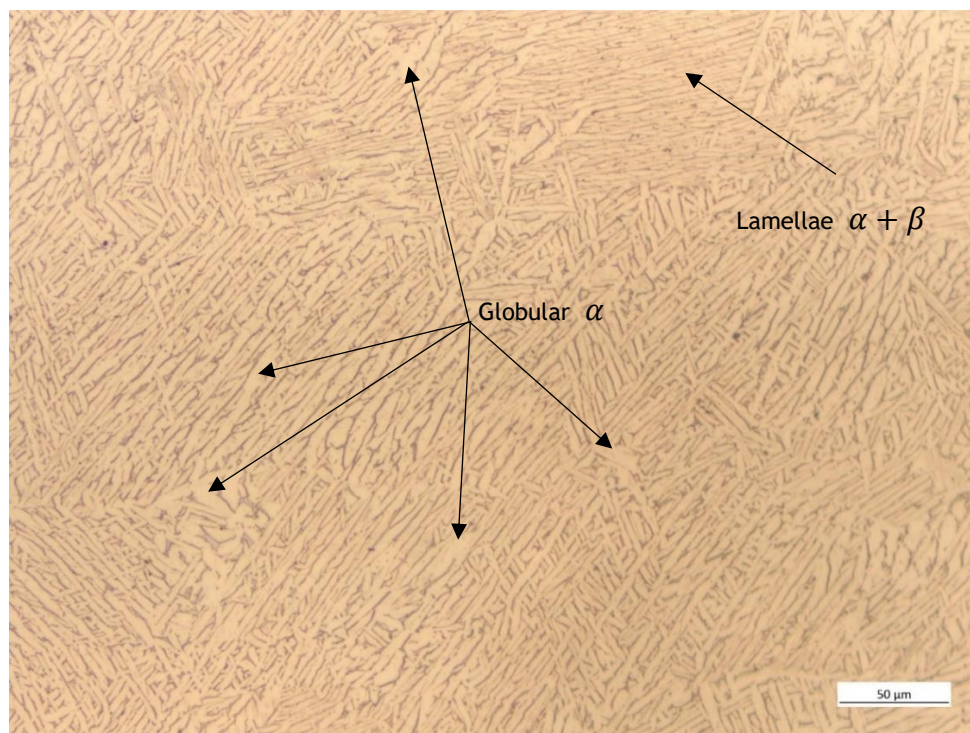
Figure 4.16: Optical micrograph of the cross section of a DMLS Ti6Al4V(ELI) specimen built along the Z-orientation, stress relieved for three hours, followed by HTA at 950 °C for two hours and furnace cooled

The micrographs of the X-, Y-, and Z-orientation specimens revealed a decomposition of the acicular α' microstructure into a lamellar α+β microstructure. From a fatigue point of view, this transformation of α' microstructure to α+β microstructure contributes to a larger elongation and improved strain hardening [3]. This confirmed that the two-hour soaking time at 950 °C improved mechanical properties, particularly properties related to HCF [27][81]. Furthermore, these micrographs show globular α as indicated by the arrows in Figures 4.14, 4.15 and 4.16. Globular α contributes to the ductility of the material as a characteristic of an equiaxed microstructure [43]. However, in this study, the microstructures were not fully equiaxed but bimodal. Yadroitsev et al. [82] reported that a bimodal microstructure was achieved with lamellar grains within the prior columnar β grains and clusters of equiaxed globular α after the high-temperature anneal at 950 °C for two hours, followed by furnace cooling. Therefore, it is evident that the refinement of the microstructures of DMLS Ti6Al4V(ELI) parts can be tailored through heat treatments and result in improved ductility of Ti6Al4V(ELI) components, consequently improving the fatigue resistance of this alloy. This potential to tailor the microstructure of DMLS Ti6Al4V(ELI) contributed to a more comprehensive doctoral study, which could lead to the eventual qualification of the DMLS process for production of structural aerospace components.

4.7   Static performance test results of the prototype scaled-down nose wheel fork

The results from all five load divisions for the X-, Y- and Z-load cases described in section 3.4.3 are presented in this section.

4.7.1 Static performance test results of the scaled-down nose wheel fork in the X-direction of loading

The strain vs time sinusoidal curves for Load division 1 of the X-load case corresponding to the force curve in Figure 3.9 in section 3.4.3 are presented in Figure 4.17.
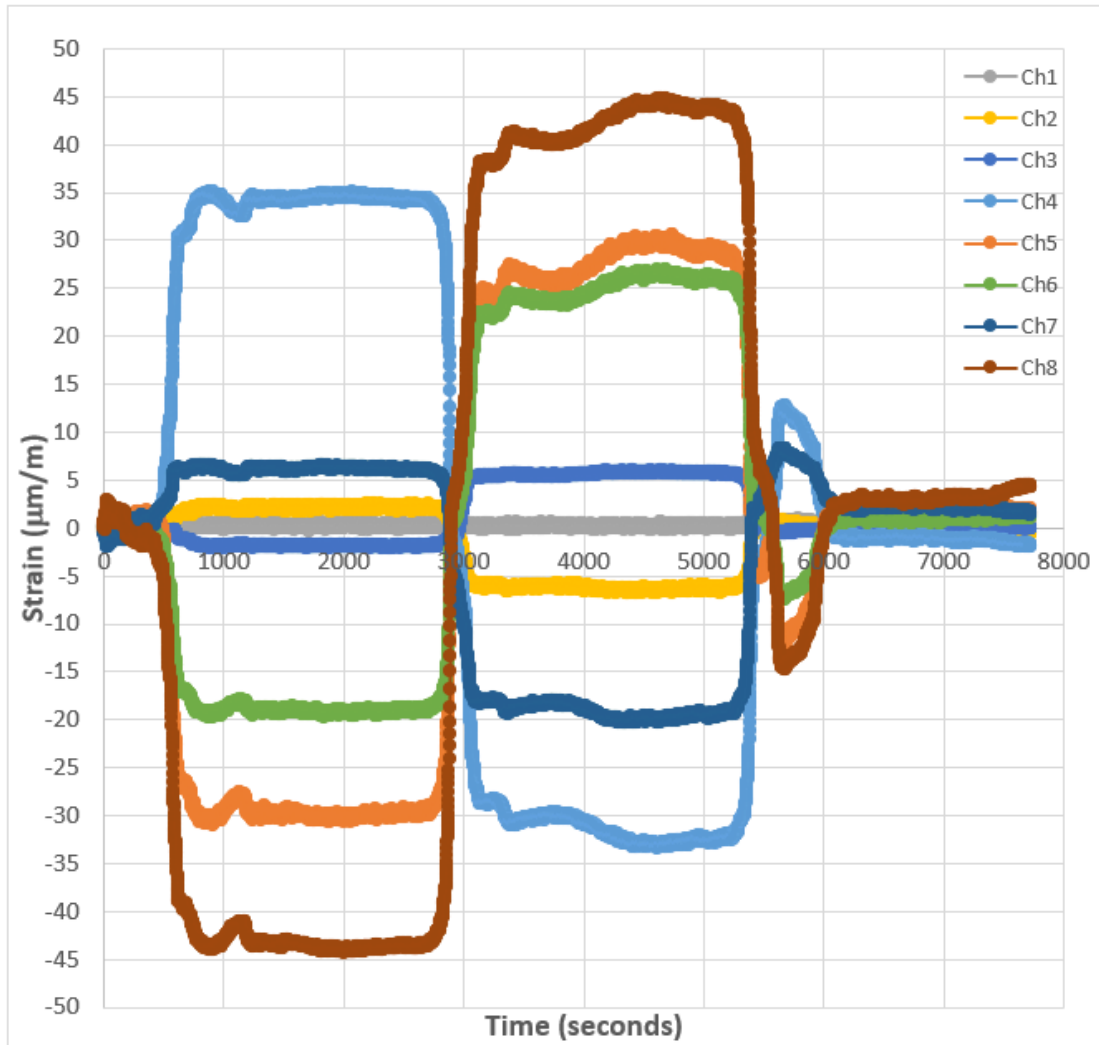
Figure 4.17: Strain vs time curves for load division 1 of X-load case

As described in section 3.4.3, the data points in Figure 4.17 were taken from the peak points (1 500 to 2 000 milliseconds) of all strain gauges from each load division (1 to 5), and the mean values were calculated. See Appendix 6 for the full data set. The graphical representations of this data are shown in Figure 4.18.
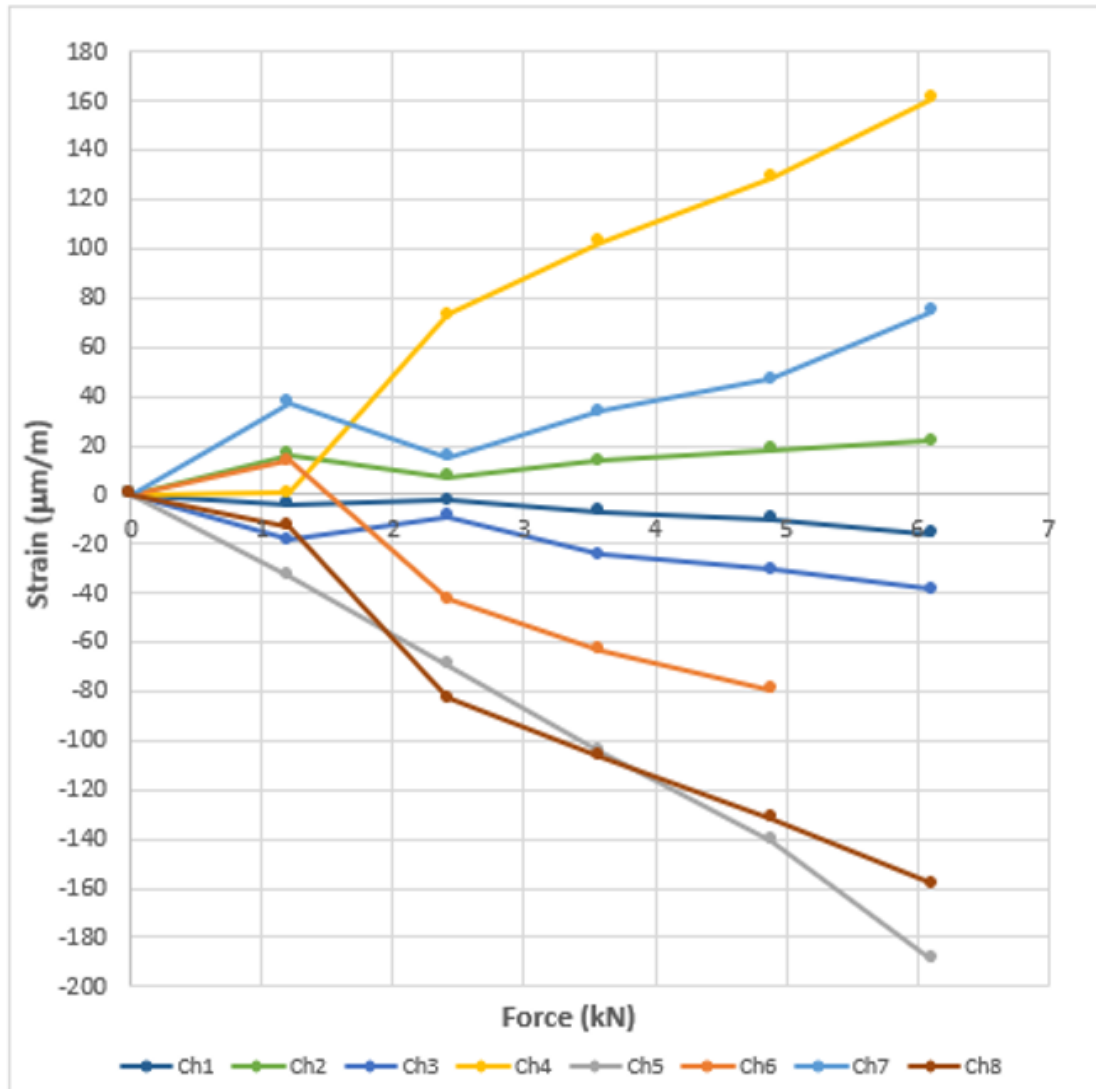
Figure 4.18: Strain vs force curves for the X-load case

A clear trend of strain increasing with force can be seen in Figure 4.18, without the failure of the prototype scaled-down nose wheel fork. The fact that the nose wheel fork prototype did not fail, even at maximum load, confirmed that the DMLS process followed resulted in a built part with good integrity for applications.

The strain versus force results for the static tests in the Y- and Z-loading directions are presented in the following sections. The complete raw data is given in Appendices 5 and 6.

4.7.2 Static performance test results of the scaled-down nose wheel fork in the Y-direction of loading

The actual experimental force values for the Y-load case are tabulated in comparison with the planned forces in Table 4.6, followed by the strain versus force curves in Figure 4.19.

Table 4.6: Planned versus actual load values of the Y-direction static test for the DMLS Ti6Al4V(ELI) prototype nose wheel fork

Load divisions	Planned load (kN)	Actual load (kN)
1	0,800	0,820
2	1,600	1,580
3	2,400	2,420
4	3,200	3,100
5	4,000	4,100
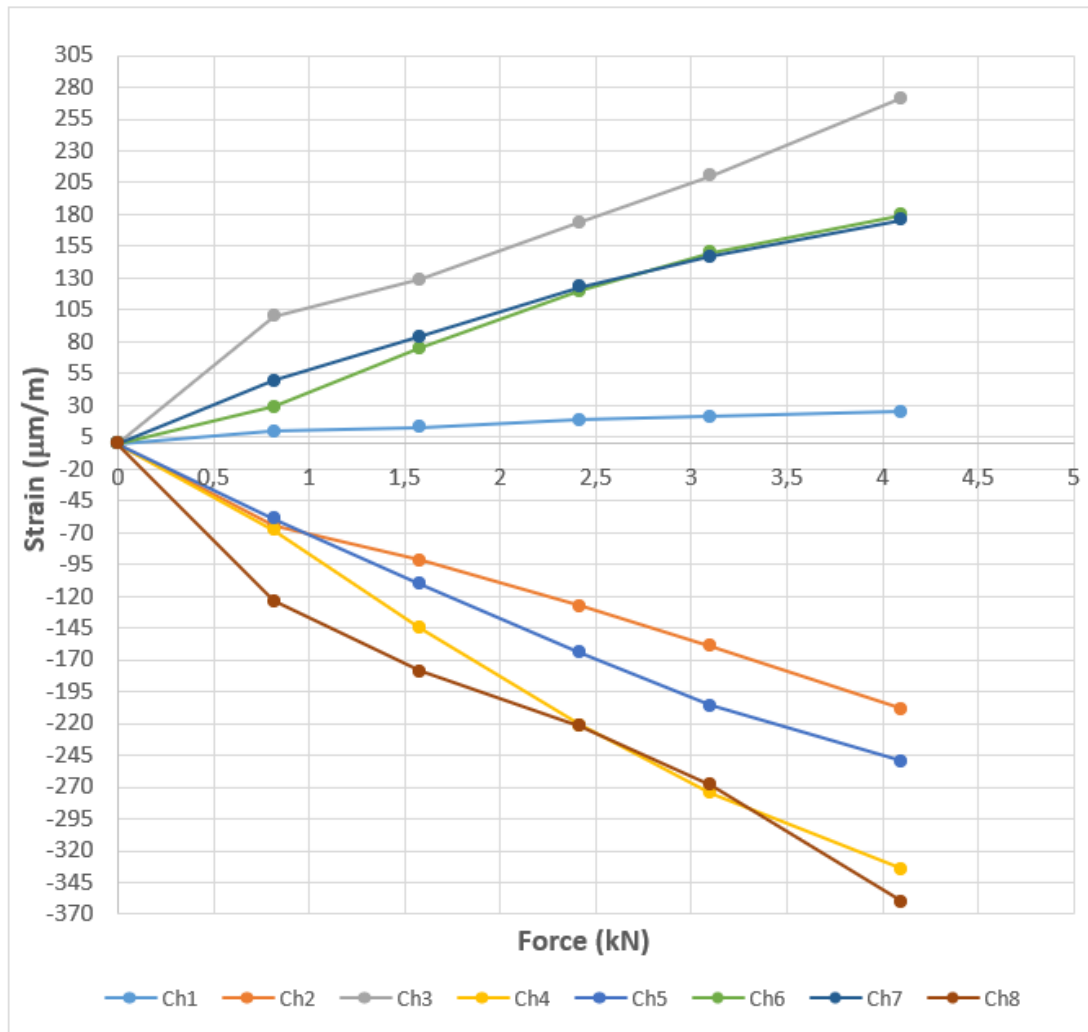
Figure 4.19: Strain vs force curve for Y-load case

4.7.3 Static performance test results of the scaled-down nose wheel fork in the Z-direction of loading

The planned values of force versus the actual experimental values are tabulated in Table 4.7 for this direction of loading. The resulting strain versus force curves are shown in Figure 4.20.

Table 4.7: Planned versus actual load values of the Z-direction static test for the DMLS Ti6Al4V(ELI) prototype nose wheel fork

Load divisions	Planned load (kN)	Actual load (kN)
1	1,700	1,720
2	3,400	3,630
3	5,100	5,140
4	6,800	6,860
5	8,500	8,480
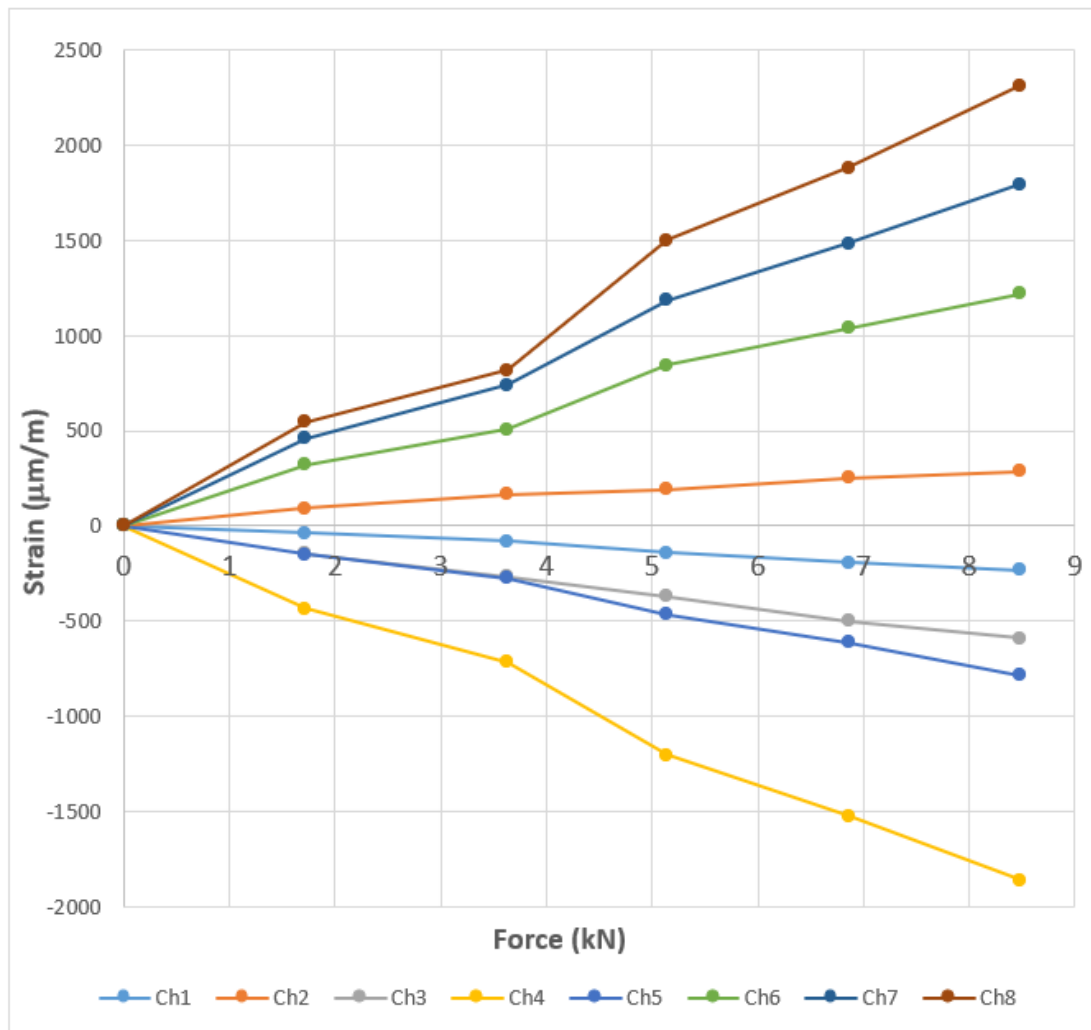
Figure 4.20: Strain vs force curve for Z-load case

The results found in the Z-load case show higher strain values for the same loads than those obtained in the X- and Y-load cases. For instance, the highest strain value of 816.775 μm/m at 3.630 kN was recorded by strain gauge CH8_SG4_P4 in channel 8 for the Z-load case. The strain value for the same strain gauge was 131.487 μm/m at 4.89 kN and 359.893 μm/m at 4.1 kN for the X- and Y-load cases, respectively. This implied that the prototype nose wheel fork was much stronger in the X and Y loading directions in position 4, where this strain gauge was connected.

4.8   Performance test summary

All three sets of strain versus force curves had a similar pattern that represented the behaviour of the strain gauges when the loads were applied to the prototype scaled-down nose wheel fork. This behaviour confirmed the expected repeatability of all strain gauges when the loads were applied. The highest load was in the Z-direction of testing. Here the highest strain value of 1793.787 μm/m in strain gauge CH 7_SG_3_P3 was obtained. The geometry of the scaled-down nose wheel fork in position 3 in Figure 3.8 is in the form of an I-beam. During the bending of an I-beam, when the load is applied perpendicular to the flanges, it is expected that the web will experience lower strain [83], hence the highest strain value on strain gauge CH 7_SG_3_P3 in the Z-loading direction. However, it is still a fairly small strain value for a load of 8.48 kN; hence there was no failure in the prototype scaled-down nosewheel fork.

In general, the scaled-down nose wheel fork performed to the expectation: no failure for all static tests in all directions of testing. This data could also be used as a guide for more comprehensive performance testing, such as HCF because the areas of high strain values were already identified experimentally without any failure of the nose wheel fork.

CHAPTER 5: CONCLUSIONS AND RECOMMENDATIONS FOR FUTURE WORK

5.1 Conclusions

The aim of this study was to generate experimental data on the static operational performance of a light aircraft nose wheel landing gear fork, which was produced through LPBF of Ti6Al4V(ELI), that would contribute to the validation of the design of this component. For this purpose, a scaled-down prototype of the nose wheel fork was produced through DMLS in Ti6Al4V(ELI).

It was found that the as-built and stress relieved followed by high temperature annealing Ti6Al4V(ELI) tensile test specimens, built with optimized DMLS building process parameters, exhibited mechanical properties compliant with the ASTM F3001 – 14 standard and high density with porosity levels lower than 0.01% were recorded.

The data generated for improving the quality of DMLS-built Ti6Al4V(ELI) parts for HCF applications in this study were consistent with previously reported data from other studies that followed similar procedures to improve the mechanical properties of DMLS Ti6Al4V(ELI) parts.

Fractography and HCF test results confirmed that the inherent DMLS surface roughness significantly impacted the HCF performance of the Ti6Al4V(ELI) test specimens. This implies that surface finishing would be needed to improve fatigue performance for applications such as structural aerospace components.

Under static performance test conditions, the prototype scaled-down nose wheel fork did not experience any failure or permanent deformation, even for the maximum load case. This contribution to the more comprehensive study of Mr L. F. Monaheng will eventually contribute to the use of LPBF Ti6Al4V(ELI) for structural aerospace components, such as the nose wheel fork.

5.2 Recommendations for future work

Appropriate surface finishing techniques for load-bearing structural parts produced through DMLS should be further researched to achieve the required improvement of the performance of such structural components.

On completion of Mr L. F. Monaheng's doctoral study to which the current study contributed, the application of applicable cost-effective surface finishing of the subsequent full-scale DMLS prototype nose wheel fork should be considered.

Hot Isostatic Pressing (HIP), known to produce parts with improved fatigue properties, was not done in this study. Therefore, the LPBF Ti6AL4V(ELI) nose wheel fork should be HIPed and tested to assess the improvement in the fatigue life of the component.

REFERENCES

[1] L. F. Monaheng, W. du Preez, N. Kotze, and M. Vermeulen, "Topology optimisation of an aircraft nose-wheel fork for production in Ti6Al4V by the Aeroswift high-speed laser powder bed fusion machine," *14th world Conf. Titan.*, vol. 321, no. 2020, p. 03013, doi: https://doi.org/10.1051/matecconf/202032103013.

[2] P. Middleton, "Aeroswift: a large-scale powder bed fusion AM system," *African Fusion*, pp. 20–23, 2018.

[3] X. Yan, S. Yin, C. Chen, C. Huang, R. Bolot, R. Lupoi, M. Kuang, W. Ma, C. Coddet, H. Liao, and M. Liu, "Effect of heat treatment on the phase transformation and mechanical properties of Ti6Al4V fabricated by selective laser melting," *J. Alloys Compd.*, vol. 764, pp. 1056–1071, 2018, doi: 10.1016/j.jallcom.2018.06.076.

[4] S. Douglas and W. Stanley, "Costs and Cost Effectiveness of Additive Manufacturing," National Institute of Standards and Technology, 2014. doi: 10.6028/NIST.SP.117.

[5] G. Nicoletto, "A novel test method for the fatigue characterization of metal powder bed fused alloys," *Procedia Struct. Integr.*, vol. 7, pp. 67–74, 2017, doi: 10.1016/j.prostr.2017.11.062.

[6] G.M. Ter Haar, "Selective Laser Melting-produced Ti6Al4V: Influence of annealing stratergies on crystallographic mirostructure on tensile behaviour," master's thesis: Mechanical Engineering,Stellenbosch University, 2017.

[7] A. Goral, "Analysis of Residual Stresses." http://www.imim.pl/PHD/www.imim-phd.edu.pl/contents/Relevant Articles/Anna Goral.pdf

[8] B. Vrancken, "Study of Residual Stresses in Selective Laser Melting," doctoral thesis, KU Leuven Arenberg doctoral school, Belgium, 2016. [Online]. Available: https://lirias.kuleuven.be/bitstream/123456789/542751/1/thesis+Bey+Vrancken+v01-06-2016+FINAL_compressed.pdf

[9] V. N. Divakaran, G. V. V Ravikumar, and S. Rao Patnala, "Aircraft

Landing Gear Design & Development," *Infosys - White paper*, pp. 1–17, 2018. [Online]. Available: https://www.infosys.com/engineering-services/white-papers/Documents/landing-gear-design-and-development.pdf

[10] I. van Zyl, "Residual stress of Ti6Al4V (ELI) parts manufactured by direct metal laser sintering," master's thesis:Central University of Technology, 2016.

[11] N. K. Dey, "Additive manufacturing laser deposition of Ti-6Al-4V for aerospace repair application," master's thesis, Missouri University of Science and Technology, 2014.

[12] "AHRLAC-ground testing phase starts", Pilot's Post." [Online]. Available: http://pilotspost.co.za/arn0000574

[13] A. Mohammed, D. S. Memom, Y.G Pawar, and S. P. Kainge, "A Study on Landing Gear Arrangement of an Aircraft," *Int. J. Innov. Res. Sci. Eng. Technol.*, vol. 6, no. 8, pp. 15730–15738, 2017.

[14] T. Niezgoda, J. Malachowski, and W. Kowalski, "Selection of dynamics charakteristics for landing gear with the use of numerical model," in *DESIGN 2002: Proceedings of the 7th International Design Conference, Vols 1 and 2*, 2002, pp. 1085–1090.

[15] A. Armaan, S. Keshav, and G. Srinivas, "A step towards safety: Material failure analysis of landing gear," *Mater. Today Proc.*, vol. 27, pp. 402–409, 2020, doi: 10.1016/j.matpr.2019.11.245.

[16] A. Bussiba and M. Kendler, "Failure Analysis of Main Landing Gear in Civilian Aircraft," in *Proceedings of the 6th International Conference on Mechanics and Materials in Design*, 2015, pp. 1061–1074.

[17] L. A. L. Franco, N. J. Lourenço, M. L. A. Graça, O. M. M. Silva, P. P. de Campos, and C. F. A. von Dollinger, "Fatigue fracture of a nose landing gear in a military transport aircraft," *Eng. Fail. Anal.*, vol. 13, no. 3, pp. 474–479, 2006, doi: 10.1016/j.engfailanal.2004.12.025.

[18] V. Infante, L. Fernandes, M. Freitas, and R. Baptista, "Failure analysis of a nose landing gear fork," *Eng. Fail. Anal.*, vol. 82, pp. 554–565, 2017, doi: 10.1016/j.engfailanal.2017.04.020.

[19] ASM International, "History and Extractive Metallurgy," in *Titanium—Physical Metallurgy, Processing, and Applications*, 2015, p. 10.

[20] International Titanium Association, "Titanium — The Infinite Choice," 2011. [Online]. Available: http://c.ymcdn.com/sites/www.titanium.org/resource/resmgr/Docs/TiUlti mate.pdf

[21] O. Takeda, T. Ouchi, and T. H. Okabe, "Recent Progress in Titanium Extraction and Recycling," *Metall. Mater. Trans. B Process Metall. Mater. Process. Sci.*, vol. 51, no. 4, pp. 1315–1328, 2020, doi: 10.1007/s11663-020-01898-6.

[22] D. Prando, A. Brenna, M. V. Diamanti, S. Beretta, F. Bolzoni, M. Ormellese, and M. P. Pedeferri, "Corrosion of titanium: Part 1: Aggressive environments and main forms of degradation," *J. Appl. Biomater. Funct. Mater.*, vol. 15, no. 4, pp. e291–e302, 2017, doi: 10.5301/jabfm.5000387.

[23] W. Callister and D. Rethwisch, *Materials science and engineering: an introduction*, 7th ed., vol. 94. John Wiley & Sons, Inc., 2007. doi: 10.1016/0025-5416(87)90343-0.

[24] C. Veiga, J. P. Devim, and A. J. R. Loureiro, "Properties and applications of titanium alloys: a brief review," *Rev. Adv. Mater. Sci.*, vol. 32, no. 2, pp. 133–148, 2012.

[25] R. Pederson, "Microstructure and Phase Transformation of Ti-6Al-4V," Licentiate Thesis, Lulea University of Technology, 2002. doi: LTU-LIC-0230-SE.

[26] M. Neikter, "Microstructure and Texture of Additive Manufactured Ti-6Al-4V," Licentiate Thesis, Lulea University of Technology, 2018.

[27] A. A. Antonysamy, "Microstructure , Texture and Mechanical Property Evolution during Additive Manufacturing of Ti6Al4V Alloy for Aerospace Applications," doctoral thesis, University of Manchester, 2012.

[28] R. A. Higgins, *Engineering metallurgy Part 1 Applied physical metallurgy.*, 6th ed. ARNOLD, 1957.

[29] M. Peters, *Titanium and Titanium Alloys*, 1st ed. Wiley-VCH Verlag Gmbh & Co. KGaA, 2003. doi: 10.1002/3527602119.

[30] ASTM International, "F2792-12a - Standard Terminology for Additive Manufacturing Technologies." pp. 1–3, 2013. doi: 10.1520/F2792-12A.2.

[31] H. Bikas, P. Stavropoulos, and G. Chryssolouris, "Additive manufacturing methods and modeling approaches: A critical review," *Int. J. Adv. Manuf.*,

vol. 83, no. 1–4, pp. 389–405, 2016, doi: 10.1007/s00170-015-7576-2.

[32] W. E. Frazier, "Metal additive manufacturing: A review," *J. Mater. Eng. Perform.*, vol. 23, no. 6, pp. 1917–1928, 2014, doi: 10.1007/s11665-014-0958-z.

[33] R. A. R. Bineli, A. P. G. Peres, A. L. Jardini, and R. Maciel Filho, "Direct Metal Laser Sintering (DMLS): Technology for Design and Construction of Microreactors," *6th Brazilian Conf. Manuf. Eng.*, pp. 1–7, 2011.

[34] Crucible Design Ltd, "Design guidelines for Direct Metal Laser Sintering," 2015.

[35] K. Bari and A. Arjunan, "Extra low interstitial titanium based fully porous morphological bone scaffolds manufactured using selective laser melting," *J. Mech. Behav. Biomed. Mater.*, vol. 95, pp. 1–12, 2019, doi: 10.1016/j.jmbbm.2019.03.025.

[36] L.B. Malefane, "Determination of the fatigue properties of Ti6Al4V (ELI) parts built by a direct metal laser sintering system with standard process parameters follwed by post-proccess treatments," master's dissertation,Central University of Technology, Free State, 2019.

[37] H. Shipley, D. Mcdonnell, M. Culleton, R. Lupoi, G. O. Donnell, and D. Trimble, "Optimisation of Process Parameters to Address Fundamental Challenges during Selective Laser Melting of Ti-6Al-4V : A Review," *Int. J. Mach. Tools Manuf.*, vol. 128, pp. 1–20, 2018.

[38] M. J. Donachie, *Titanium: A technical guide*, 2nd ed. ASM International, 2000.

[39] D. Askeland and P. Fulay, *The Science & Engineering of Materials*, 6th ed. Cengage Learning, 2005. [Online]. Available: http://books.google.com/books?id=fRbZslUtpBYC&pgis=1

[40] M. Vanderhasten, L. Rabet, and B. Verlinden, "Ti-6Al-4V: Deformation map and modelisation of tensile behaviour," *Materials and Design*, vol. 29, no. 6. pp. 1090–1098, 2008. doi: 10.1016/j.matdes.2007.06.005.

[41] G. Lütjering, J. C. Williams, and A. Gysler, "Microstructure and mechanical properties of Titanium alloys," in *Microstructure and Properties of Materials*, vol. 2, 2000, pp. 1–74. doi: 10.1142/9789812793959_0001.

[42] J. Sieniawski, W. Ziaja, K. Kubiak, and M. Motyka, "Microstructure and

Mechanical Properties of High Strength Two-Phase Titanium Alloys," *Titan. Alloy. - Adv. Prop. Control*, 2013, doi: 10.5772/56197.

[43]   G. M. Moletsane, "Microstructure and mechanical properties of Ti6Al4V (ELI) parts produced by DMLS," master's dissertation: Central University of Technology, Free State, 2016.

[44]   B. Vrancken, L. Thijs, J. Kruth, and J. Van Humbeeck, "Heat treatment of Ti6Al4V produced by Selective Laser Melting : Microstructure and mechanical properties," *J. Alloys Compd.*, vol. 541, pp. 177–185, 2012, doi: 10.1016/j.jallcom.2012.07.022.

[45]   I. Yadroitsev, P. Krakhmalev, and I. Yadroitsava, "Selective laser melting of Ti6Al4V alloy for biomedical applications: Temperature monitoring and microstructural evolution," *J. Alloys Compd.*, vol. 583, pp. 404–409, 2014, doi: 10.1016/j.jallcom.2013.08.183.

[46]   ASTM International, "Standard Specification for Wrought Ti6Al4V Alloy for Surgical Implant Applications (UNS R56400)," *ASTM International, West Conshohocken, PA*, no. C. pp. 1–5, 2006.

[47]   A. Fatemi, R. Molaei, J. Simsiriwong, N. Sanaei, J. Pegues, B. Torries, N. Phan, and N. Shamsaei, "Fatigue behaviour of additive manufactured materials: An overview of some recent experimental studies on Ti-6Al-4V considering various processing and loading direction effects," *Fatigue Fract. Eng. Mater. Struct.*, vol. 42, no. 5, pp. 991–1009, 2019, doi: 10.1111/ffe.13000.

[48]   A. I. H. Committee, *Fatigue and Fracture*, Vol. 19. ASM International, 1996.

[49]   N. M. Dhansay, "Fracture Mechanics Based Fatigue and Fracture Toughness evaluation on SLM Ti-6A1-4V," master's thesis: Mechanical Engineering,University of Cape Town, 2015.

[50]   N. W. Sachs and P. E. Sachs, "Fracture Features," *J. fatigue Anal. Prev.*, vol. 5, no. 2, pp. 11–15, 2005.

[51]   L. B. Malefane, W. du Preez, and M. Maringa, "High Cycle Fatigue Properties of As-Built Ti6Al4V (Eli) Produced By Direct Metal Laser Sintering," *South African J. Ind. Eng.*, vol. 28, no. 3, pp. 1–12, 2017, doi: 10.7166/28-3-1861.

[52]   L. M. Seabra, "Design Optimisation for Selective Laser Melting (SLM)

and Experimental Testing of an Aircraft Component," master's thesis,Tecnico Lisboa, 2015.

[53] G. Nicoletto, R. Konečná, L. Kunz, and M. Frkáň, "Influence of as-built surface on fatigue strength and notch sensitivity of Ti6Al4V alloy produced by DMLS," *MATEC Web Conf.*, vol. 165, pp. 2–7, 2018, doi: 10.1051/matecconf/201816502002.

[54] X. Gong, T. Anderson, and K. Chou, "Review on Powder-Based Electron Beam Additive Manufacturing Technology," *ASME/ISCIE 2012 Int. Symp. Flex. Autom.*, p. 507, 2012, doi: 10.1115/ISFA2012-7256.

[55] N. Sanaei and A. Fatemi, "Analysis of the effect of surface roughness on fatigue performance of powder bed fusion additive manufactured metals," *Theor. Appl. Fract. Mech.*, vol. 108, p. 102638, 2020, doi: 10.1016/j.tafmec.2020.102638.

[56] M. Kahlin, H. Ansell, and J. J. Moverare, "Fatigue behaviour of notched additive manufactured Ti6Al4V with as-built surfaces," *Int. J. Fatigue*, vol. 101, pp. 51–60, 2017, doi: 10.1016/j.ijfatigue.2017.04.009.

[57] E. Wycisk, A. Solbach, S. Siddique, D. Herzog, and F. Walther, "Effects of Defects in Laser Additive Manufactured Ti-6Al-4V on Fatigue Properties," *Phys. Procedia*, vol. 56, pp. 371–378, 2014, doi: 10.1016/j.phpro.2014.08.120.

[58] P. J. Withers and H. K. D. H. Bhadeshia, "Residual stress. Part 1– Measurement techniques," *Mater. Sci. Technol.*, vol. 17, no. 4, pp. 366–375, 2001, doi: 10.1179/026708301101510087.

[59] M. Deveci, "Types of Residual Stresses," 2019. [Online]. Available: https://www.stresstech.com/download_file/view_inline/456/

[60] H. Liu, T. Sparks, F. Liou, and D. Dietrich, "ResidualStress and Deformation ModellingforMetalAdditive ManufacturingProcesses," in *Proceedings of the World Congress on Mechanical, Chemical, and Material Engineering (MCM 2015)*, 2015, p. Paper No.245.

[61] J. Sieniawski, W. Ziaja, M. Motyka, and K. Kubiak, "Microstructure and Mechanical Properties of High Strength Two-Phase Titanium Alloys," *Titan. Alloy. - Adv. Prop. Control*, no. October, 2013, doi: 10.5772/56197.

[62] M. Randt, S. Sun, M. Leary, S. Feih, J. Elambasseril, and Q. Lui, "High-Value SLM Aerospace Components: From Design to Manufacture," *Adv.*

Mater. Res., vol. 633, pp. 135–147, 2013.

[63] B. Vayre, F. Vignat, and F. Villeneuve, "Designing for additive manufacturing," *Procedia CIRP*, vol. 3, no. 1, pp. 632–637, 2012, doi: 10.1016/j.procir.2012.07.108.

[64] J. Lettori, R. Raffaeli, M. Peruzzini, J. Schmidt, and M. Pellicciari, "Additive manufacturing adoption in product design: An overview from literature and industry," *Procedia Manuf.*, vol. 51, no. 2019, pp. 655–662, 2020, doi: 10.1016/j.promfg.2020.10.092.

[65] Y. Zhang, A. Bernard, R. K. Gupta, and R. Harik, "Evaluating the design for additive manufacturing: A process planning perspective," *Procedia CIRP*, vol. 21, pp. 144–150, 2014, doi: 10.1016/j.procir.2014.03.179.

[66] ASTM International, "Standard Practice for Conducting Force Controlled Constant Amplitude Axial Fatigue Tests of Metallic Materials." pp. 1–6, 2002. doi: 10.1520/E0466-15.2.

[67] L. F. Monaheng, W. du Preez, and C. Polese, "Towards Qualification in the Aviation Industry: Impact Toughness of Ti6Al4V(ELI) Specimens Produced through Laser Powder Bed Fusion Followed by Two-Stage Heat Treatment," *Metals (Basel).*, vol. 11, no. 11, p. 1736, 2021, doi: 10.3390/met11111736.

[68] ASTM International, "F3001 − 14 Standard Specification for Additive Manufacturing Titanium-6 Aluminum-4 Vanadium ELI (Extra Low Interstitial) with Powder Bed Fusion." pp. 1–6, 2018. doi: 10.1520/F3001-14.

[69] A. Y. Al-Maharma, S. P. Patil, and B. Markert, "Effects of porosity on the mechanical properties of additively manufactured components: a critical review," *Mater. Res. Express*, vol. 7, no. 12, 2020, doi: 10.1088/2053-1591/abcc5d.

[70] V. Chastand, P. Quaegebeur, W. Maia, and E. Charkaluk, "Comparative study of fatigue properties of Ti-6Al-4V specimens built by electron beam melting (EBM) and selective laser melting (SLM)," *Mater. Charact.*, vol. 143, pp. 76–81, 2018, doi: 10.1016/j.matchar.2018.03.028.

[71] A. Du Plessis, S. G. Le Roux, J. Els, G. Booysen, and D. C. Blaine, "Application of microCT to the non-destructive testing of an additive manufactured titanium component," *Case Stud. Nondestruct. Test. Eval.*,

vol. 4, pp. 1–7, 2015, doi: 10.1016/j.csndt.2015.09.001.

[72] R. Biswal, A. K. Syed, and X. Zhang, "Assessment of the effect of isolated porosity defects on the fatigue performance of additive manufactured titanium alloy," *Addit. Manuf.*, vol. 23, no. August, pp. 433–442, 2018, doi: 10.1016/j.addma.2018.08.024.

[73] J. R. Poulin, A. Kreitcberg, P. Terriault, and V. Brailovski, "Fatigue strength prediction of laser powder bed fusion processed Inconel 625 specimens with intentionally-seeded porosity: Feasibility study," *Int. J. Fatigue*, vol. 132, no. September 2019, p. 105394, 2020, doi: 10.1016/j.ijfatigue.2019.105394.

[74] Z. A. Mierzejewska, R. Hudák, and J. Sidun, "Mechanical properties and microstructure of DMLS Ti6Al4V alloy dedicated to biomedical applications," *Materials (Basel).*, vol. 12, no. 1, 2019, doi: 10.3390/ma12010176.

[75] F. Liu, W. Jingchao, T. Zhi, L. Bin, G. Yue, and D. Z. Zhang, "An aerospace Integrated Component Application Based on Selective Laser Melting: Design, Fabrication and Fe Simulation," in *Proceedings of the 29th Annual International Solid Freeform Fabrication Symposium – An Additive Manufacturing Conference*, 2018, pp. 488–499.

[76] M. Dallago, V. Fontanari, E. Torresani, M. Leoni, C. Pederzolli, C. Potrich, and M. Benedetti, "Fatigue and biological properties of Ti-6Al-4V ELI cellular structures with variously arranged cubic cells made by selective laser melting," *J. Mech. Behav. Biomed. Mater.*, vol. 78, pp. 381–394, 2018, doi: 10.1016/j.jmbbm.2017.11.044.

[77] A. A. Benzerga and J. B. Leblond, *Advances in Applied Mechanics*, vol. 44, no. December. 2010. doi: 10.1016/S0065-2156(10)44003-X.

[78] H. Gong, K. Rafi, T. Starr, and B. Stucker, "Effect of defects on fatigue test of as-built TI6AL4V parts fabricated by selective laser melting," vol. 66, pp. 37–39, 2012.

[79] P. Hartunian and M. Eshraghi, "Effect of build orientation on the microstructure and mechanical properties of selective laser-melted Ti-6Al-4V Alloy," *J. Manuf. Mater. Process.*, vol. 2, no. 69, pp. 2–13, 2018, doi: 10.3390/jmmp2040069.

[80] K. S. R. Chandran, "Duality of fatigue failures of materials caused by

Poisson defect statistics of competing failure modes," *Nat. Mater.*, vol. 4, no. 4, pp. 303–308, 2005, doi: 10.1038/nmat1351.

[81] G. Lutjering, "Influence of processing on microstructure and mechanical properties of (alpha + beta) titanium alloys," vol. 243, pp. 32–45, 1998.

[82] I. Yadroitsev, P. Krakhmalev, I. Yadroitsava, and A. Du Plessis, "Qualification of Ti6Al4V ELI Alloy Produced by Laser Powder Bed Fusion for Biomedical Applications," *Jom*, vol. 70, no. 3, pp. 372–377, 2018, doi: 10.1007/s11837-017-2655-5.

[83] B. Dupen, *Applied Strength of Materials for Engineering Technology*, vol. 10. Research & Creativity at IPFW, 2016.

APPENDICES

APPENDIX 1: Tensile and fatigue test specimen dimensions
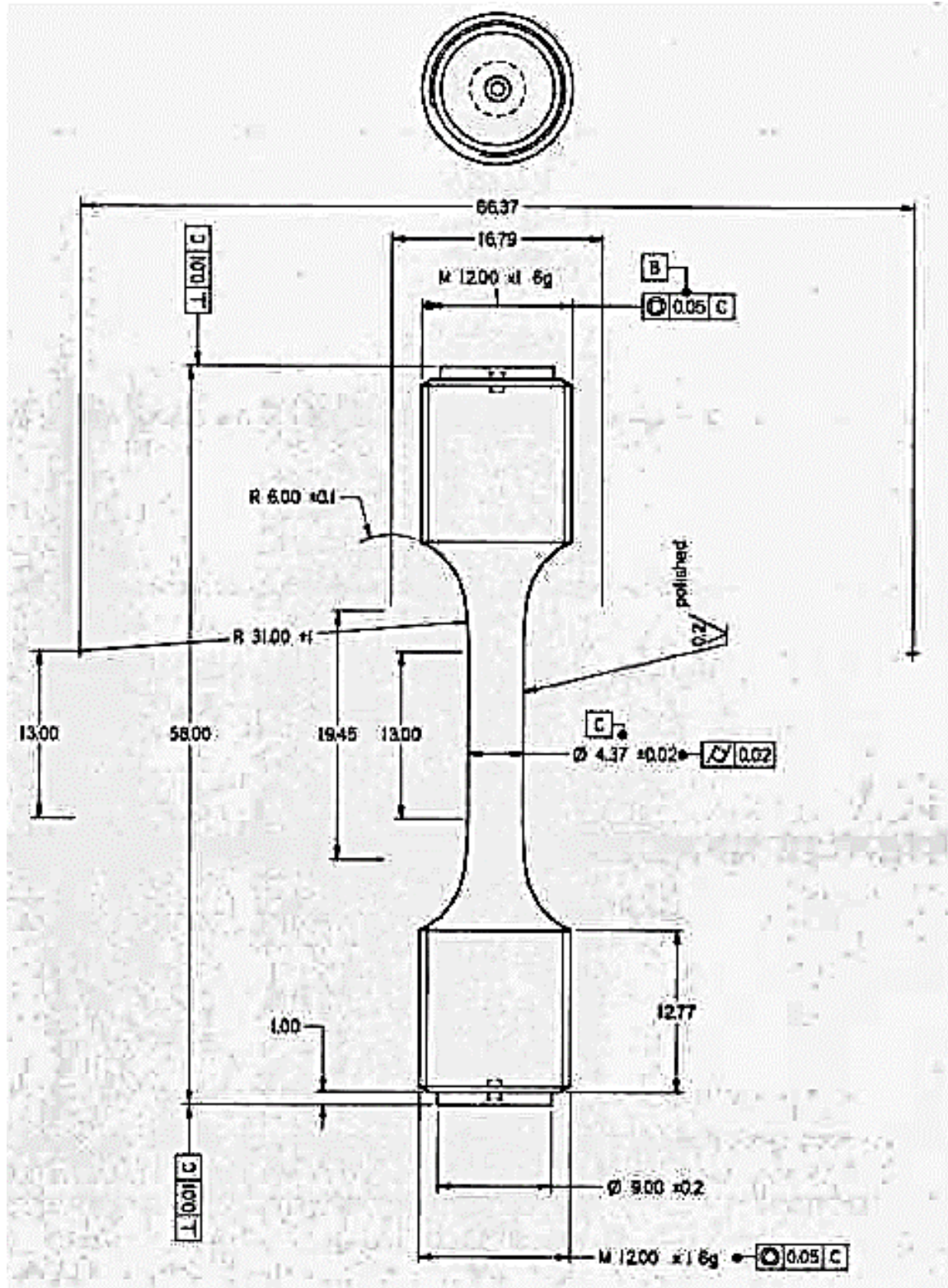
APPENDIX 2: Test instruction plan for a scaled-down nose wheel fork

■ AHRLAC NOSEWHEEL FORK PROJECT

Design review: Changing of the material for nose wheel fork performance test jig

COMPILED BY: HP Miya (M.Eng. student in Mechanical and Mechatronics Engineering)

DATE OF DESIGN REVIEW: 24 January 2022

REVIEWED BY: Prof Willie du Preez (Main supervisor)

LF Monaheng (Co-supervisor)

1. Introduction

Central University of technology (CUT) contracted Product Development Technology Station (PDTS) to do manufacturing of the test jig according to the design that was approved by CUT and University of Pretoria (UP) Team, see Appendix 1. PDTS encountered challenges with the outsourcing of the central components due to suppliers not having the materials because of COVID-19 regulations.

Technical decisions were made to utilise the substitute materials that are available in the country (South Africa), and the test jig subsequently came to completion. Figure 1 and table 1 present these changes.
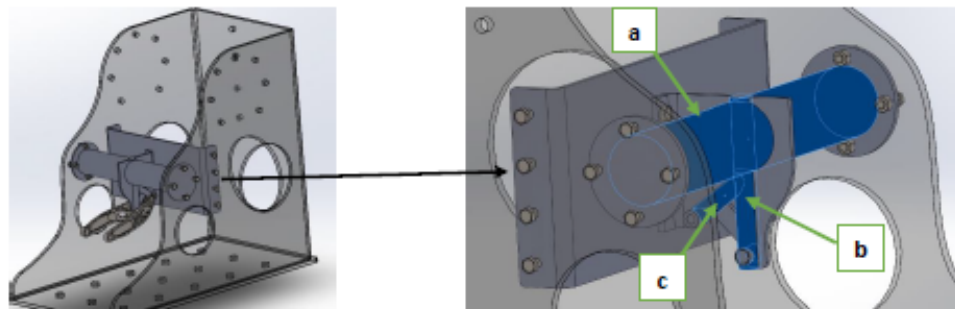
Figure 1: Central components of the test jig for which the metals had to be substituted. a) small scale central support tube. b) small scale shock absorber tube.   c) small scale shock torque-arm tube.

Table 1: List of the test jig central components with their substitutes:

Component number:	Material initially planned for use	Substitute material
a	60x3 mm mild steel round tube	65 mm EN 24 round bar
b	21x3 mm mild steel round tube	20 mm EN 24 round bar
c	21x3 mm mild steel round tube	16 mm EN 24 round bar

The substitute materials were successfully outsourced, and this brought to completion the manufacturing of the test jig. See figure 2 for the completed test jig.

Figure 3: Test jig with the scale-down nose wheel fork of the AHRLAC aircraft.

2. Approval of the test jig design changes.

By signing this document, the following team members agree that they have reviewed the design changes of the scaled-down nose wheel fork test jig and they agree that the changes should be implemented in manufacturing phase.

3. CUT team members

Mr HP Miya: .... Date: ....24 January 2022.......

Mr LF Monaheng: .... Date: ....31 January 2022.......

Prof WB du Preez: .... Date: ....30 March 2022.......

4. PDTS reviewers

Name: ...Mr HP Miya... **Signature** .... **Capacity:** ...Project Engineer Jnr..(Project leader) **Date:** 24 January 2022

Name: Mr R Masheane **Signature** .... **Capacity:** ...Project Engineer........... **Date:** 09 May 2022

Project review: Design of nose wheel fork performance test jig

COMPILED BY: HP Miya (M.Eng. student in Mechanical and Mechatronics Engineering)

REVIEWED BY: Prof Willie du Preez (Main supervisor)

LF Monaheng (Co-supervisor)

---

1. Introduction

The AHRLAC company has included additive manufacturing (AM) in its manufacturing strategy. Manufacturing of the AHRLAC nose wheel fork in Ti6Al4V (ELI) through selective laser melting (SLM) was selected as a pilot project for undercarriage parts of the aircraft. As part of this project, the performance of prototype SLM Ti6Al4V (ELI) nose wheel forks has to be tested under simulated operational load conditions. For this testing, collaboration was established between the Central University of Technology, Free State (CUT) and the University of Pretoria (UP). The intention was to execute the performance test of the nose wheel fork at the Centre for Asset Integrity Management (C-AIM) of UP.

2. Performance test jig design

Technical meetings between the CUT students and experts at UP were held to discuss and plan the design of the test jig for this performance testing. The jig was designed to fit the available testing equipment in the C-AIM at UP. The maximum loads acting in the X, Y, and Z planes must be applied in a sinusoidal form and for a single load case at a time. This loading sequence would only require one actuator. It is expected that with a simple sinusoidal loading fatigue test, enough data would be obtained to validate the design of the SLM Ti6Al4V (ELI) nose wheel fork.

This test jig will be used to test the fatigue behaviour of both the scaled-down and full-scale prototype nose wheel forks. In Figure 1 the test jig design in the testing facilities according to UP specifications is illustrated. It is important to note that a single actuator will be used at the time for applying loads in the x, y, z directions.
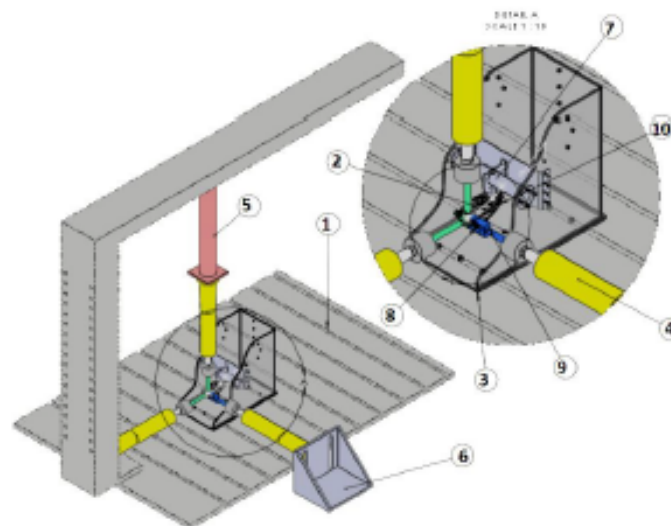
Figure 1: The assembly of the performance test jig that accommodates both scaled-down and full-scale nose wheel forks. A single actuator will be used for each load case.

The types of equipment necessary for the experimental tests are indicated in table 1. Some equipment will be provided by the UP and others including the assembly are the responsibility of CUT. The items in Table 1 are labelled according to the numbering in Figure 1 and are mainly for testing the scaled-down nose wheel fork.

Table 1: Necessary equipment for experimentation

Item No.	Equipment description	Quantity	Supplier
1	Isolation bed	1	UP
2	Ti6Al4V (ELI) nose wheel fork	1	CUT
3	Test jig and assembly	1	CUT
4	16 kN Actuator with load cell	1	UP
5	Extension beam	1	UP
6	Actuator holder	1	UP
7	Fork fixation bracket	1	CUT
8	Wheel shaft	1	CUT
9	Side loading link (Y-Link)	1	CUT
10	Shock strut shaft	1	CUT
11	Toque arm shaft	1	CUT
12	Data acquisition system (8 Channel)	1	CUT
13	Strain gauges (rosettes)	2	CUT

In Figure 2, the links between the nose wheel fork and the hydraulic actuator through the load cell are illustrated. These connections were designed to accurately apply and record the required force on the nose wheel fork. Given this design, a calibration of the load cell will be necessary before the test commences.
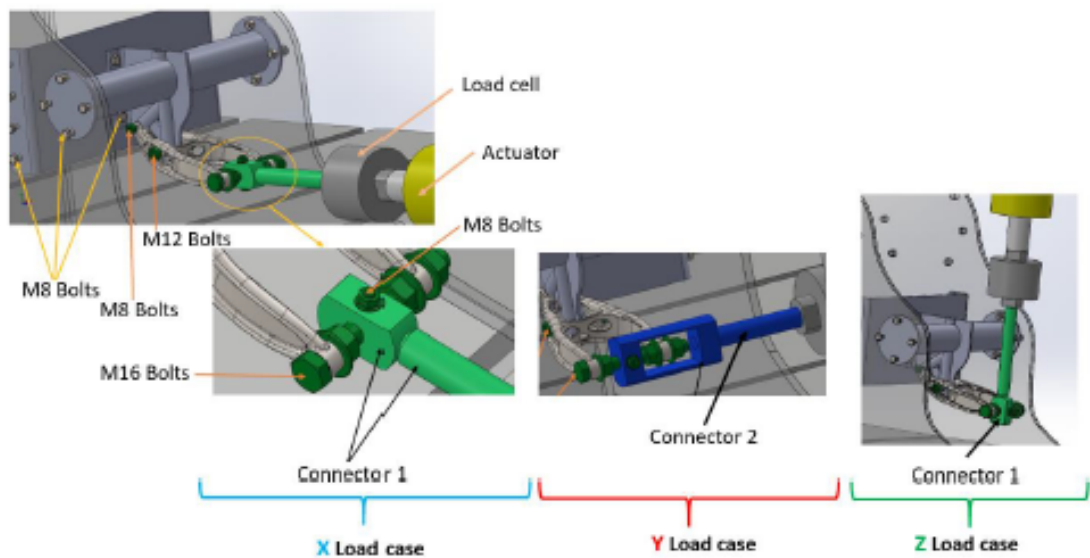
Figure 2: Illustration of the connectiors to be used for the different load cases applied to the nose wheel fork by the hydraulic actuator through the load cell.

3. Jig strength determination

The test jig was designed and validated for fit-for-purpose using finite element analysis (FEA). Three linear elastic FEAs were performed at the maximum loads of Fx = 13 960 N, Fy = 8 395 N and Fz = 20 711 N. All loads were applied through the jig on the nose wheel fork, as it will be done during experimentation. Boundary conditions were set on the cylindrical surfaces of the holes by restricting them to translate in all directions. In Figure 3 the FEA results are shown.
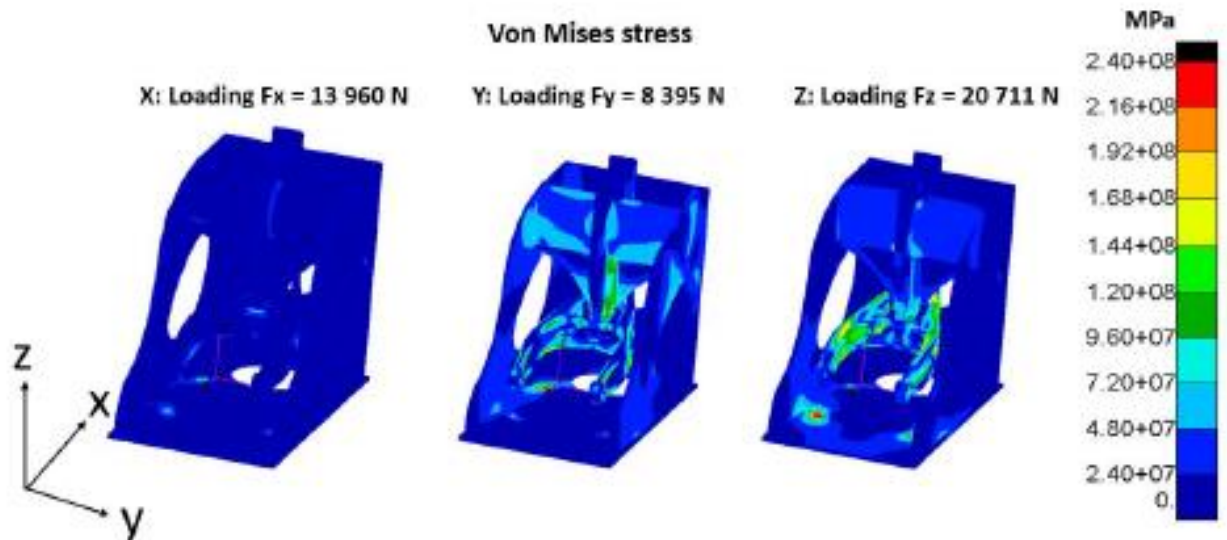
Figure 3: FEA results of the test jig simulated under three orthogonal directional maximum loads.

A stress concentration of 240 MPa was noticed in an area for the Z load case. However, it is below the fatigue limit of the mild steel. Therefore, the jig will be manufactured from a mild steel plate with a minimum thickness of 10 mm.

4. Material specifications

The jig will be manufactured from the materials stated in Table 2. The housing of the jig will be fabricated using normal mild steel, while high strength steel will be used for the connecting shaft.. This was decided based on the FEA results obtained. The shaft experiences more stress than the housing since it has the points of load application and the nose wheel fork fixation points.

Table 2: Material properties of the jig

Materials	Hardness (BHN)	UTS (MPa)	YS (MPa)	Elongation (%)
High strength steel (for shafts) EN 24 Steel	248-302	850 -1000	650	13
Jig housing & other components. (EN 10025-S335JR Steel plate)	146 - 187	490 - 630	355	20

5. Performance test procedure

The performance testing will be done in two phases. In Phase 1, a scaled-down nose wheel fork will be tested at loads which are 40% of the magnitude of the loads on the full-scale nose wheel fork. All sinusoidal loads Fx, Fy, and Fz, which are 5 584 N, 3 358 N, and 8 285 N, respectively, will be applied on the scaled-down nose wheel fork. For each load case, the load will be applied gradually on the fork until the required load level is reached and the sinusoidal loading will be repeated for 5 million cycles. In Phase 2, the full-scale nose wheel fork will be tested under maximum load and the same boundary conditions that were set in Phase 1. The maximum loads applicable to the full-scale nose wheel fork Fx, Fy and Fz are 13 960 N, 8 395 N and 20 711 N, respectively. In both Phase 1 and 2, strain gauges will be used to collect fatigue strain data related to fatigue. This data will be used to assess the fatigue behaviour of the nose wheel fork produced in Ti6Al4V (ELI) through SLM.

6. Determination of experimental frequency

The jig will be mounted on the isolated test floor, which has a T-slot base and a natural frequency of about 1 Hz. With the knowledge of the isolation bed natural frequency, the impact of external loads resulting from the fixation points will be taken into consideration during the analysis of the results.

The experimental frequency must be such that the nose wheel fork does not resonate, since it is well known that resonance in any structure can result in catastrophic mechanical failure. The resonance occurs when the natural frequency is equal to the frequency of the applied external force. Therefore, it is necessary to determine the natural frequency of the nose wheel fork. To avoid catastrophic failure, the experimentation will therefore be performed at 5% less than the natural frequency. To determine the natural frequency of the nose wheel fork equation 1 was used.

$$f_n = \frac{1}{2\pi}\sqrt{\frac{g}{\delta}}$$

(1)

Where, f_n, g and δ represent natural frequency, gravitational acceleration and static deflection, respectively.

The static deflection was calculated using the FEA method, due to the complexity of the nose wheel fork geometrical shape. This was followed by the determination of the natural frequency, experimental frequency and the number of days required for each experiment. See all these details in Tables 3 and 4 for the full scale and scaled-down nose wheel forks, respectively.

Table 3: Experimental test parameters for performance testing of the full-scaled nose wheel fork

Experiment ID Full scaled fork	Loads(N)	Maximum Von Mises stress (MPa)	Deflection (mm)	Natural frequency (Hz)	Experimental frequency (5% less than the natural frequency	Duration of experiments in days to achieve 5×10^8 cycles
Experiment 1	Fx = 13 960	115	1.41	13.28	12.62	5
Experiment 2	Fy = 8 395	195	6.48	6.20	5.89	10
Experiment 3	Fz= 20 711	407	5.56	6.69	6.36	9
					Total number of days of testing	24 days

Table 4: Experimental test parameters for performance testing of the scaled-down nose wheel fork

Experiment ID Scaled-down fork	Loads(N)	Maximum Von Mises stress (MPa)	Deflection (mm)	Natural frequency (Hz)	Experimental the frequency (5% less than the natural frequency	Duration of experiments in days to achieve 5×10^8 cycles
Experiment 1	Fx= 5 584	263	1.13	14.83	14.09	4
Experiment 2	Fy = 3 358	479	5.23	6.90	6.56	9
Experiment 3	Fz = 8 285	855	4.60	7.35	6.98	8
					Total number of days of testing	21 days

In total, the scaled-down nose wheel fork will be tested for 21 days, whereas 24 days will be needed to test a full-scaled nose wheel fork.

7. Approval of the test jig design.

By signing this document, the following team members agree that they have reviewed the design of the scaled-down nose wheel fork test jig and they agree that the design can be frozen.

8. CUT team members

Mr HP Miya: .... Date ....17 September 2020

Mr LF Monaheng: .... Date ....16 Sep. 20

Prof WB du Preez: .... Date: ......17 September 2020...

9. UP team members

Prof PS Heyns .... Date....2020/11/13............

APPENDIX 3: Universal amplifier specifications (MX840A)

QUANTUM X
MX840A

Universal amplifier

Special features

– 8 individually configurable inputs
  (electrically isolated)
– Connection of more than 12
  transducers technologies
– Data rate: up to 19,200 Hz
– 24–bit A/D converter per channel
  for synchronous, parallel
  measurements
– Active low pass filter
– TEDS support
– Supply voltage (DC): 10 V ... 30 V
– Supply voltage for active
  transducers (DC): 5 V ... 24 V

Block diagram

B2924-1.1 en

HBM
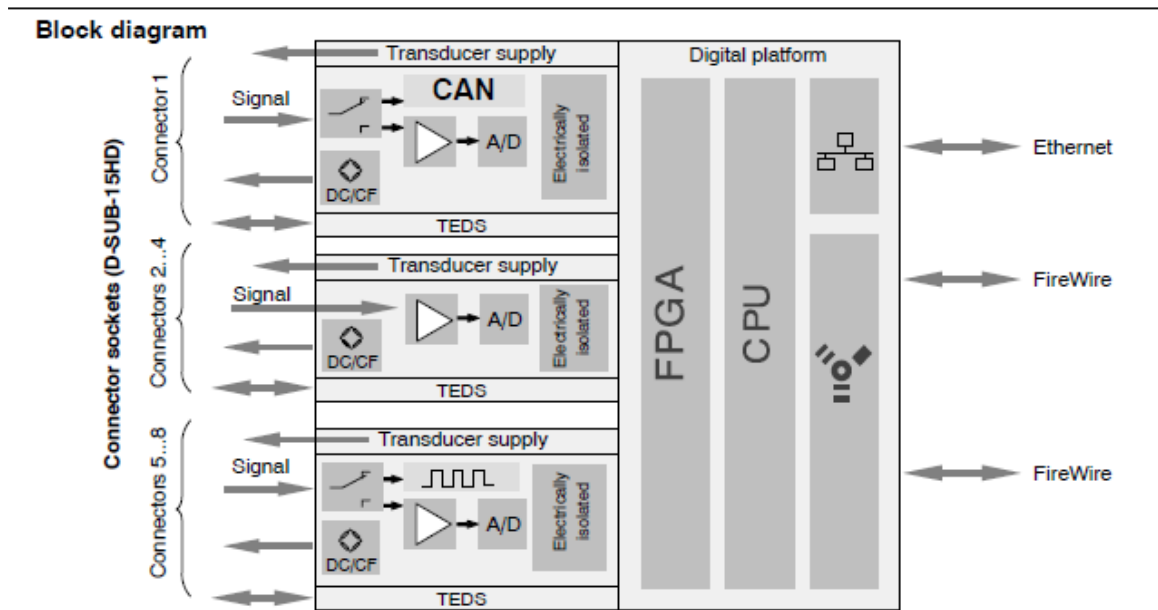
Specifications MX840A

General specifications		
Inputs	Number	8, electrically isolated from each other and from the supply voltage[1]
Transducer technologies		Strain gage full and half bridge, inductive full and half bridge, piezoresistive full bridge, potentiometric transducers, three voltage ranges, current; resistance (e. g. PTC, NTC, KTY); resistance thermometer (PT100, PT1000); thermocouples (K, N, E, T, S, ...) with cold junction in the plug (1–THERMO–MXBOARD). Frequency, pulse counting, SSI, incremental rotary encoder (connectors 5–8 only) CAN (ISO 11898; connector 1 only)
A/D converter		24 Bit Delta Sigma converter
Data rate	Hz	0.1 ... 19200, adjustable for each channel
Active low-pass filter (Bessel/Butterworth, can be switched off)	Hz	0.01 ... 3200 (–3 dB)
Transducer identification (TEDS, IEEE 1451.4) max. distance of the TEDS module	m	100
Transducer connection		D-SUB-15HD
Supply voltage range (DC)	V	10 ... 30 (24 V nominal (rated) voltage)
Supply voltage interruption		max. 5 ms at 24 V
Power consumption without adjustable transducer excitation with adjustable transducer excitation	 W W	 < 9 < 12
Transducer Excitation (active transducers) Adjustable supply voltage (DC) Maximum output power	 V W	 5 ... 24; adjustable for each channel 0.7 each channel / a total of 2
Ethernet (data link) Protocol/addressing Connection Max. cable length to module	 – – m	10Base-T / 100Base-TX TCP/IP (direct IP address or DHCP) 8P8C plug (RJ-45) with twisted pair cable (CAT-5) 100
FireWire (module synchronization, data link, optional supply voltage) Baud rate Max. current from module to module Max. cable length between the nodes Max. number of modules connected in series (daisy chain) Max. number of modules in a FireWire system (including hubs[2], backplane) Max. number of hops[3]	 MBaud A m – – –	IEEE 1394b (HBM modules only) 400 (approx. 50 MByte/s) 1.5 5 12 (=11 Hops) 24 14
Nominal (rated) temperature range	°C [°F]	–20 ... +60 [–4 ... +140]
Operating temperature range (no dewing allowed/module not dew-point proof)	°C [°F]	–20 ... +65 [–4 ... +149]
Storage temperature range	°C [°F]	–40 ... +75 [–40 ... +167]
Rel. humidity at 31 °C	%	80 (non condensing) lin. reduction to 50 % at 40 °C
Protection class (up to 2000 m height, degree of contamination 2)		III
Degree of protection		IP20 per EN 60529
Mechanical tests[4] Vibration (30 min) Shock (6 ms)	 m/s² m/s²	 50 350
EMC requirements		per EN 61326
Max. input voltage at transducer socket to ground (Pin 6) PIN 1, 2, 3, 4, 5, 7, 8, 10, 13, 15 PIN 14 (voltage)	 V V	 5.5 (no transients) 60 (no transients)/typ. 500
Dimensions, horizontal (W x H x D)	mm	52.5 x 200 x 124 (with case protection) 44 x 174 x 124 (without case protection)
Weight, approx.	g	980

[1] When the variable transducer supply is used, there is no electrical isolation from the supply voltage.

[2] Hub: FireWire node or distributor

[3] Hop: Transition from module to module or signal conditioning / distribution via FireWire (hub, backplane)

[4] Mechanical stress is tested according to European Standard EN60068–2–6 for vibrations and EN60068–2–27 for shock. The equipment is subjected to an acceleration of 50 m/s² in a frequency range of 5...65 Hz in all 3 axes. Duration of this vibration test: 30min per axis. The shock test is performed with a nominal acceleration of 350 m/s² for 6 ms, half sine pulse shape, with 3 shocks in each of the 6 possible directions.

Specifications MX840A (Continued)

5 mV/V CF strain gage full bridge with 1 V or 2.5 V excitation (AC, effective)		
Accuracy class		0.05
Carrier frequency (sine)	Hz	4800 ±1.5
Bridge excitation voltage (effective)	V	1 and 2.5 (± 5 %)
Transducers that can be connected		strain gage full bridges
Permissible cable length between MX840A and transducer	m	100

Measuring ranges
    at 2.5 V excitation
    at 1 V excitation
	mV/V
	mV/V
		±5
		±10

Measurement frequency range (−3 dB)	kHz	0 ... 1.6

Transducer impedance
    at 2.5 V excitation
    at 1 V excitation
	Ω
	Ω
		300 ... 1000
		80 ... 1000

Noise at 25 °C and 2.5 V excitation (peak to peak)
    with filter 1 Hz Bessel
    with filter 10 Hz Bessel
    with filter 100 Hz Bessel
    with filter 1 kHz Bessel
	μV/V
	μV/V
	μV/V
	μV/V
		< 0.2
		< 0.5
		< 1
		< 4

Linearity error	%	< 0.02 of full scale
Zero drift (2.5 V excitation)	% / 10 K	0.02 of full scale
Full-scale drift (2.5 V excitation)	% / 10 K	< 0.05 of measurement value

5 mV/V CF strain gage half bridge with 1 V or 2.5 V excitation (AC, effective)		
Accuracy class		0.1
Carrier frequency (sine)	Hz	4800 ±1.5
Bridge excitation voltage (effective)	V	1 and 2.5 (± 5 %)
Transducers that can be connected		strain gage half bridges
Permissible cable length between MX840A and transducer	m	100

Measuring ranges
    at 2.5 V excitation
    at 1 V excitation
	mV/V
	mV/V
		±5
		±10

Measurement frequency range (−3 dB)	kHz	0 ... 1.6

Transducer impedance
    at 2.5 V excitation
    at 1 V excitation
	Ω
	Ω
		300 ... 1000
		80 ... 1000

Noise at 25 °C and 2.5 V excitation (peak to peak)
    with filter 1 Hz Bessel
    with filter 10 Hz Bessel
    with filter 100 Hz Bessel
    with filter 1 kHz Bessel
	μV/V
	μV/V
	μV/V
	μV/V
		< 0.5
		< 0.7
		< 1
		< 4

Linearity error	%	< 0.02 of full scale
Zero drift (2.5 V excitation)	% / 10 K	0.1 of full scale
Full-scale drift (2.5 V excitation)	% / 10 K	< 0.1 of measurement value

Specifications MX840A (Continued)

100 mV/V DC piezoresistive strain gage full bridge with 2.5 V (DC) excitation		
Accuracy class		0.05
Excitation voltage (DC)	V	2.5 ± 5%
Transducers that can be connected		piezoresistive strain gage full bridges
Permissible cable length between MX840A and transducer	m	100
Measuring range	mV/V	± 100
Measurement frequency range (–3 dB)	kHz	0 ... 3.2
Transducer impedance	Ω	300 ... 1000
Noise at 25 °C (peak to peak) with filter 1 Hz Bessel with filter 10 Hz Bessel with filter 100 Hz Bessel with filter 1 kHz Bessel	µV/V µV/V µV/V µV/V	< 4 < 6 < 15 < 60
Linearity error	%	< 0.02 of full scale
Zero drift	% / 10 K	< 0.02 of full scale
Full-scale drift	% / 10 K	< 0.05 of measurement value

1000 mV/V DC piezoresistive strain gage full bridge with 2.5 V (DC) excitation		
Accuracy class		0.05
Bridge excitation voltage (DC)	V	2.5 ± 5%
Transducers that can be connected		piezoresistive strain gage full bridges
Permissible cable length between MX840A and transducer	m	100
Measuring range	mV/V	± 1000
Measurement frequency range (–3 dB)	kHz	0 ... 3.2
Transducer impedance	Ω	300 ... 1000
Noise at 25 °C (peak to peak) with filter 1 Hz Bessel with filter 10 Hz Bessel with filter 100 Hz Bessel with filter 1 kHz Bessel	µV/V µV/V µV/V µV/V	< 40 < 100 < 200 < 700
Linearity error	%	< 0.02 of full scale
Zero drift	% / 10 K	< 0.02 of full scale
Full-scale drift	% / 10 K	< 0.05 of measurement value

Specifications MX840A (Continued)

100 mV/V CF inductive full bridge with 1 V or 2.5 V excitation (AC, effective)		
Accuracy class		0.05
Carrier frequency (sine)	Hz	4800 ±1.5
Bridge excitation voltage (effective)	V	1 and 2.5 (±5 %)
Transducers that can be connected		inductive full bridges
Permissible cable length between MX840A and transducer	m	100
Measuring ranges at 2.5 V excitation at 1 V excitation	mV/V mV/V	±100 ±300
Measurement frequency range (−3 dB)	kHz	0 ... 1.6
Transducer impedance at 2.5 V excitation at 1 V excitation	Ω Ω	300 ... 1000 80 ... 1000
Noise at 25 °C and 2.5 V excitation (peak to peak) with filter 1 Hz Bessel with filter 10 Hz Bessel with filter 100 Hz Bessel with filter 1 kHz Bessel	μV/V μV/V μV/V μV/V	< 3 < 5 < 15 < 50
Linearity error	%	< 0.02 of full scale
Zero drift (2.5 V excitation)	% / 10 K	< 0.02 of full scale
Full-scale drift (2.5 V excitation)	% / 10 K	< 0.05 of measurement value

1000 mV/V CF inductive full bridge with 1 V excitation (AC, effective)		
Accuracy class		0.1
Carrier frequency (sine)	Hz	4800 ±1.5
Bridge excitation voltage (effective)	V	1 (±5 %)
Transducers that can be connected		inductive full bridges
Permissible cable length between MX840A and transducer	m	100
Measuring range	mV/V	±1000
Measurement frequency range (−3 dB)	kHz	0 ... 1.6
Transducer impedance	Ω	80 ... 1000
Noise at 25 °C (peak to peak) with filter 1 Hz Bessel with filter 10 Hz Bessel with filter 100 Hz Bessel with filter 1 kHz Bessel	μV/V μV/V μV/V μV/V	< 40 < 100 < 500 < 1200
Linearity error	%	< 0.02 of full scale
Zero drift	% / 10 K	< 0.02 of full scale
Full-scale drift	% / 10 K	< 0.1 of measurement value

Specifications MX840A (Continued)

100 mV/V CF inductive half bridge with 1 V or 2.5 V excitation (AC, effective)		
Accuracy class		0.1
Carrier frequency (sine)	Hz	4800 ± 1.5
Bridge excitation voltage (effective)	V	1 and 2.5 (± 5 %)
Transducers that can be connected		inductive half bridges
Permissible cable length between MX840A and transducer	m	100
Measuring ranges at 2.5 V excitation at 1 V excitation	 mV/V mV/V	 ± 100 ± 300
Measurement frequency range (−3 dB)	kHz	0 ... 1.6
Transducer impedance at 2.5 V excitation at 1 V excitation	 Ω Ω	 300 ... 1000 80 ... 1000
Noise at 25 °C and 2.5 V excitation (peak to peak) with filter 1 Hz Bessel with filter 10 Hz Bessel with filter 100 Hz Bessel with filter 1 kHz Bessel	 µV/V µV/V µV/V µV/V	 < 3 < 5 < 15 < 50
Linearity error	%	< 0.02 of full scale
Zero drift (2.5 V excitation)	% / 10 K	< 0.1 of full scale
Full-scale drift (2.5 V excitation)	% / 10 K	< 0.1 of measurement value

LVDT		
Accuracy class		0.1
Carrier frequency (sine)	Hz	4800 ± 1.5
Bridge excitation voltage (effective)	V	1 (± 5 %)
Transducers that can be connected		LVDT
Permissible cable length between MX840A and transducer	m	100
Measuring range	mV/V	± 3000
Measurement frequency range (−3 dB)	kHz	0 ... 1.6
Transducer impedance	mH	4 ... 33
Noise at 25 °C (peak to peak) with filter 1 Hz Bessel with filter 10 Hz Bessel with filter 100 Hz Bessel with filter 1 kHz Bessel	 µV/V µV/V µV/V µV/V	 < 40 < 100 < 500 < 1200
Linearity error	%	< 0.02 of full scale
Zero drift	% / 10 K	< 0.1 of full scale
Full-scale drift	% / 10 K	< 0.1 of measurement value

Specifications MX840A (Continued)

Potentiometric transducer		
Accuracy class		0.1
Excitation voltage (DC)	V	2.5 (± 5 %)
Transducers that can be connected		potentiometric transducers
Permissible cable length between MX840A and transducer	m	100
Measuring range	mV/V	± 500
Measurement frequency range (−3 dB)	kHz	0 ... 3.2
Transducer impedance	Ω	300 ... 5000
Noise at 25 °C (peak to peak) with filter 1 Hz Bessel with filter 10 Hz Bessel with filter 100 Hz Bessel with filter 1 kHz Bessel	µV/V µV/V µV/V µV/V	< 40 < 100 < 200 < 700
Linearity error	%	< 0.02 of full scale
Zero drift (1 V excitation)	% / 10 K	< 0.1 of full scale
Full-scale drift (1 V excitation)	% / 10 K	< 0.1 of measurement value

10 V DC voltage		
Accuracy class		0.05
Transducers that can be connected		voltage generator up to ± 10 V
Permissible cable length between MX840A and transducer	m	100
Measuring range	V	± 10
Measurement frequency range (−3 dB)	kHz	0 ... 3.2
Internal resistance of the voltage source	Ω	< 500
Internal impedance, typ.	MΩ	1
Noise at 25 °C (peak to peak) with filter 1 Hz Bessel with filter 10 Hz Bessel with filter 100 Hz Bessel with filter 1 kHz Bessel	µV µV µV µV	< 150 < 300 < 600 < 3000
Linearity error	%	< 0.02 of full scale
Common-mode rejection with DC common mode with 50 Hz common mode, typ.	dB dB	> 100 75
Maximum common-mode voltage (to housing and supply ground)	V	± 60
Zero drift	% / 10 K	< 0.02 of full scale
Full-scale drift	% / 10 K	< 0.05 of measurement value

Specifications MX840A (Continued)

60 V DC voltage		
Accuracy class		0.05
Transducers that can be connected		voltage generator up to ± 60 V
Permissible cable length between MX840A and transducer	m	100
Measuring range	V	± 60
Measurement frequency range (–3 dB)	kHz	0 ... 3.2
Internal resistance of the voltage source	Ω	< 500
Input impedance, typ.	MΩ	1
Noise at 25 °C (peak to peak) with filter 1Hz Bessel with filter 10Hz Bessel with filter 100Hz Bessel with filter 1kHz Bessel	µV µV µV µV	< 150 < 300 < 600 < 3000
Linearity error	%	< 0.02 of full scale
Common-mode rejection with DC common mode with 50 Hz common mode, typ.	dB dB	> 100 75
Maximum common-mode voltage (to housing and supply ground)	V	± 60
Zero drift	% / 10 K	< 0.02 of full scale
Full-scale drift	% / 10 K	< 0.05 of measurement value

100 mV DC voltage		
Accuracy class		0.1
Transducers that can be connected		voltage generator
Permissible cable length between MX840A and transducer	m	100
Measuring range	mV	± 300
Measurement frequency range (–3 dB)	kHz	0 ... 3.2
Input impedance	MΩ	> 20
Noise at 25 °C (peak to peak) with filter 1 Hz Bessel with filter 10 Hz Bessel with filter 100 Hz Bessel with filter 1 kHz Bessel	µV µV µV µV	< 5 < 100 < 1000 < 1500
Linearity error	%	< 0.03 of full scale
Common-mode rejection with DC common mode with 50 Hz common mode, typ.	dB dB	> 90 75
Maximum common-mode voltage (to housing and supply ground)	V	± 30
Zero drift	% / 10 K	< 0.1 of full scale
Full-scale drift	% / 10 K	< 0.1 of measurement value

Specifications MX840A (Continued)

20 mA DC current		
Accuracy class		0.05
Transducers that can be connected		transducers with current output (0 ... 20 mA or 4 ... 20 mA)
Permissible cable length between MX840A and transducer	m	100
Measuring range	mA	± 30
Measurement frequency range (–3 dB)	kHz	0 ... 3.2
Measurement resistance value, typ.	Ω	10
Noise at 25 °C (peak to peak) with filter 1 Hz Bessel with filter 10 Hz Bessel with filter 100 Hz Bessel with filter 1 kHz Bessel	µA µA µA µA	< 1 < 1.5 < 15 < 40
Linearity error	%	< 0.02 of full scale
Common-mode rejection with DC common mode with 50 Hz common mode, typ.	dB dB	> 100 75
Maximum common-mode voltage (to housing and supply ground)	V	± 30
Zero drift	% / 10 K	< 0.05 of full scale
Full-scale drift	% / 10 K	< 0.05 of measurement value

Resistance		
Accuracy class		0.1
Transducers that can be connected		PTC, NTC, KTY, TT-3, resistances generally (connection with 4 wire configuration)
Permissible cable length between MX840A and transducer	m	100
Measuring ranges	Ω	0 ... 5000
Speisestrom	mA	0.4 ... 0.8
Measurement frequency range (–3 dB)	kHz	0 ... 3.2
Noise at 25 °C (peak to peak) with filter 1 Hz Bessel with filter 10 Hz Bessel with filter 100 Hz Bessel with filter 1 kHz Bessel	K K K K	< 0.5 < 1 < 2 < 6
Linearity error	%	< ± 0.02 of full scale
Zero drift	%/10K	<0.02 of full scale
Full-scale drift	% / 10 K	<0.1 of measurement value

Resistance thermometer (PT100, PT1000)		
Accuracy class		0.1
Transducers that can be connected		PT100, PT1000 (connection with 4 wire configuration)
Permissible cable length between MX840A and transducer	m	100
Linearization range	°C [°F]	–200 ... +848 [–328 ... +1558.4]
Measurement frequency range (–3 dB)	kHz	0 ... 3.2
Noise at 25 °C (peak to peak) with filter 1 Hz Bessel with filter 10 Hz Bessel with filter 100 Hz Bessel with filter 1 kHz Bessel	K K K K	< 0.1 < 0.2 < 0.5 < 1.5
Linearity error	K	< ± 0.3
Zero drift with PT100 with PT1000	K / 10 K K / 10 K	<0.2 <0.1
Full-scale drift with PT100 with PT1000	K / 10 K K / 10 K	<0.5 <1

Specifications MX840A (Continued)

Thermocouples[5]		
Transducers that can be connected		Thermocouples (type B, E, J, K, N, R, S, T)
Permissible cable length between MX840A and transducer	m	100
Measuring range	mV	±100
Linearization ranges		
Type B (Pt-30 % Rh and Pt-6 % Rh)	°C [°F]	+100 ... +1820 [+212 ... +3308]
Type E (Ni-Cr and Cu-Ni)	°C [°F]	−200 ... +900 [−328 ... +1652]
Type J (Fe and Cu-Ni)	°C [°F]	−210 ... +1200 [−346 ... +2192]
Type K (Ni-Cr and Ni-Al)	°C [°F]	−270 ... +1372 [−454 ... +2501.6]
Type N (Ni-14,2 % Cr and Ni-4,4 % Si-0,1 % Mg)	°C [°F]	−270 ... +1300 [−454 ... +2372]
Type R (Pt-13 % Rh and Pt)	°C [°F]	−50 ... +1768 [−58 ... +3214.4]
Type S (Pt-10 % Rh and Pt)	°C [°F]	−50 ... +1768 [−58 ... +3214.4]
Type T (Cu and Cu-Ni)	°C [°F]	−270 ... +400 [−454 ... +752]
Transducer impedance	Ω	< 500
Measurement frequency range (−3 dB)	kHz	0 ... 3.2
Noise at 25 °C and Type K (peak to peak)		
with Filter 1 Hz Bessel	K	0.05
with Filter 10 Hz Bessel	K	0.1
with Filter 100 Hz Bessel	K	0.5
with Filter 1 kHz Bessel	K	1
Zero error		
Type E, J, K, T	K	<±0.3
Type N, R, S	K	<±3
Type B	K	<±30
Linearity error		
Type E, J, K, T	K	<±0.3
Type N, R, S	K	<±3
Type B	K	<±30
Max. error of the cold junction	K	<±0.5
Total error limit		
Type E, J, K, T	K	±1
Type N, R, S	K	±6.5
Type B	K	±60
Temperature drift (type K)	K/10 °C	<±1
Cold junction 1−THERMO−MXBOARD		
Nominal (rated) temperature range	°C [°F]	−20 ... +60 [−4 ... +140]
Operating temperature range	°C [°F]	−20 ... +65 [−4 ... +149]
Storage temperature range	°C [°F]	−40 ... +75 [−40 ... +167]

[5] The external cold junction is required for connecting thermocouples to the MX840A (Order no.: 1−THERMO−MXBOARD).

Specifications MX840A (Continued)

Frequency or pulse counting (connections 5 ... 8)		
Accuracy class		0.01
Transducers that can be connected		HBM-torque transducers, Frequency signal sources (square), incremental encoder, pulse counters, SSI transducers
Permissible cable length between MX840A and transducer	m	50
Signals $F_1 (\pm)$ $F_2 (\pm)$ Zero index $(\pm)$		Frequency or pulse signal Direction of rotation signal shifted by $\pm 90^\circ$ to F_1 Zero position signal
Input level with differential operation Low level High level		Differential inputs (RS422): Signal (+) < Signal (–) –200 mV Differential inputs (RS422): Signal (+) > Signal (–) +200 mV
Input level with unipolar operation Low level High level	V V	<1.5 > 3.5
Maximum input voltage at transducer socket to ground (pin 6)	V	5.5 (no transients)
Measuring ranges Frequency Pulse counting	Hz pulses/s	0.1 ... 1,000,000 0 ... 1,000,000
Input impedance, typ.	kΩ	10
Temperature drift	%/10K	< 0,01 of measurement value
SSI mode (differentially) Shift clock Word length Code Input level Low level High level Signals Data Shift clock	kHz Bit	100, 200, 500, 1000 12–31 dual or gray Differential inputs (RS422): Signal (+) < Signal (–) –200 mV Differential inputs (RS422): Signal (+) > Signal (–) +200 mV Data+, Data– (RS-422) Clk+, Clk– (RS-422)

Digital control output (Triggering shunt calibration, reset of external charge amplifiers)		
Output type		open collector
Reference potential		Pin 6 (ground)
High level Output unloaded, typ. I_{out} = 5 mA	V V	5 > 4.5
Leakage current (high impedance output)	µA	< 1
Permissible load impedance	kΩ	> 1

CAN (connection 1/read only)						
Supported protocols		CAN 2.0A, CAN 2.0B				
Number of CAN ports		1 (connection 1)				
Bus link		two wire, according to ISO11898				
Baud rates and permissible cable lengths	kBit/s m	1000, 25,	500, 100,	250, 250,	125, 500,	100 600
Sampling rate	signals/s	max. 10,000				
CAN signals		≤ 128				
CAN signal types		standard, mode-dependent, mode-signal				

APPENDIX 4: Data recorder specifications (CX22W)

QUANTUM^X

CX22W / CX22

Data recorder

Special features

- Stand-alone data acquisition: exchangeable CF-CARD
- Connection of QuantumX modules
- Easy system configuration: trigger, computation, virtual channels, signal analysis
- Many interfaces: LAN, WLAN, USB, Digital I/O
- Touchscreen connection (optional): DVI / USB
- Supply voltage (DC): 10 V ... 30 V no fan

Block diagram

Front	Digital platform	Rear
WLAN (only CX22W)	CF-CARD	
Ethernet		
DVI	CPU Intel® Atom™	
Digital In/Out TTL		FireWire
USB 3 x		
RS-232		
MIC – IN		FireWire
AUDIO – OUT		

B3191-1.0 en

HBM

Specifications

Devices that can be connected		QuantumX MGCplus [2]
Number of channels FireWire (QuantumX) Ethernet NTP (QuantumX, MGCplus Cp42, Interrogator)		384 (24 modules x 16 Channels) 400
Synchronization options		FireWire (only QuantumX, automatica, recommended) Ethernet / NTP (QuantumX / MGCplus CP42)
System configuration / Data access		Remote access or via "QuantumX Network Assistant" software Direct connection to a PC (Ethernet or WLAN) or via network (DHCP) Data access via Windows Explorer
Channel configuration		Manually via integrated sensor database (all typical transducers, HBM sensors, CAN–dbc import, open, expandable) Automatically via TEDS (integrated editor)
Data recording / Start of recording		After switching on the operating voltage Triggered (pre–trigger) to measurement signal, message, digital input Via software (remote access or direct connection of peripheral devices), time
Number of sample rates		3 different data rates and groups (depending on measurement module)
Formula editor (calculation channels)		Arithmetic, exponent, root, root mean square value, logic, trigonometry, integral/differential, exponential, logarithm, limit values (connect digital output, play audio file via external speaker, entry in log file), software filters (moving averages, Bessel, Butterworth), experimental stress analysis using SG
Trigger signals		Analog, bus signal, computed signals, digital input (0/1)
Trigger type		Edge (rising, falling), level (above, below)
End of recording		Switch off, manual, triggered (post), time, number of measured values
Scope of recording		Selected signals, meta data (sensors, measurement configuration, test parameters), statistics log
Recording mode		Standard Time interval (periodic file creation, without data loss) Long–term measurement (time, cycle with counter/cycle time/peak–valley) Peak values (interval) Ring buffer (up to 10 minutes)
Sequences		10 sequential recording configurations (measurement jobs), repetitions
Storage formats		HBM catman® (bin) ASCII (asc, replay with MX878) Microsoft Excel® (xls, xlsx, xlsb) MTS (RPC III) MathWorks MATLAB™ (mat) HBM nCode (dac) Vector (MDF 4.0) NI DIAdem (dac)
Automation		Key scripting (Visual Basic for application)
Data storage		Exchangeable CF card, USB stick, external USB hard disk
Display or remote control		
Online display **Recommended display**		Freely configurable display and control panels in full screen mode 1024 x 768 pixels DVI digital [1]
Display elements		Numeric display, line recorder (y–t, x–y, y–f / FFT), spreadsheet, indicator, bar graph, LED, polar diagram, switch (button), checkbox, selection box, background image, text
Keypad		Control via function keys

[1] DVI–2–VGA adapter does not work

[2] QuantumX and MGCplus CP42 can be synchronized via Ethernet NTP. The CX22(–W) can be used as NTP Master.

Specifications

Protection		
System change		Enhanced Write Filter (EWF) needs to be opened to save changes.

General specifications		
Operating system		WindowsXP embedded
Prozessor		Intel Atom, 1.33 GHz with 533 MHz FSB
Internal storage medium	GB	8, two partitions
Exchangeable memory 　Version 　Formfactor 　Memory capacity, max. 　Recording rate, max. 　Measured value / Signal	 GByte Values/s Byte	CompactFlash 4.1 CompactFlash type 1 128 800000 4
Starting time, approx.	sec	45
Interfaces (number)[1]		Ethernet (1) WLAN (1) FireWire (2) USB2.0 (3) RS232(1) DVI (1) Digital I/O (6)
Supply voltage range (DC)	V	10 ... 30, nominal (rated) voltage 24V
Power consumption (at 24V)	W	< 12, no rotating parts (fans), no noise
Ethernet (Konfiguration des Datenrekorders) 　Protocol/addressing 　Connection 　Max. cable length to module WLAN (data recorder configuration) 　WLAN standard 　Data transfer rate 　Security protocols 　Straight line range 　Frequency carrier, Country/Region 　Antenna	 m MBit m 	10Base–T / 100Base–TX / 1000Base–TX TCP/IP (direct IP address or DHCP) 8P8C plug (RJ-45) with twisted pair cable (CAT-5) 100 IEEE 802.11 n/h and IEEE 802.11 b/g, Adhoc-support 54 WEP, WPA, WPA2, TKIP, AES 200 (IEEE 802.11n) 2.4 GHz Standard SMA socket, Typ RF Coax
FireWire (module synchronization, data link, optional supply voltage) 　Baud rate 　Max. current from module to module 　Max. cable length between the nodes 　Max. number of modules connected in series (daisy chain) 　Max. number of modules in a FireWire system (including hubs[2], backplane) 　max. chain of hops[3]	 MBaud A m 	IEEE 1394b (HBM modules only) 400 (approx. 50 MByte/s) 1.5 5 12 (=11 hops) 24 14
USB 　Version / Connector 　Cable length, max.	 m	2.0/Standard Highspeed (Host) compatible with Version 1.1 5
RS-232-C 　Connector 　Baud rate, max. 　Devices	 kBaud 	DSUB 9–pin 115 e.g. GPS (NMEA)
DVI 　Type		Digital, connecting LCD monitor

[1] Rack installation not possible
[2] Hub: FireWire node or distributor
[3] Hop: Transition from module to module/signal conditioning

Specifications

Protection class (up to 2000 m height, degree of contamination 2)		III
Line out / voice output		Jack, 3.5 mm
Degree of protection		IP20
Mechanical tests[1]		
Vibration (30 min)	m/s^2	50
Shock (6 ms)	m/s^2	350
EMC requirements		according to EN61326
Nominal (rated) temperature range	°C [°F]	−20 °C ... +60 °C [−4 ... +140]
Operating temperature range (no dewing allowed/module not dew-point proof)	°C [°F]	−20 °C ... +65 °C [−4 ... +149]
Storage temperature range	°C [°F]	−40 °C ... +75 °C [−40 ... +167]
Rel. humidity at 31 °C	%	80 (non condensing) lin. reduction to 50 % at 40 °C
Weight, approx.	g	1200
Dimensions, horizontal (H x W x D)	mm	52.5 x 200 x 122 (with case protection) 44 x 174 x 119 (without case protection)
Real Time Clock		
Clock drift		max. 1.2 minutes per month
Time buffering		CMOS Batterie
Time zone (factory settings)		UTC (Universal Time, Coordinated)
Digital I/Os		
Number of inputs/outputs		6 3 inputs (clamps 1, 2, 3) 3 outpust (clamps 4, 5, 6)
Type of connection		screw terminals Plug: MC 1,5/7−ST−3,5 (Phoenixcontact)
LEDs (number) output state		3
Cable length (max.)	m	3
Cable type (required with interference)		shielded
Input signal range TTL		
Max. permissible input level	V	−0.5 ... 5.5
Input level High	V	4
Input level Low	V	0.7
Internal pullup resistors	kOhm	100
Output signal range TTL		
Output High	V	4
Output Low	V	0.7
Output current max.	mA	1

[1] Mechanical stress is tested according to European Standard EN60068−2−6 for vibrations and EN60068−2−27 for shock. The equipment is subjected to an acceleration of 25 m/s^2 in a frequency range of 5...65 Hz in all 3 axes. Duration of this vibration test: 30min per axis. The shock test is performed with a nominal acceleration of 200 m/s^2 for 11 ms, half sine pulse shape, with shocks in each of the 6 possible directions.

APPENDIX 5: Actuator controller data: Force peak values in volts

X- load case

Load division 1	Load division 2	Load division 3	Load division 4	Load division 5
0,6052419	1,228849	1,802829	2,45757	3,12E+00
0,606839	1,228176	1,802349	2,458635	3,12E+00
0,6098506	1,229509	1,803697	2,458071	3,12E+00
0,6088958	1,229907	1,804213	2,457442	3,12E+00
0,6057624	1,227969	1,804689	2,457652	3,12E+00
0,6044196	1,227877	1,803951	2,458228	3,12E+00
0,6055599	1,228826	1,801583	2,458904	3,12E+00
0,6072652	1,228486	1,802524	2,458744	3,12E+00
0,6070093	1,227428	1,803993	2,45865	3,12E+00
0,60477	1,227085	1,802146	2,457857	3,12E+00
0,6022176	1,227198	1,800392	2,456542	3,12E+00
0,6014552	1,227156	1,79912	2,457921	3,12E+00
0,6029783	1,227302	1,799524	2,458913	3,12E+00
0,6037709	1,227125	1,80184	2,457448	3,12E+00
0,6026825	1,227336	1,80176	2,457581	3,12E+00
0,6016477	1,228891	1,801144	2,458112	3,12E+00

Y- load case

Load division 1	Load division 2	Load division 3	Load division 4	Load division 5
-0,4099826	-0,7930673	-1,214471	-1,540456	-2,05E+00
-0,4090685	-0,793586	-1,21451	-1,540719	-2,05E+00
-0,4096882	-0,7936916	-1,214433	-1,541355	-2,05E+00
-0,4100119	-0,7933894	-1,214323	-1,541087	-2,05E+00
-0,4098425	-0,7936658	-1,214476	-1,540274	-2,047019
-0,4091719	-0,7935431	-1,21496	-1,540391	-2,047183
-0,4090876	-0,7935933	-1,214685	-1,540702	-2,047269
-0,4104634	-0,7946133	-1,214467	-1,540504	-2,047538

-0,4101099	-0,7944874	-1,214539	-1,540545	-2,047575
-0,4093925	-0,7934437	-1,214218	-1,540262	-2,047399
-0,4100696	-0,7933997	-1,214529	-1,54107	-2,046645
-0,4098585	-0,7933333	-1,214437	-1,542489	-2,047122
-0,4093335	-0,7932424	-1,214503	-1,541836	-2,048721
-0,4094222	-0,7939082	-1,215505	-1,541683	-2,048514
-0,4098109	-0,7943498	-1,215048	-1,541982	-2,047867
-0,4097211	-0,7936183	-1,214683	-1,540972	-2,047997

Z- load case

Load division 1	Load division 2	Load division 3	Load division 4	Load division 5
-0,9021346	-1,658939	-2,618229	-3,430433	-4,24E+00
-0,9029101	-1,658915	-2,618898	-3,430138	-4,24E+00
-0,9038466	-1,659591	-2,619511	-3,43045	-4,24E+00
-0,9032576	-1,660172	-2,619297	-3,43131	-4,24E+00
-0,9024044	-1,659315	-2,6184	-3,430718	-4,245124
-0,9026717	-1,659294	-2,618921	-3,429706	-4,244807
-0,9026464	-1,659613	-2,619289	-3,430674	-4,245395
-0,9022462	-1,659076	-2,618436	-3,430346	-4,245244
-0,9030509	-1,659892	-2,618523	-3,429649	-4,244957
-0,9030405	-1,660331	-2,619283	-3,431651	-4,245938
-0,9025628	-1,659891	-2,619486	-3,431189	-4,246548
-0,9034611	-1,660346	-2,618913	-3,429385	-4,246277
-0,9036573	-1,659983	-2,619009	-3,429674	-4,246424
-0,9032302	-1,659695	-2,619514	-3,429809	-4,246785
-0,9028736	-1,660962	-2,618768	-3,430565	-4,246601
-0,902767	-1,661336	-2,618996	-3,430155	-4,246694

APPENDIX 6: Strain gauge data: Strain peak values in μm/m

X- load case

Load division 1: 1.206 kN

CH 1	CH 2	CH 3	CH 4	CH 5	CH 6	CH 7	CH 8
0,335	2,1	-1,88	34,2392	-29,826	-19,21	6,17	-43,29
0,269	2,04	-1,94	34,1808	-29,966	-19,2	6,19	-43,38
0,184	2,01	-1,93	34,1536	-29,996	-19,03	6,14	-43,31
0,134	2,1	-1,87	34,2218	-29,726	-18,92	6,06	-43,19
0,138	2,34	-1,86	34,1777	-29,416	-18,85	6,03	-43,14
0,213	2,27	-1,9	34,0885	-29,436	-18,73	5,95	-43,09
0,184	1,97	-1,94	34,0512	-29,616	-18,81	5,9	-43,11
0,03	1,77	-1,9	34,0043	-29,746	-18,82	5,89	-43,16
0,035	1,91	-1,88	33,9971	-29,616	-18,86	5,91	-43,14
0,114	2,08	-1,95	34,0713	-29,346	-18,86	5,97	-43,1
0,147	2,17	-1,94	34,1795	-29,146	-18,88	6,01	-43,08
0,243	2,04	-1,91	34,1614	-29,176	-18,91	5,98	-43,04
0,229	2,01	-1,95	34,0536	-29,346	-18,93	5,97	-42,97

Load division 2: 2.424 kN

CH 1	CH 2	CH 3	CH 4	CH 5	CH 6	CH 7	CH 8
-2,602	7,22	-9,05	73,51	-69,973	-43,039	15,56	-83,46
-2,623	7,19	-9,07	73,53	-70,033	-43,046	15,6	-83,53
-2,514	7,25	-9,11	73,59	-69,863	-43,037	15,65	-83,62
-2,53	7,23	-9,16	73,69	-69,993	-43,04	15,62	-83,67
-2,591	7,15	-9,12	73,65	-70,363	-43,022	15,59	-83,68
-2,505	7,27	-9,14	73,56	-70,483	-43,092	15,64	-83,71
-2,511	7,46	-9,16	73,59	-70,423	-43,131	15,77	-83,84
-2,52	7,4	-9,16	73,58	-70,343	-43,103	15,81	-83,92
-2,559	7,24	-9,1	73,57	-70,273	-43,189	15,72	-83,83

CH 1	CH 2	CH 3	CH 4	CH 5	CH 6	CH 7	CH 8
-2,452	7,19	-9,07	73,66	-70,123	-43,145	15,67	-83,69
-2,34	7,35	-9,03	73,68	-69,923	-42,834	15,62	-83,67
-2,485	7,3	-9,06	73,61	-70,113	-42,752	15,56	-83,74
-2,6	7,21	-9,12	73,58	-70,563	-42,876	15,62	-83,81

Load division 3: 3.582 kN

CH 1	CH 2	CH 3	CH 4	CH 5	CH 6	CH 7	CH 8
-6,854	13,48	-24,5	103,13	-105,753	-63,73	34,24	-107,12
-6,757	13,67	-24,42	103,27	-105,813	-63,73	34,2	-107,19
-6,784	13,68	-24,42	103,33	-105,803	-63,71	34,14	-107,19
-6,683	13,62	-24,42	103,4	-105,893	-63,69	34,11	-107,18
-6,587	13,64	-24,44	103,39	-106,063	-63,66	34,14	-107,2
-6,894	13,69	-24,45	103,31	-106,043	-63,69	34,12	-107,22
-7,208	13,67	-24,51	103,28	-106,003	-63,69	34,13	-107,29
-7,142	13,76	-24,58	103,32	-105,933	-63,54	34,22	-107,31
-6,846	13,71	-24,57	103,31	-105,873	-63,53	34,28	-107,32
-6,652	13,66	-24,49	103,28	-105,773	-63,67	34,23	-107,26
-6,674	13,69	-24,4	103,2	-105,793	-63,66	34,16	-107,12
-6,912	13,8	-24,4	103,17	-105,863	-63,56	34,21	-107,09
-6,851	13,96	-24,5	103,16	-105,853	-63,57	34,28	-107,14

Load division 4: 4.892 kN

CH 1	CH 2	CH 3	CH 4	CH 5	CH 6	CH 7	CH 8
-9,433	17,57	-29,46	122,84	-132,037	-75,35	42,42	-126,13
-9,233	17,64	-29,38	123	-131,967	-75,33	42,46	-126,15
-9,223	17,73	-29,3	123,01	-132,157	-75,31	42,49	-126,24
-9,463	17,67	-29,28	122,96	-132,377	-75,27	42,47	-126,29
-9,643	17,45	-29,34	122,98	-132,397	-75,27	42,4	-126,27
-9,373	17,42	-29,41	123,02	-132,277	-75,29	42,38	-126,25
-9,083	17,6	-29,4	123,04	-132,147	-75,34	42,38	-126,23

-9,183 17,74 -29,33 123,04 -132,017 -75,22 42,34 -126,15

-9,273 17,73 -29,23 123,02 -132,107 -75,14 42,35 -126,15

-9,293 17,65 -29,23 122,91 -132,207 -75,26 42,39 -126,11

-9,333 17,69 -29,3   122,91 -132,327 -75,37 42,4   -126,07

-9,363 17,57 -29,36 122,93 -132,487 -75,35 42,42 -126,12

-9,413 17,47 -29,43 122,97 -132,377 -75,45 42,43 -126,19

Load division 5: 6.120 kN

CH 1	CH 2	CH 3	CH 4	CH 5	CH 6	CH 7	CH 8
-14,807	21,2	-36,74	158,29	-184,3259	-96,79	71,51	-154,18
-14,767	21,23	-36,82	158,24	-184,4459	-96,79	71,47	-154,3
-14,727	21,43	-36,88	158,16	-184,5359	-96,61	71,55	-154,44
-14,617	21,56	-36,92	158,29	-184,7059	-96,67	71,73	-154,64
-14,437	21,61	-36,98	158,48	-184,8559	-96,83	71,86	-154,77
-14,447	21,58	-36,99	158,58	-184,9159	-96,9	71,83	-154,8
-14,567	21,46	-36,97	158,57	-184,8359	-96,8	71,79	-154,75
-14,697	21,42	-36,99	158,42	-184,8359	-96,69	71,77	-154,77
-14,767	21,41	-37,01	158,44	-184,9259	-96,83	71,81	-154,9
-14,647	21,4	-37,02	158,75	-185,1759	-96,91	71,92	-155,22
-14,577	21,45	-37,02	159,05	-185,2959	-97,21	72,08	-155,54
-14,677	21,46	-37,03	159,07	-185,0959	-97,35	72,16	-155,56
-14,737	21,5	-37,09	158,9	-185,1259	-97,19	72,13	-155,45
-14,797	21,52	-37,05	158,9	-185,6059	-97,2	72,15	-155,63
-14,777	21,55	-37,11	158,99	-185,9859	-97,26	72,22	-155,84
-14,777	21,62	-37,26	159,16	-186,0559	-97,32	72,29	-155,97
-14,817	21,63	-37,3	159,32	-186,0359	-97,46	72,38	-156,08
-14,767	21,51	-37,24	159,44	-186,1259	-97,45	72,51	-156,3

Y- load case

Load division 1: 0.820 kN

CH 1	CH 2	CH 3	CH 4	CH 5	CH 6	CH 7	CH 8
9,9335	-66,15	102,96	-69,373	-60,592	29,842	48,817	-126,5
9,6625	-64,19	100,45	-67,983	-59,402	28,902	49,317	-124,01
9,5015	-63,69	99,58	-67,463	-59,122	28,722	49,487	-123,27
9,5995	-63,68	99,18	-67,293	-58,932	28,362	49,537	-123,03
9,5425	-63,56	99,11	-67,333	-58,862	28,432	49,477	-122,98
9,5465	-63,22	98,94	-67,183	-58,732	28,492	49,427	-122,9

Load division 2: 1.580 kN

CH 1	CH 2	CH 3	CH 4	CH 5	CH 6	CH 7	CH 8
13,169	-91,82	128,92	-144,917	-110,191	75,012	83,713	-178,6
13,079	-92,1	129,08	-145,377	-110,391	75,182	83,983	-179,33
13,029	-92,16	129,02	-145,727	-110,601	75,452	84,183	-179,67
12,909	-92,25	129,13	-145,817	-110,511	75,342	84,243	-179,94
12,929	-92,08	129,09	-145,827	-110,541	75,432	84,313	-180,04
12,819	-90,75	127,38	-145,007	-109,661	74,752	84,703	-178,03

Load division 3: 2.420 kN

CH 1	CH 2	CH 3	CH 4	CH 5	CH 6	CH 7	CH 8
17,215	-119,432	163,81	-203,007	-150,929	109,525	110,476	-213,46
18,745	-128,742	175,38	-220,317	-164,339	119,115	121,076	-222,69
18,985	-129,892	176,38	-225,277	-167,599	122,055	125,526	-223,77
18,695	-129,722	175,84	-225,957	-167,399	122,545	126,276	-223,92
18,835	-129,632	175,79	-226,317	-167,289	122,755	126,616	-223,96
18,805	-129,792	175,64	-226,587	-167,309	122,695	126,826	-224

Load division 4: 3.100 kN

CH 1	CH 2	CH 3	CH 4	CH 5	CH 6	CH 7	CH 8
20,247	-147,053	195,81	-257,035	-192,296	140,201	138,539	-245,16
20,977	-151,573	201,3	-265,765	-197,996	145,161	143,289	-252,76
21,337	-160,743	212,65	-276,345	-207,046	150,781	146,829	-269,19
22,027	-166,213	219,17	-283,455	-213,156	154,161	150,139	-280,86
21,857	-165,493	217,98	-283,825	-213,076	154,261	151,419	-280,97
21,897	-165,143	217,47	-283,915	-212,686	154,411	151,879	-281,04

Load division 5: 4.100 kN

CH 1	CH 2	CH 3	CH 6	CH 5	CH 6	CH 7	CH 8
24,287	-197,367	258,1	-319,408	-239,626	172,92	168,79	-336,51
24,957	-211,767	275,18	-336,578	-253,176	180,52	174,59	-365,9
25,117	-210,907	273,86	-337,518	-252,126	180,64	176,7	-364,72
24,857	-210,627	273,35	-337,708	-251,456	180,49	177,55	-364,31
25,037	-210,707	272,99	-337,868	-250,966	180,55	178,05	-364,06
24,747	-210,427	272,81	-338,018	-250,856	180,65	178,35	-363,86

Z- load case

Load division 1: 1.720 kN

CH 1	CH 2	CH 3	CH 4	CH 5	CH 6	CH 7	CH 8
-36,5224	90,007	-141,813	-431,75	-149,755	317,98	453,71	546,18
-37,1224	91,547	-144,143	-434,27	-150,585	319,36	456,58	547,15
-37,3024	92,007	-144,703	-435,11	-150,925	320,02	457,19	546,97
-37,4624	92,737	-145,553	-436,29	-151,015	320,63	458,32	547,67
-37,5024	92,987	-145,953	-437,18	-151,145	321,27	459,41	548,54
-37,6224	93,437	-146,513	-437,98	-151,715	321,93	460,03	548,93

Load division 2: 3.630 kN

CH 1	CH 2	CH 3	CH 4	CH 5	CH 6	CH 7	CH 8
-63,717	148,32	-233,863	-619,82	-235,394	441,84	648,16	703,49
-76,567	160,85	-261,703	-700,16	-268,754	496,19	726,23	798,07
-81,907	166,11	-273,233	-733,24	-282,474	518,76	757,74	836,96
-83,907	168,27	-277,773	-745,27	-288,094	526,59	770,08	851,2
-84,697	168,87	-279,103	-749,4	-289,464	529,13	773,96	855,79
-84,807	169,16	-279,723	-749,09	-289,834	528,88	774,13	855,14

Load division 3: 5.140 kN

CH 1	CH 2	CH 3	CH 4	CH 5	CH 6	CH 7	CH 8
-141,159	188,42	-362,64	-1189,4	-455,239	835,26	1169,41	1481,02
-145,079	192,73	-372,11	-1219,9	-469,819	853,87	1200,41	1520,82
-144,859	192,81	-372,02	-1217,8	-469,499	851,9	1199,41	1518,62
-142,479	192,45	-369,06	-1201,6	-464,529	839,87	1188,21	1500,02
-142,109	192,6	-368,02	-1197,3	-462,919	836,84	1185,31	1495,22
-142,059	192,68	-367,92	-1196,9	-462,779	836,8	1185,11	1495,12

Load division 4: 6.860 kN

CH 1	CH 2	CH 3	CH 4	CH 5	CH 6	CH 7	CH 8
-188,302	246,2108	-487,81	-1488,29	-594,27	1014,58	1447,48	1833,27
-191,512	250,1508	-496,22	-1517,49	-607,32	1032,28	1474,48	1869,97
-192,312	251,6408	-498,86	-1527,99	-612,34	1038,58	1484,08	1882,97
-193,092	252,7808	-500,95	-1535,29	-615,58	1043,08	1490,88	1892,17
-193,952	253,5008	-502,71	-1541,69	-618,57	1046,88	1496,68	1899,87
-194,152	254,2708	-503,6	-1544,39	-619,91	1048,28	1499,38	1903,37

Load division 5: 8.480 kN

CH 1	CH 2	CH 3	CH 4	CH 5	CH 6	CH 7	CH 8
-217,795	271,18	-557,19	-1727,76	-720,24	1142,51	1672,12	2148,35
-219,865	273,72	-562,78	-1747,36	-729,64	1153,21	1689,82	2172,35
-232,535	285,89	-593,14	-1869,66	-785,79	1226,11	1794,32	2319,25
-239,615	296,75	-615,83	-1951,66	-827,2	1270,71	1871,32	2421,75
-238,925	297,05	-615,22	-1946,26	-825,8	1266,31	1868,62	2416,45
-238,565	297,09	-615,01	-1943,26	-824,48	1264,11	1866,52	2413,05

APPENDIX 7: NECSA CT Scanning results

Radiation Science

This document is the property of NECSA and shall not be used,
reproduced, transmitted or disclosed without prior written permission

necsa
We're in your world
RESEARCH AND DEVELOPMENT

PROJECT REPORT

NON-DESTRUCTIVE TESTING FOR ADDITIVE MANUFACTURED TITANIUM SAMPLES AT HIGH RESOLUTION: MIXRAD

DOC No: RS-COMMERC-REP-20002

Revision: 0

	NAME	DESIGNATION	DATE	SIGNATURE
COMPILED	Dr LC Bam	Senior Scientist: Radiography/Tomography	04 July 2020	
REVIEWED	Mr JW Hoffman	Engineer: Radiogrpahy/Tomography	04 July 2020	pp
APPROVED	Dr LC Bam	Acting Section Leader: RADTOM	04 July 2020	

Radiation Science

This document is the property of NECSA and shall not be used,
reproduced, transmitted or disclosed without prior written permission

Content

RESTRICTED

Radiation Science

This document is the property of NECSA and shall not be used,
reproduced, transmitted or disclosed without prior written permission
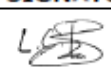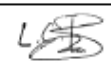
1 Introduction

Results are generated at the SANCRAT (South African Centre for Radiography and Tomography) that forms part of the National Beam Line Center located at Necsa. The flow diagram below indicates where in the organizational structure of Necsa the work was performed.
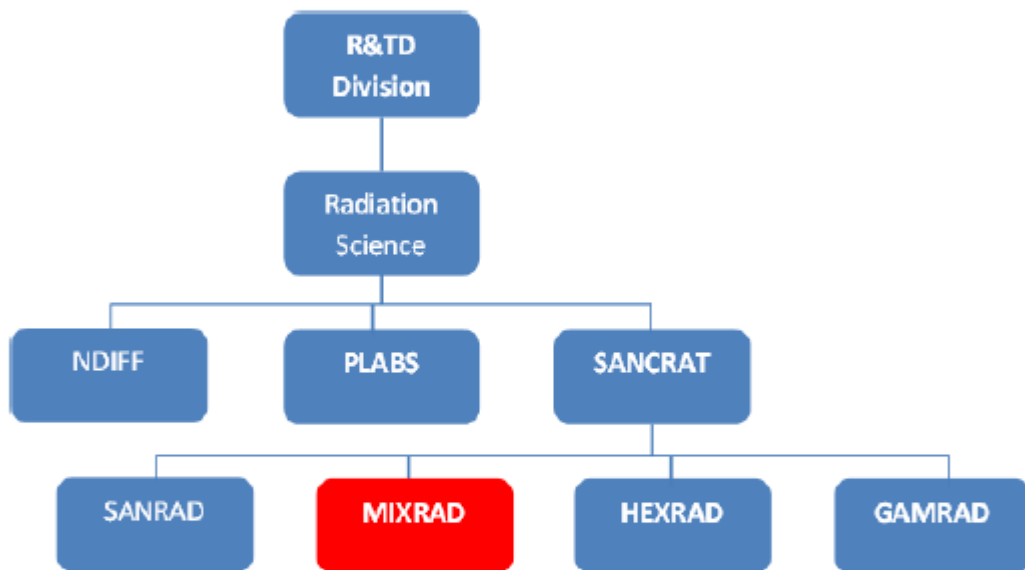
SANCRAT is part of the South African National System of Innovation and hosts 4 facilities (MIXRAD; SANRAD; HEXRAD and GAMRAD) utilizing penetrating radiation such as X-rays, neutrons and Gamma-rays. The MIXRAD is currently operational while the SANRAD undergoes massive upgrade and the latter are in a planning phase.

For this project the Micro-focus X-ray Computed Tomography (MIXRAD) facility was utilized that offers a very attractive radiation based research technique since high quality micron-level information of the interior as well as composition of samples can be obtained non-invasively and non-destructively. This application of Micro-focus X-ray tomography investigations is therefore ideal in the study of porosity measurements, porosity distribution, pore size distribution and quantification of these properties.

2 Client

Table 1: Client Information

Company	Name	Designation	Tel no	Email
CUT-CRPM	Mr Patrick Miya	Project Engineer	+27 51 507 3530	hmiya@cut.ac.za

3 Aim of the Project

Through the Micro-focus X-Ray tomography technique, the porosity of the Titanium samples were investigated:

4 MIXRAD Facility

Table 2: Micro-focus X-ray Machine Characteristics

Type	Potential range (kV)	Current range (mA)	Max Power	Detector
NIKON XTH 225 ST	30 -0225	0 to 1	30W	Perkin Elmar (2048 x 2048)

Figure 1: Micro-focus X-ray Machine (MIXRAD)

Radiation Science

This document is the property of NECSA and shall not be used,
reproduced, transmitted or disclosed without prior written permission

necsa

We're in your world

RESEARCH AND DEVELOPMENT

5 Experimental Set-up

The following MIXRAD scanning parameters for this project have been applied:

Table 3: Specific Scanning Parameters

Potential (kV)	Current (uA)	Exposure time per projection (sec)	Projections per sample
185	200	4	2000

6 Samples

The samples were supplied by CUT-CRPM and scanned using the parameters specified in Table 3 in order to obtain sufficient X-ray penetration (minimum of 10% is required) for optimal image contrast. The resolution obtained for each of the sample is reflected in Table 4.

Table 4: Resolution

Sample ID	Scanning resolution (µm)
X1	8.2
Y1	8.2
Z1b	8.2
Z1	8.2
Z3	10.5
Z4	10.5
Z5	10.5
Z7	10.5
Z8	10.5
Z11	10.5
Z12	10.5

RESTRICTED

Radiation Science

This document is the property of NECSA and shall not be used,
reproduced, transmitted or disclosed without prior written permission

necsa
We're in your world
RESEARCH AND DEVELOPMENT

7 Tomography Process

The tomography process consists of reconstructing raw 2D-projections into a 3D virtual volume by means of Nikon developed reconstruction software. The virtual digitized volume is analyzed in VGStudioMax 3.2.0 volume rendering software, which makes quantitative determination of the physical properties like porosity, mineral inclusions, fracturing, etc. possible.

8 Qualitative Results

Figures 2 – 12 depicts the 2D Slice representation of the sample.

8.1: X1 Sample – thin part

Figure 2: X1 Sample: 2D Slice in top view

Radiation Science

This document is the property of NECSA and shall not be used,
reproduced, transmitted or disclosed without prior written permission
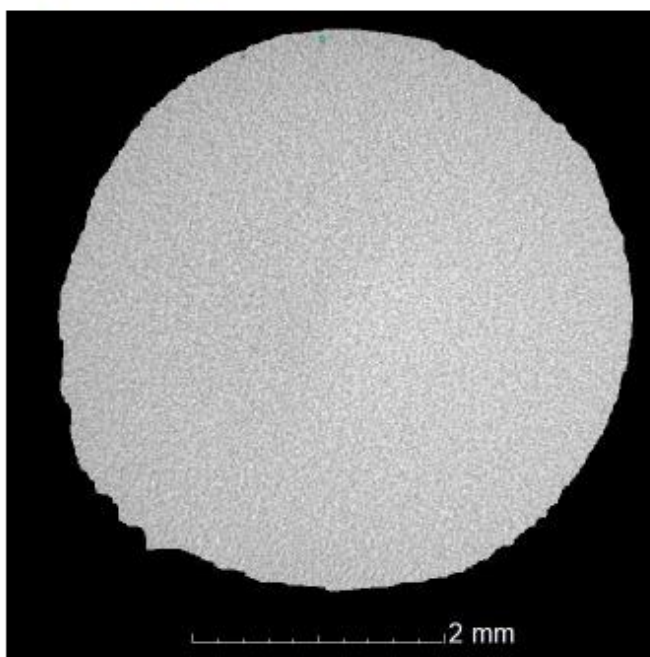
8.2: Y1 Sample – thin part
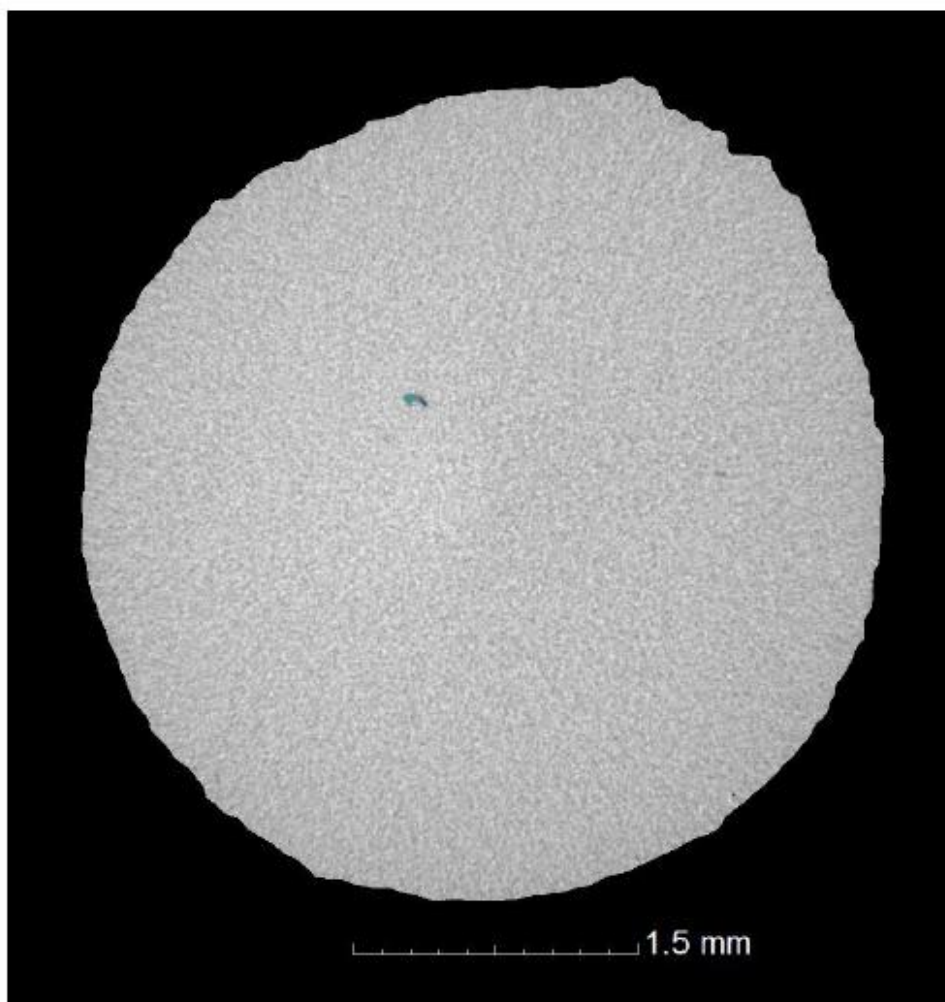
Figure 3: Y1 Sample: 2D Slice in top view

RESTRICTED

125 | P a g e

Central University of
Technology, Free State

Radiation Science
This document is the property of NECSA and shall not be used,
reproduced, transmitted or disclosed without prior written permission

necsa
We're in your world
RESEARCH AND DEVELOPMENT

8.3: Z1b Sample – thin part
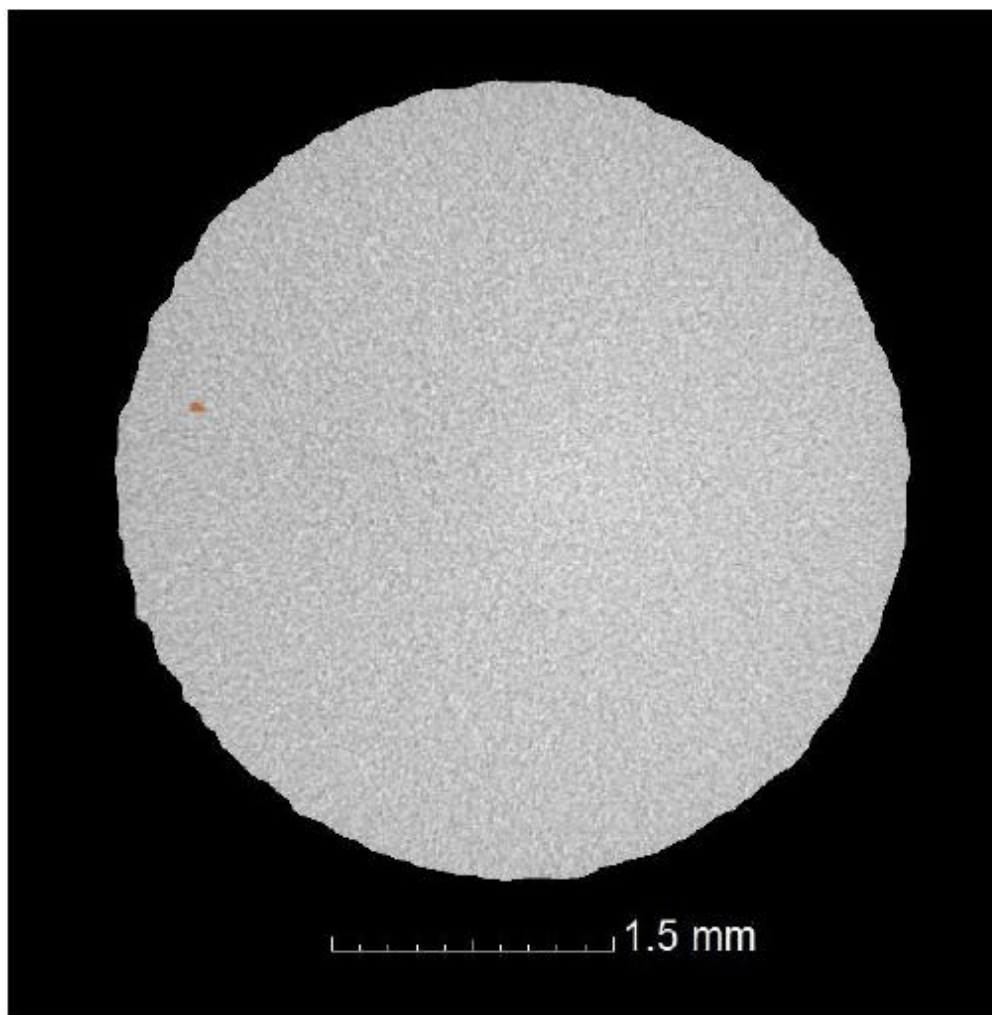
Figure 4: Z1b Sample: 2D Slice in top view

126 | P a g e

Radiation Science

This document is the property of NECSA and shall not be used,
reproduced, transmitted or disclosed without prior written permission
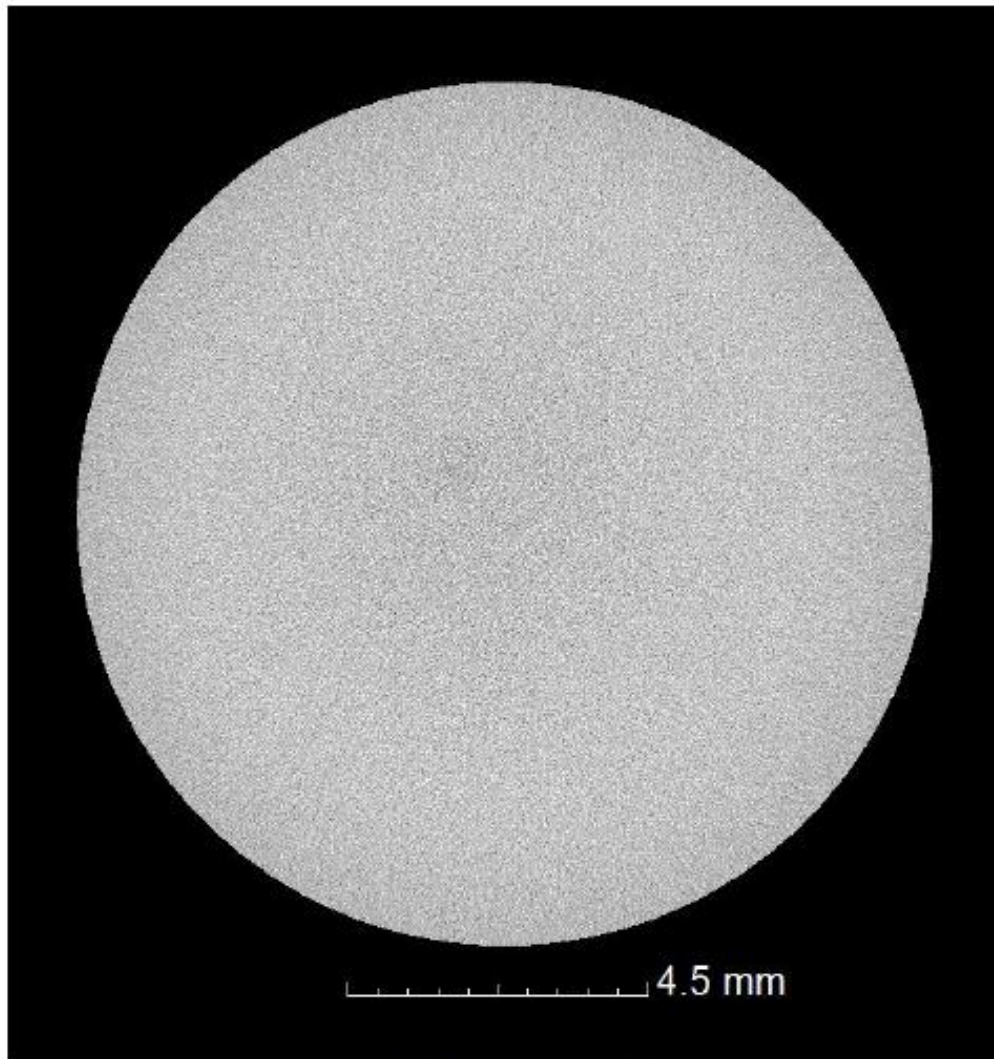
8.4: Z1 Sample

Figure 5: Z1 Sample: 2D Slice in top view

Radiation Science

This document is the property of NECSA and shall not be used,
reproduced, transmitted or disclosed without prior written permission

necsa
We're in your world

RESEARCH AND DEVELOPMENT
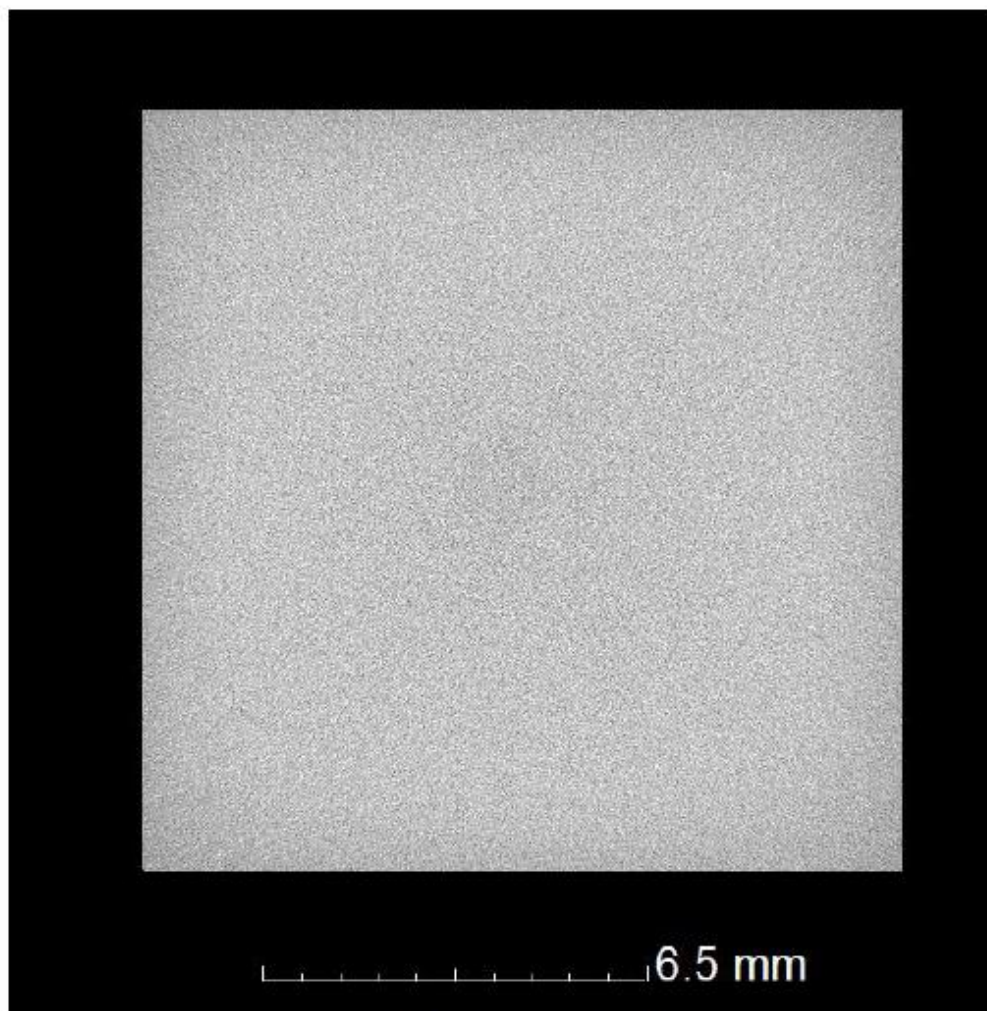
8.5: Z3 Sample

Figure 6: Z3 Sample: 2D Slice in top view

RESTRICTED

128 | P a g e

Radiation Science

This document is the property of NECSA and shall not be used, reproduced, transmitted or disclosed without prior written permission

necsa
We're in your world
RESEARCH AND DEVELOPMENT
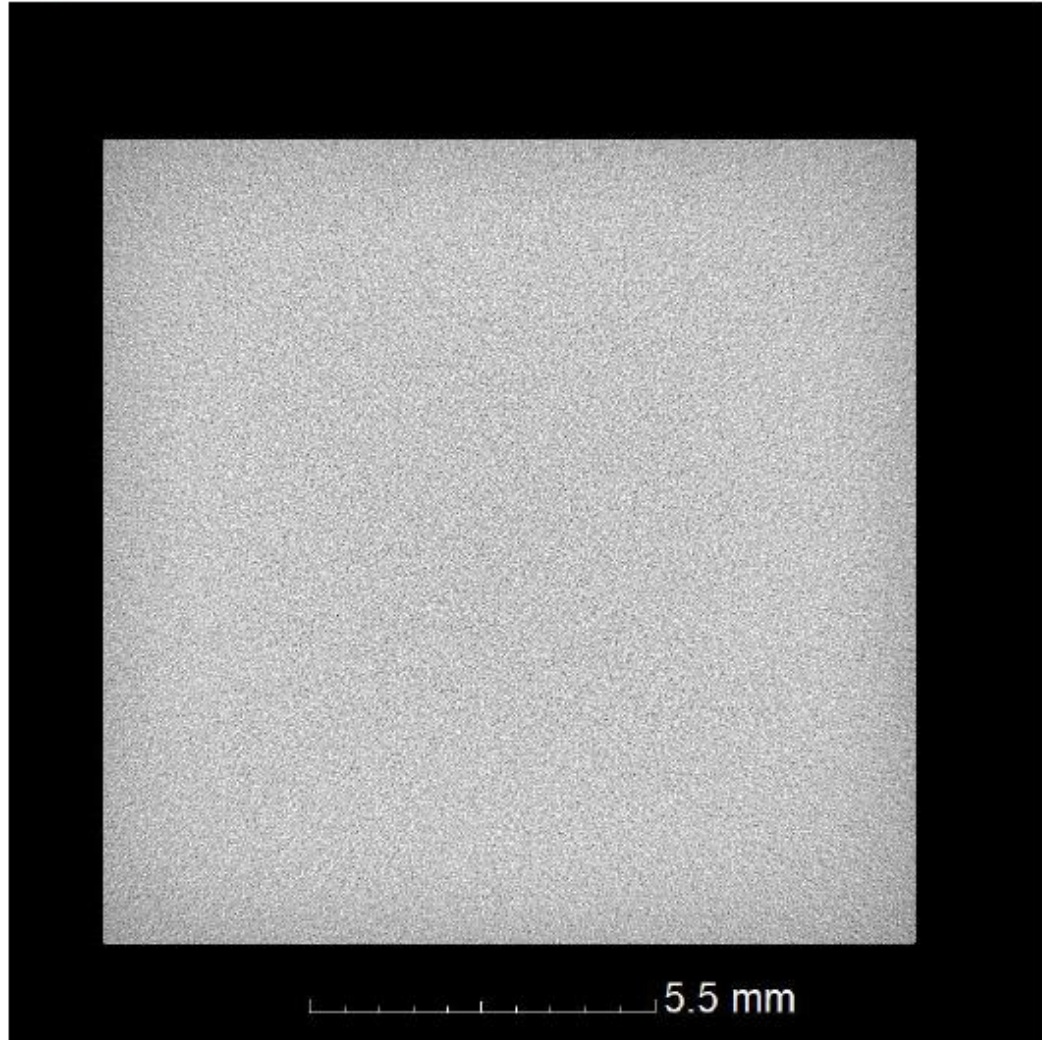
8.6: Z4 Sample

Figure 7: Z4 Sample: 2D Slice in top view

Radiation Science

This document is the property of NECSA and shall not be used,
reproduced, transmitted or disclosed without prior written permission

necsa
We're in your world

RESEARCH AND DEVELOPMENT
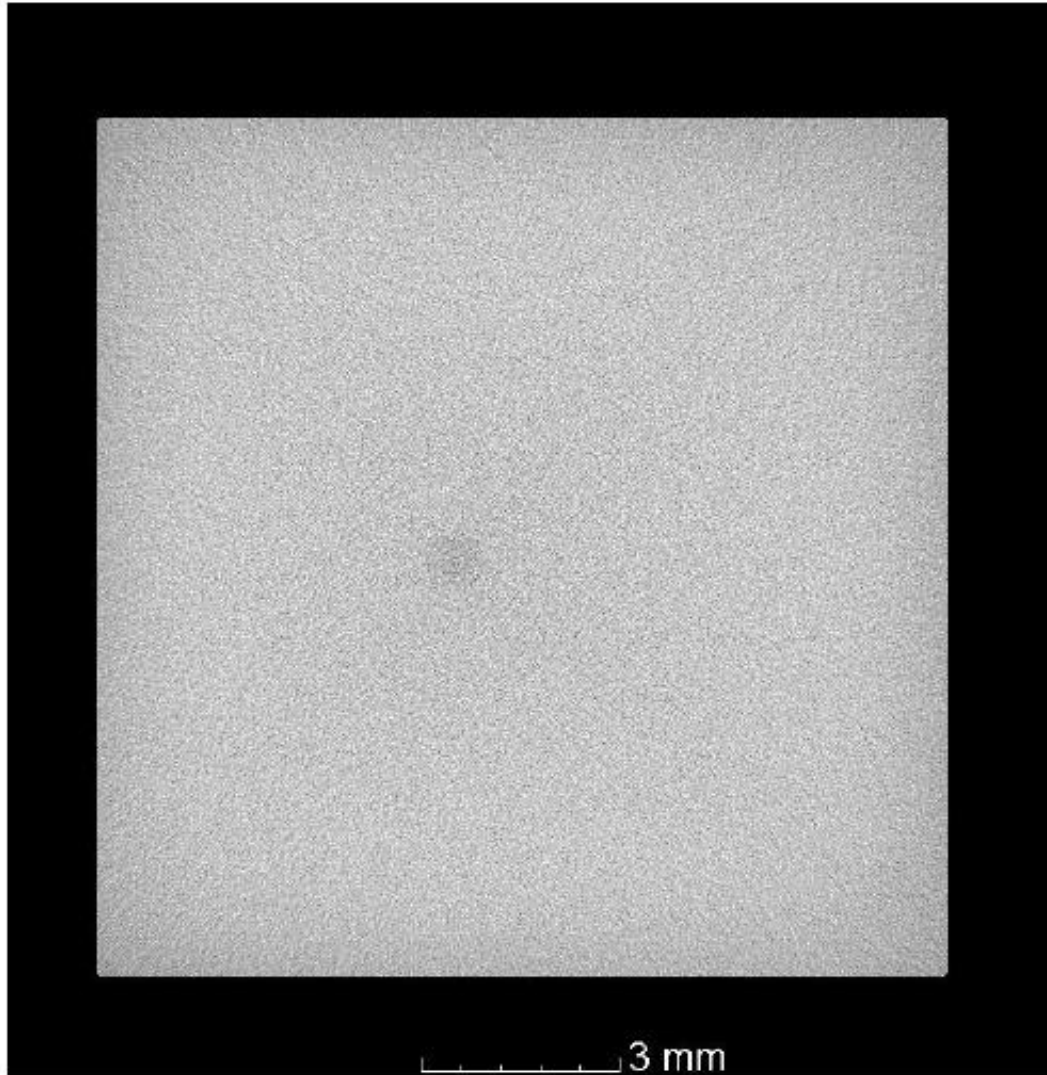
8.7: Z5 Sample

Figure 8: Z5 Sample: 2D Slice in top view

Radiation Science

This document is the property of NECSA and shall not be used,
reproduced, transmitted or disclosed without prior written permission

RESEARCH AND DEVELOPMENT
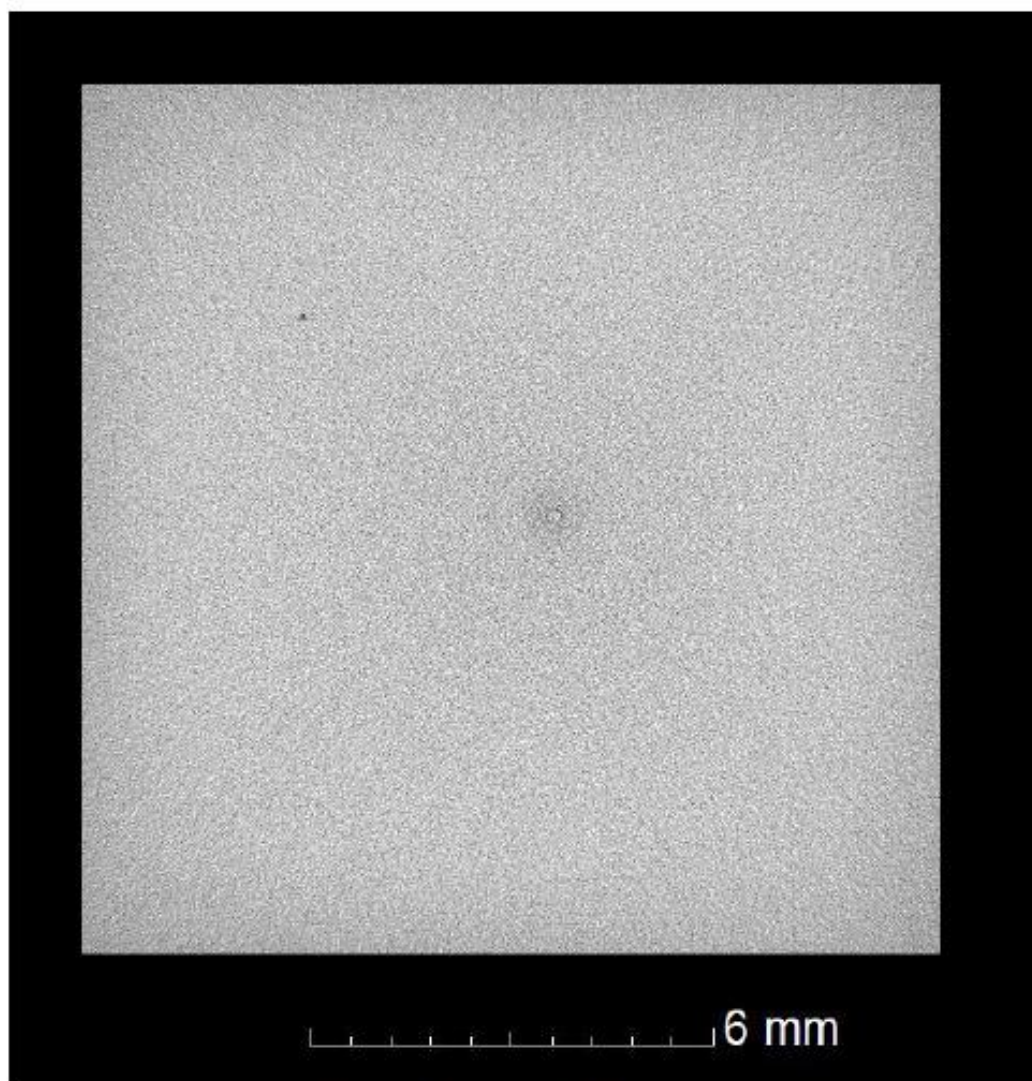
8.8: Z7 Sample

Figure 9: Z7 Sample: 2D Slice in top view

Radiation Science

This document is the property of NECSA and shall not be used,
reproduced, transmitted or disclosed without prior written permission

necsa
We're in your world
RESEARCH AND DEVELOPMENT
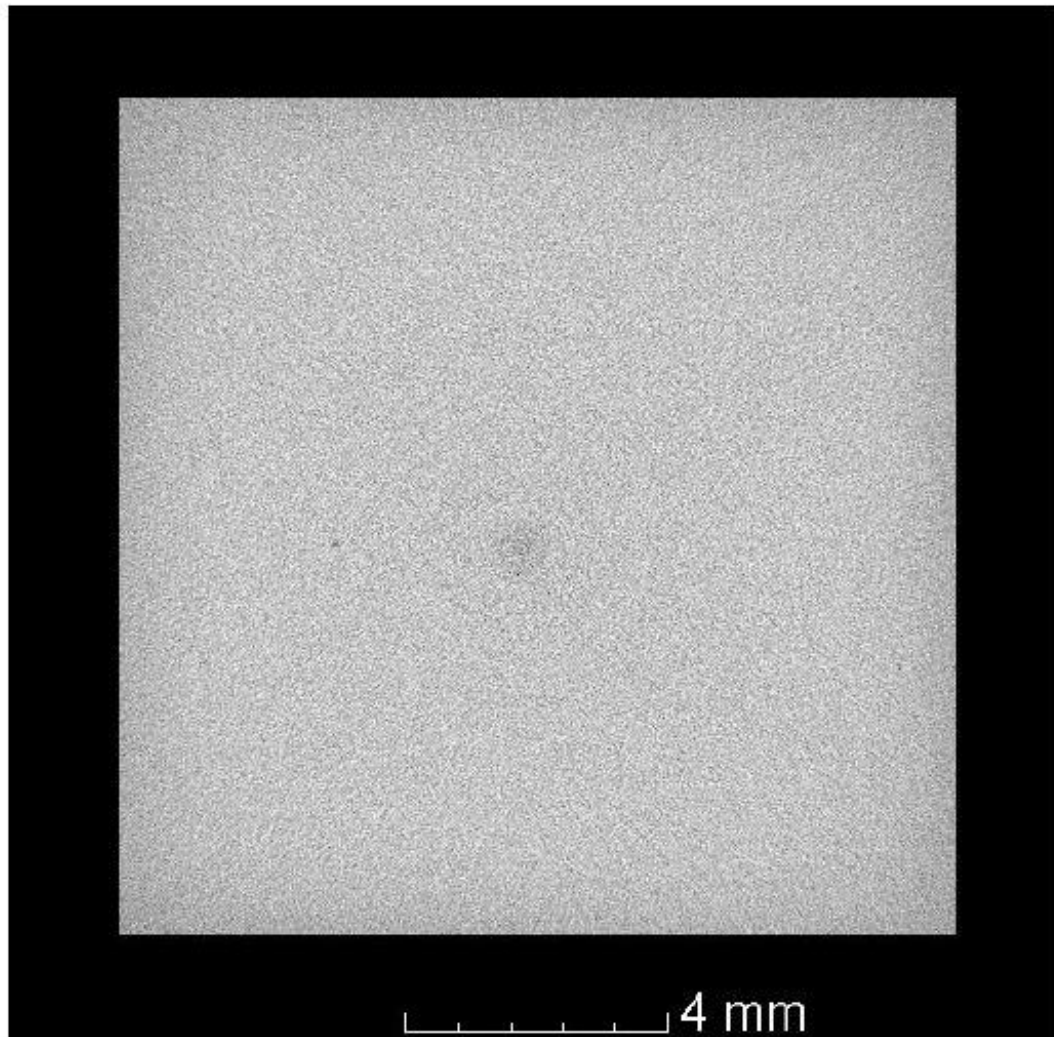
8.9: Z8 Sample

Figure 10: Z8 Sample: 2D Slice in top view

Radiation Science

This document is the property of NECSA and shall not be used,
reproduced, transmitted or disclosed without prior written permission

necsa
We're in your world

RESEARCH AND DEVELOPMENT
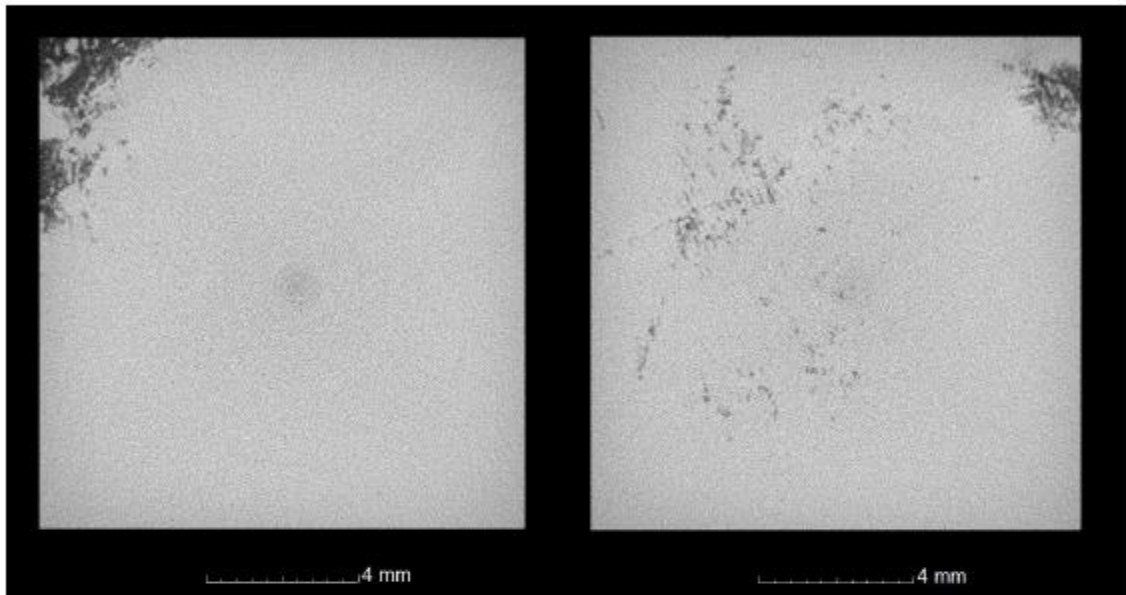
8.10: Z11 Sample

Figure 11: Z11 Sample: 2D LEFT: Slice in to view showing a crack on the edge and 2D RIGHT: Slice in top view showing a crack on the edge and pores in the crack region

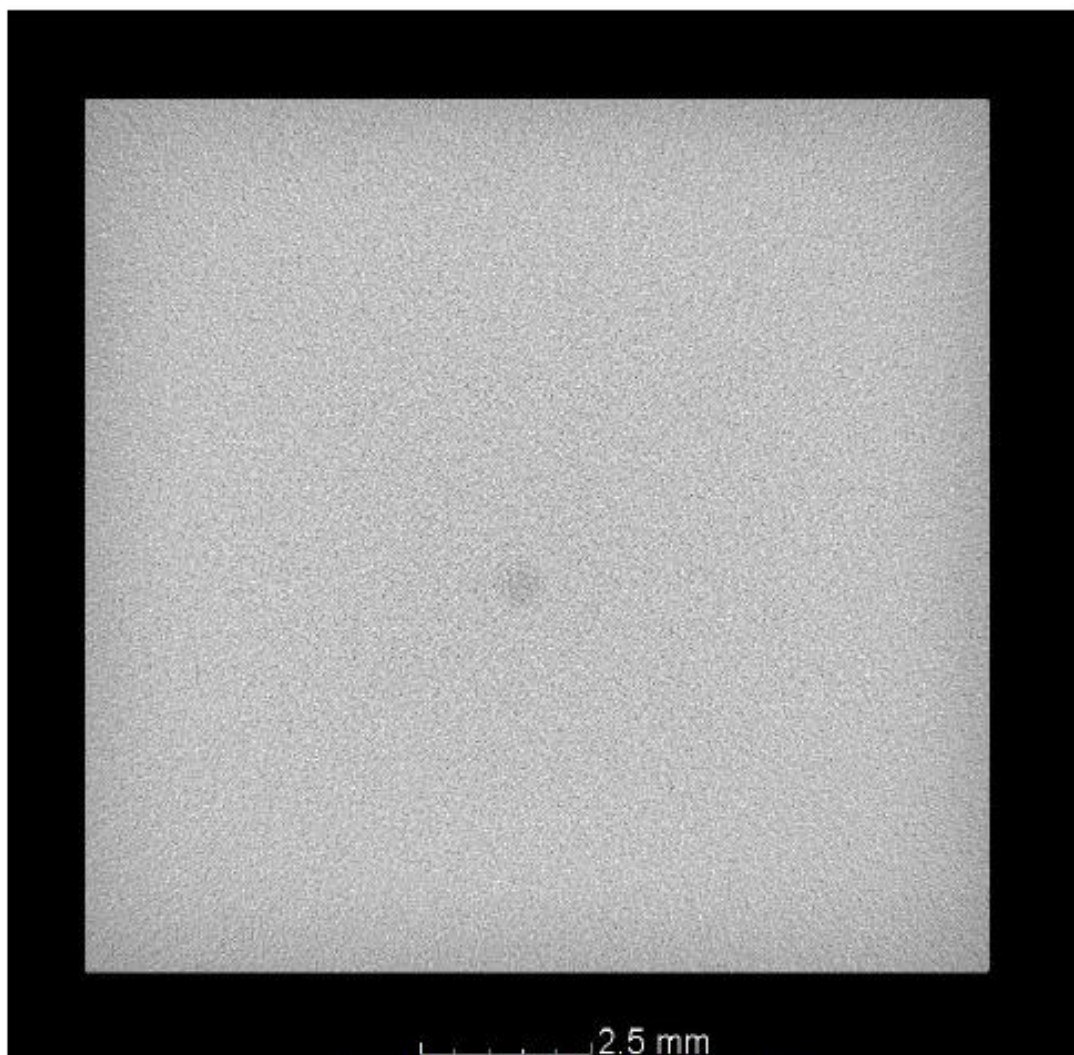![Central University of Technology, Free State logo]

Radiation Science
This document is the property of NECSA and shall not be used,
reproduced, transmitted or disclosed without prior written permission

necsa
We're in your world
RESEARCH AND DEVELOPMENT

8.11: Z12 Sample

Figure 12: Z12 Sample: 2D Slice in top view

Radiation Science
This document is the property of NECSA and shall not be used,
reproduced, transmitted or disclosed without prior written permission

necsa
We're in your world
RESEARCH AND DEVELOPMENT

9 Quantitative Results

The samples were scanned at the resolution 8.2 and 10.5 due to different region of interest thicknesses. No porosity information was detected on the Z3, Z4, Z5 and Z12 samples. This is due to the porosity information being smaller than the scanning resolution. However, porosity information could be detected on sample X1, Y1, Z1b, Z1, Z7, Z8 and Z11. Sample Z11 had the largest quantified porosity information because the crack was better defined and more pores were detected around the crack area given the scanning resolution. The quantified porosity information was based on visual and detectable pores to minimize over quantification of the porosity information which will include sample information.

Table 5: Porosity information

Sample ID	Scanning resolution (µm)	Porosity %	Comment
X1	8.2	0.0029	
Y1	8.2	0.0033	
Z1b	8.2	0.0013	
Z1	8.2	0.0011	
Z3	10.5	Non-detected	
Z4	10.5	Non-detected	
Z5	10.5	Non-detected	
Z7	10.5	0.0050	
Z8	10.5	0.0034	
Z11	10.5	0.116	Crack
Z12	10.5	Non-detected	

RESTRICTED

APPENDIX 8: CSIR tensile and fatigue testing results

T0381

TENSILE AND FATIGUE TESTING
OF
Ti6Al4V AM SPECIMENS

DOCUMENT CONTROL

Degree of Confidentiality	Company Confidential	
Title	Tensile & Fatigue Testing of Ti6Al4V AM specimens	
Author(s)	C. McDuling	
Date of Issue	8 April 2021	
Number of Pages	8	
Issuing Organisation: CSIR MFC PO Box 395 Pretoria 0001	Tel.: (27 12) 841-4226	
	Fax: (27 12) 841-3378	
CLIENT NAME	CUT	
PROJECT NUMBER	HVD9M1E	
KEYWORDS	Tensile and Fatigue Testing of Ti6Al4V specimens	
ISSUE NUMBER	1	
MT - LABORATORY MANAGER	Stephen Masete	Signature:
TECHNICAL SIGNATORY	Chris McDuling	Signature:

137 | P a g e

TABLE OF CONTENTS

EXECUTIVE SUMMARY

The Manufacturing Cluster of the CSIR, was requested by the Central University of Technology to conduct tensile and fatigue testing on Ti6Al4V AM specimens in accordance with ASTM E 8M and ASTM E 466 respectively.

The test results are summarized on pages 5 to 7.

1. INTRODUCTION

The Manufacturing Cluster of the CSIR was requested by Mr. Miya Hlakae of the Central University of Technology, to conduct tensile and fatigue testing on Ti6Al4V specimens in accordance with ASTM E 8M and ASTM E 466 respectively. Thirty as manufactured specimens, ten each from the x, y and z directions were submitted for testing. Three specimens from each direction were tensile tested and the remaining seven from each direction were fatigue tested. The gauge section of the specimens were not machined according to the specification. The purpose of the testing was to compare the fatigue life of the as manufactured surface of the specimens from the x, y and z directions.

2. TEST PROCEDURES

Tensile Test

Test standard	ASTM E 8 M
Procedure	LM-WP-402
Equipment	Instron 50kN 1342
Temperature	20 °C
Test rate	0.5mm/min.

Fatigue Test

Test standard	ASTM E 466
Procedure	LM-WP-403
Equipment	Instron 50kN 1342
Temperature	20 °C
Control mode	Load control – sinusoidal wave form
Frequency	10 Hz
R - ratio	0.1
Run out cycles	5×10^6

3. TEST RESULTS

Tensile Test

|	Specimen label	Length (mm)	Area (mm^2)	Tensile stress at Yield (Offset 0.2 %) (MPa)	Modulus (Chord 150 MPa - 600 MPa) (GPa)	UTS (MPa)	% Elongation (4*D)	Reduction of Area (%)
1	X1	20.00	13.85	860.42	116.3	948.13	16.50	43.0
2	X2	20.00	13.85	852.44	113.9	939.65	15.50	39.4
3	X3	20.00	13.85	853.73	115.0	941.53	15.05	33.3
Mean		20.00	13.85	855.53	115.1	943.10	15.68	38.6
Coefficient of Variation		0.000	0.000	0.501	1.010	0.472	4.732	12.739
Range		0.00	0.00	7.98	2.3	8.47	1.45	9.7
Standard Deviation		0.000	0.000	4.285	1.162	4.450	0.742	4.914
Minimum		20.00	13.85	852.44	113.9	939.65	15.05	33.3
Maximum		20.00	13.85	860.42	116.3	948.13	16.50	43.0
Median		20.00	13.85	853.73	115.0	941.53	15.50	39.4

|	Specimen label	Length (mm)	Area (mm^2)	Tensile stress at Yield (Offset 0.2 %) (MPa)	Modulus (Chord 150 MPa - 600 MPa) (GPa)	UTS (MPa)	% Elongation (4*D)	Reduction of Area (%)
1	Y1	20.00	13.85	863.94	118.1	947.64	13.25	30.6
2	Y2	20.00	13.85	860.75	120.8	943.50	14.70	36.0
3	Y3	20.00	13.85	856.71	114.6	941.14	15.05	41.2
Mean		20.00	13.85	860.47	117.8	944.09	14.33	35.9
Coefficient of Variation		0.000	0.000	0.421	2.622	0.348	6.658	14.846
Range		0.00	0.00	7.23	6.2	6.50	1.80	10.7
Standard Deviation		0.000	0.000	3.625	3.089	3.289	0.954	5.334
Minimum		20.00	13.85	856.71	114.6	941.14	13.25	30.6
Maximum		20.00	13.85	863.94	120.8	947.64	15.05	41.2
Median		20.00	13.85	860.75	118.1	943.50	14.70	36.0

	Specimen label	Length (mm)	Area (mm^2)	Tensile stress at Yield (Offset 0.2 %) (MPa)	Modulus (Chord 150 MPa - 600 MPa) (GPa)	UTS (MPa)	% Elongation (4*D)	Reduction of Area (%)
1	Z1	20.00	14.32	774.78	110.0	888.52	15.75	50.3
2	Z2	20.00	14.25	780.48	109.5	894.81	15.60	49.4
3	Z3	20.00	14.25	781.33	108.5	891.61	16.15	50.4
Mean		20.00	14.28	778.86	109.3	891.65	15.83	50.0
Coefficient of Variation		0.000	0.271	0.457	0.703	0.353	1.796	1.098
Range		0.00	0.07	6.55	1.5	6.29	0.55	1.0
Standard Deviation		0.000	0.039	3.562	0.769	3.146	0.284	0.550
Minimum		20.00	14.25	774.78	108.5	888.52	15.60	49.4
Maximum		20.00	14.32	781.33	110.0	894.81	16.15	50.4
Median		20.00	14.25	780.48	109.5	891.61	15.75	50.3

Specimen 1 to 3
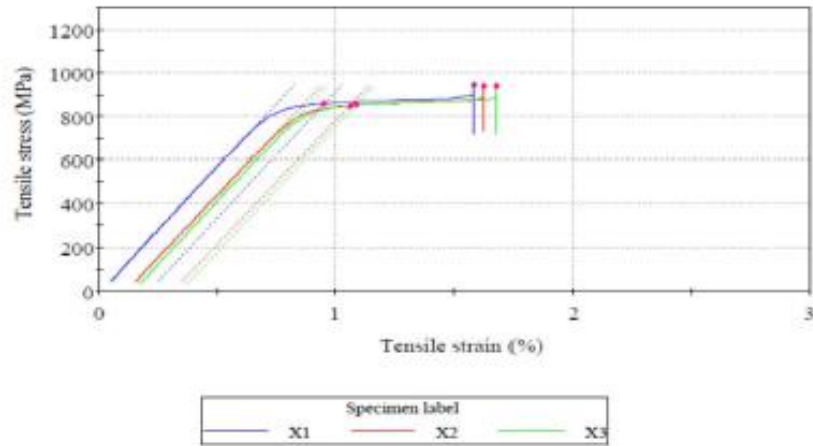
Specimen 1 to 3

Specimen 1 to 3
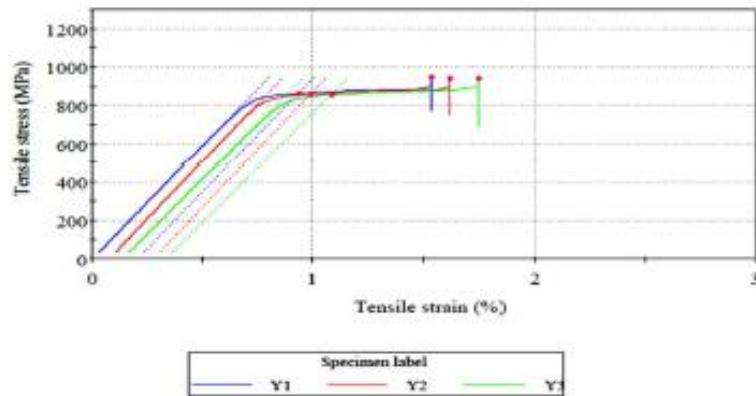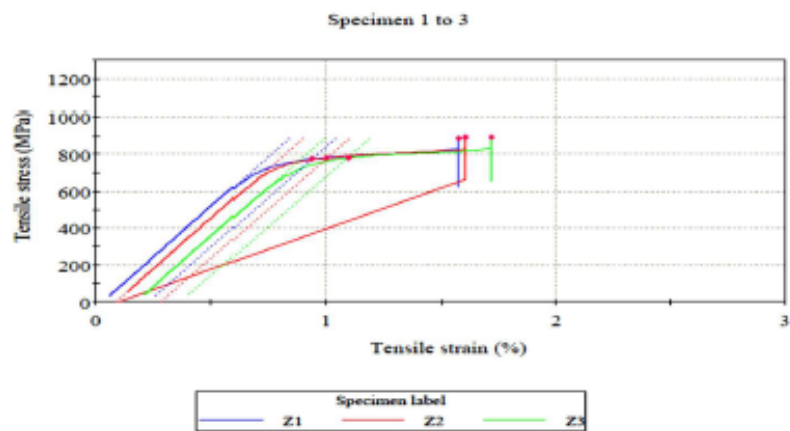
Fatigue Test

Specimen Label	X4	X5	X9	X6	X7	X10	X8
Maximum Stress MPa	360	300	270	230	210	200	190
Number of cycles at failure	147027	218190	346930	513876	893273	1153581	5000000
Specimen Label	Y4	Y5	Y9	Y8	Y6	Y10	Y7
Maximum Stress MPa	360	300	270	250	230	200	190
Number of cycles at failure	132859	304007	434787	538903	598800	1002143	5000000
Specimen Label	Z4	Z5	Z6	Z10	Z7	Z9	Z8
Maximum Stress MPa	450	418	360	300	270	250	225
Number of cycles at failure	50142	61584	122595	483996	370439	730494	5000000
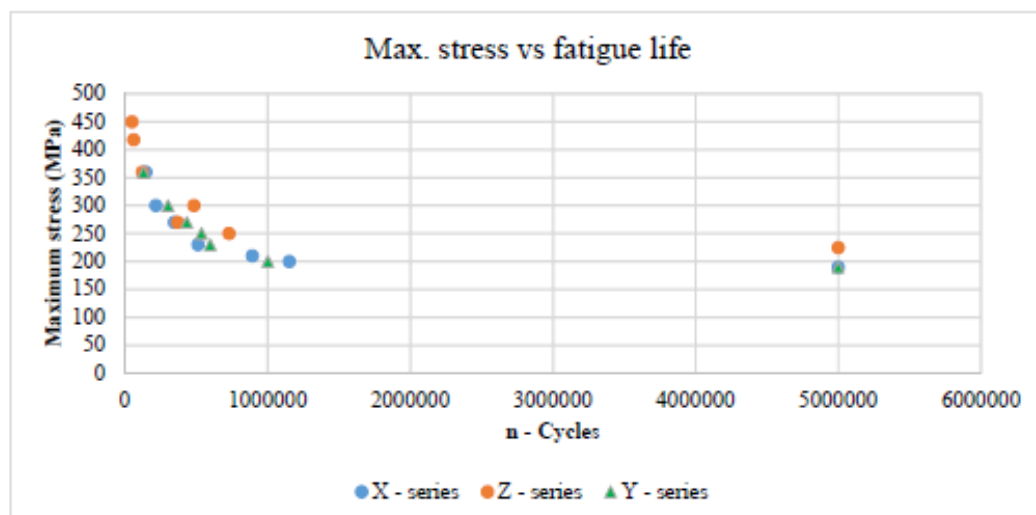
4. GENERAL REMARKS

4.1   These test results apply only to the specimens supplied to the CSIR for testing and the CSIR accepts no responsibility for any product differences due to manufacturing variations.

4.2   The CSIR takes no responsibility for the applicability of the test results to real life operating conditions of the product.

4.3   The CSIR cannot be held responsible for any failure or consequential damage resulting from such failure.

<u>**END**</u>